AD_________________

Award Number: W81XWH-08-1-0613

TITLE: X-Ray Phase Imaging For Breast Cancer Detection

PRINCIPAL INVESTIGATOR: Xizeng Wu, Ph.D.

CONTRACTING ORGANIZATION: University of Alabama at Birmingham,
Birmingham, AL 35294

REPORT DATE: September 2012

TYPE OF REPORT: Final

PREPARED FOR: U.S. Army Medical Research and Materiel Command
Fort Detrick, Maryland 21702-5012

DISTRIBUTION STATEMENT: Approved for public release; distribution unlimited

The views, opinions and/or findings contained in this report are those of the author(s) and should not be construed as an official Department of the Army position, policy or decision unless so designated by other documentation.

REPORT DOCUMENTATION PAGE		*Form Approved* *OMB No. 0704-0188*

Public reporting burden for this collection of information is estimated to average 1 hour per response, including the time for reviewing instructions, searching existing data sources, gathering and maintaining the data needed, and completing and reviewing this collection of information. Send comments regarding this burden estimate or any other aspect of this collection of information, including suggestions for reducing this burden to Department of Defense, Washington Headquarters Services, Directorate for Information Operations and Reports (0704-0188), 1215 Jefferson Davis Highway, Suite 1204, Arlington, VA 22202-4302. Respondents should be aware that notwithstanding any other provision of law, no person shall be subject to any penalty for failing to comply with a collection of information if it does not display a currently valid OMB control number. **PLEASE DO NOT RETURN YOUR FORM TO THE ABOVE ADDRESS.**

1. REPORT DATE *(DD-MM-YYYY)* September 2012	**2. REPORT TYPE** Final	**3. DATES COVERED** *(From - To)* 1 September 2008 - 30 September 2012
4. TITLE AND SUBTITLE X-Ray Phase Imaging For Breast Cancer Detection		**5a. CONTRACT NUMBER**
		5b. GRANT NUMBER W81XWH-08-1-0613
		5c. PROGRAM ELEMENT NUMBER
6. AUTHOR(S) Xizeng Wu, Ph.D.		**5d. PROJECT NUMBER**
		5e. TASK NUMBER
		5f. WORK UNIT NUMBER
7. PERFORMING ORGANIZATION NAME(S) AND ADDRESS(ES) University of Alabama at Birmingham, Birmingham, AL 35294		**8. PERFORMING ORGANIZATION REPORT NUMBER**
9. SPONSORING / MONITORING AGENCY NAME(S) AND ADDRESS(ES) U.S. Army Medical Research and Material Fort Detrick, Maryland 21702-5012		**10. SPONSOR/MONITOR'S ACRONYM(S)**
		11. SPONSOR/MONITOR'S REPORT NUMBER(S)

12. DISTRIBUTION / AVAILABILITY STATEMENT

Approved for public release; distribution unlimited

13. SUPPLEMENTARY NOTES

14. ABSTRACT

Aiming to develop a low-dose and quantitative x-ray phase imaging technique for facilitating breast cancer detection, in this project we designed and built a high-voltage x-ray imaging prototype that enables x-ray phase imaging and radiation dose reduction, as is demonstrated in phantom imaging. We developed an innovative phase attenuation duality based (PAD-based) method, which greatly facilitating the low doe phase retrieval for soft tissue body parts such as breast. The phantom imaging demonstrated that the PAD-based phase retrieval greatly enhance the contrast-to noise ratios of images, hence it has good potential for reducing radiation doses in breast imaging. We also developed a robust general phase retrieval method, the attenuation-partition based (AP-based) method for general clinical imaging. This method was demonstrated to be superior to the mostly used phase retrieval method in literature in performing robust phase retrieval for low-dose imaging. Considering the high breast density is one of the biggest risk factors for breast cancer, we proposed for the first time an x-ray phase-shifts based method of breast density measurement, as a quantitative imaging method of the phase-sensitive breast imaging.

15. SUBJECT TERMS

Phase-contrast x-ray imaging, Breast imaging, Phase retrieval

16. SECURITY CLASSIFICATION OF:			**17. LIMITATION OF ABSTRACT**	**18. NUMBER OF PAGES**	**19a. NAME OF RESPONSIBLE PERSON** USAMRMC
a. REPORT U	**b. ABSTRACT** U	**c. THIS PAGE** U	UU	74	**19b. TELEPHONE NUMBER** *(include area code)*

Table of Contents

Page

Introduction…………………………………………………………….………..…... 4

Body……………………………………………………………………………….. 4

Key Research Accomplishments………………………………………….……….. 12

Reportable Outcomes……………………………………………………………. 13

Conclusion………………………………………………………………………. 14

References……………………………………………………………………….. 14

Appendices……………………………………………………………………… 16

Introduction

Conventional mammography is limited in its sensitivity and specificity for breast cancer detection, since it relies on the small difference in x-ray attenuation between breast tissues and the lesions. As x-ray wave passes through breast, x-ray undergoes phase-shifts as well. X-ray phase-shift differences between tissue and lesions are several hundreds times larger than their attenuation differences. Hence the phase-sensitive breast imaging has the potential to greatly enhance the cancer detection sensitivity and specificity and reduce the radiation doses to breast. It is challenging to implement phase-sensitive x-ray breast imaging because one should provide the partially coherent x-ray illumination, maintain short exposure times, and limit radiation doses. Moreover, in order to fully exhibit tissue phase contrast, one has to perform phase retrievals. But the most commonly used phase retrieval method is unstable to image noise and requires high radiation dose levels to work, thus this common phase retrieval method is not feasible in clinical imaging where radiation dose control is critically important.

Taking up these challenges, the long-term objective of the project is to develop a low-dose and quantitative x-ray phase imaging technique for facilitating breast cancer detection. The Specific Aims of the project are: (1) Develop a prototype phase-imaging system enabling the phase retrieval, that is, the reconstruction of objects phase-maps. The system hardware comprises a micro-focus tube operating at high tube voltages, a high-resolution photostimulable phosphor based detector (CR-system). An innovative phase retrieval method will be developed to retrieve tissue phase map from a single recorded image. (2) Validate the accuracy of the reconstructed tissue projected electron densities; validate the many-fold radiation dose reduction to be achieved with the proposed system; conduct subjective measurements to characterize the performance of the proposed system.

Body

Toward to the Specific Aims set as above, we have accomplished following works associated with each task outlined in the approved Statement of Work.

Development of a prototype x-ray phase imaging system (Task 1)

Design and build the system prototype

In this project we designed and built a unique x-ray imaging prototype using high tube-voltages for implementing the phase contrast imaging and enabling radiation dose reduction. The key design issue for an inline phase contrast imaging system is how to optimize the phase

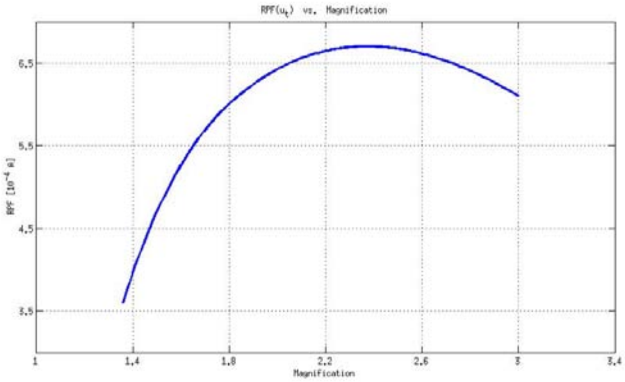

Figure 1. Relative phase contrast visibility $|RPF(\vec{u})|$ varies for different $\mathbf{R_1}$ and $\mathbf{R_2}$ of a system with a SID =1.5 m. In this plot we assumed a uniform circular focal spot of 50 μm in diameter, and a detector pitch of 43.75 μm, 60.5 keV x-ray and a fine object structure of 15 line-pairs/mm.

contrast visibility by balancing the conflict requirements on x-ray spatial coherence and reasonable exposure times . In our design we tackled this issue by using a method based the relative phase-visibility factor (RPF), a phase imaging metric that we previously developed [Wu, Liu 2004]. We computed the RFP as a function of different configurations with varying x-ray wavelengths, tube focal spot sizes, different source-object- and object-detector-distances (denoted by $\mathbf{R_1}$ and $\mathbf{R_2}$ respectively), finest object-structure sizes, and the detector sampling pitches. Form the computed RPFs we determined the optimal system configuration for phase contrast visibility. Figure 1 shows the RFP as a function of $\mathbf{R_1}$ and $\mathbf{R_2}$ for a system configuration. Figure 1 shows that the optimal magnification factors are found to be in the range of 2 to 2.3. The experiment with various phantoms (such the step-edge phantom, mammography BR3D phantom, contrast details phantom, etc.) confirmed optimal phase contrast visibility with the designed system configurations.

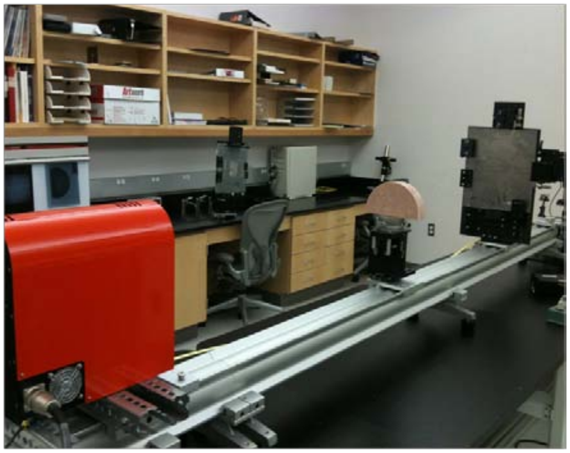
Fig. 2. A high-energy x-ray phase contrast imaging system

According to these optimal system configurations determined from above RPF-analysis, our subcontractor Dr. Liu and his group integrated the hardware components successfully built a prototype system as is shown in Fig. 2. In order to operate the prototype in both conventional and phase contrast imaging modes for comparisons, the imaging and measurement components (the x-ray tube, CR-plate) are mounted on an optical rail, which allows to vary. Note that the object -detector distance $\mathbf{R_2}$ is kept relatively large as determined by the RFP-analysis to allow phase-shifted x-rays diffract to form phase-contrast images. The source is a micro-focus tube (Model L8121-01, Hamamatsu Photonics) with integrated high voltage power supply. The tube has a tungsten-target and a uniform circular focal spot of 50 $\mu\mathrm{m}$ in diameter. The mounted detector is a Konica Minolta Konica large FOV (24 x 30cm) mammography photostimulable phosphor plate and a Konica REGIUS 190 Reader of a 43.75 $\mu\mathrm{m}$ sampling pitch. The system has been used in acquiring phase contrast projection images of various phantoms in this project.

Develop the phase retrieval methods

With a micro-focus x-ray tube the achievable x-ray spatial coherence is limited, hence a x-ray tube-based system can generate only moderate phase-contrast at tissue interfaces and boundaries with dark-bright diffraction fringes. In order to fully exhibit the tissue phase contrast, one should perform the phase retrieval from the acquired phase-contrast images. The phase retrieval is a procedure of retrieving the phase-shift map $\varphi(\vec{r})$ of an object from its phase-sensitive projections, where $\varphi(\vec{r}) = -\lambda r_e \int_{ray} \rho_e(\vec{r},s)ds$ and $\rho_e(\vec{r},s)$ denotes the tissue electron density, $r_e =$ 2.818 x 10^{-15} m is the classical electron radius and λ is x-ray wavelength. By means of phase retrieval from phase-contrast images, one can disentangle the phase contrast from mixed attenuation- and phase-contrast in phase-contrast images. Moreover, a retrieved tissue phase map provides a map of imaged object's projected electron densities (the ray integrals of electron densities) as well. The challenge for developing breast x-ray phase imaging is how to overcome the difficulty for implementing phase retrieval with breast imaging.

In general one needs to acquire at least two and mostly four to five images with different object-detector distances. This requirement is imposed by the x-ray wave nature and its wave equation. The most commonly used method in the literature for phase retrieval in the literature is based on the Transport of Intensity Equation (TIE) [Allen, Oxley. 2001]. According to the TIE-based method, one needs to acquire at least two images, one contact radiograph, and one phase contrast image, for retrieving a phase map of an object. While the TIE-based phase retrieval method is computational effective for the cases with strong phase contrast effects and low noise levels, we found that it will fail for phase retrieval when the acquired projection images are contaminated with relatively strong noises. In other words, we found that the common TIE-based method is not robust against noise. Suppressing x-ray quantum noise may require using high radiation doses in the image acquisitions. For clinical applications it is imperative to limit and reduce radiation doses involved, hence it is critical to develop low-dose robust phase retrieval methods for clinical applications of phase contrast imaging, as in clinical applications where radiation dose constraints dictates relatively high noise levels. Moreover, the TIE-based method needs to acquire multiple (at least two) images with different object-detector distances. This multiple-exposure requirement adds to the radiation dose burden and makes the procedure cumbersome. To overcome these difficulties in implementing phase retrieval in clinical imaging, we developed two phase retrieval methods as described in following:

(1) Development of the Phase-Attenuation Duality based (PAD-based) phase retrieval method

First, we found that when high energy x-rays are employed, we can robustly retrieve the map of a soft tissue object from just a single phase-contrast projection of the object. In fact, analyzing the tissue attenuation data, we realized that the soft tissues' attenuation cross sections can be approximated by that of x-ray incoherent scattering, as long as x-ray energies are of about 60 keV or higher. Under this circumstance, we found that soft-tissue attenuation and soft-tissue phase-shifts are all related to the projected electron density. We call this correlation as the phase-attenuation duality. Utilizing this notion of the phase-attenuation duality (PAD), we were able to simplify x-ray wave equation, and discovered an innovative method to retrieve a phase-map from just a single recorded image [Wu, Liu, Yan 2005]. We call this novel method as the PAD-based phase retrieval method. With this method the cumbersome procedures associated with required exposures for the phase retrieval are eliminated, and more importantly, the radiation doses involved are reduced as well.

In the project we employed high tube voltages such as 120 kVp-150 kVp for breast phantom imaging for shortening the exposure times and reducing radiation doses. Phase retrieval from a single phase-contrast image forms a key strategy for this project. However, we noted that our previous PAD-based phase retrieval method becomes inaccurate in the cases of high-resolution and large object-detector distances. Extending our previous results, in this project we developed a more accurate PAD-based phase retrieval method. We noticed that the Fresnel diffraction can be thought as a x-ray wave-front filtering with the Fresnel propagator $\exp(i\pi\lambda z\vec{u}^2)$, where λ is x-ray wavelength and $\vec{u}$ is the wave-front's transverse spatial frequency vector, and z is the object-detector-distance. So the phase of the propagator, i.e. $\pi\lambda z\vec{u}^2$, determines how strongly the exiting wavefront will be diffracted in the propagation. The previous PAD-based phase retrieval formula was derived by linearizing Fresnel propagator phases [Wu, Liu, Yan 2005]. Therefore, in order to develop robust phase retrieval algorithms with high accuracies, one should not linearize Fresnel propagators, rather one should consider the full exponential propagators instead. In this project we derived a new PAD-based phase retrieval method using the full exponential propagators. This new phase retrieval method lays a sound foundation for implementing high-resolution phase-sensitive imaging of soft tissue objects. For details, please refer to [Wu and Yan 2009].

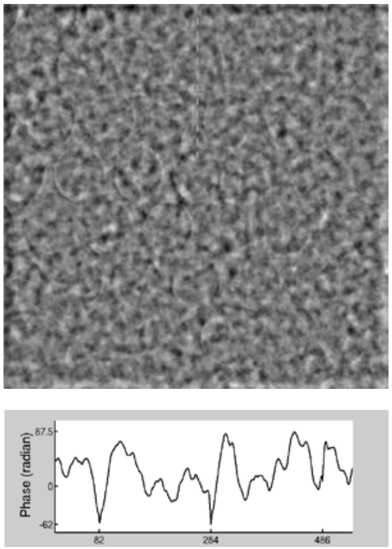

Fig. 3. (Upper) Retrieved phase maps of the bubble wrap with the TIE-based method and mended with the Tikhonov regularization. (Lower) Profile of the retrieved phase values along the marked line.

(2) Development of the Attenuation-Partition based (AP-based) phase retrieval method

The PAD-based phase retrieval method described above can be used only for soft tissue body parts imaged with high-energy x-rays. One still needs to develop a robust phase retrieval method for general clinical imaging applications as well. Extending the PAD-method to general cases, we developed the attenuation-partition based (AP-based) method for general phase retrievals. In this method, we utilize the correlation between the x-ray phase shift and its attenuation to eliminate the intrinsic singularities involved in the TIE-based phase retrieval method. These singularities may amplify the noise in the acquired images and result in instability in phase retrievals. In the AP-based method, we first extract the Compton scattering cross-sections from the attenuation image and retrieve an approximate phase map. We then iteratively incorporate the rest of the attenuation cross-section into phase retrieval by repeatedly correcting errors, which is calculated as the differences between the measured phase-contrast image intensities and the Fresnel diffraction estimates [Yan, Wu, Liu 2010]. We first proposed the idea in 2008, and in this project we modified the original iterative algorithm coding for speeding the iteration convergence, and performed quantitative and systematic evaluation of its robustness and efficiency. We systematically compared the performance of this new algorithm with two widely used phase retrieval algorithms in the literature including the TIE-based method described above. We showed that the AP-based method converges faster than the Gerchberg-Saxton algorithm in the Fresnel diffraction regime, and is much more robust against image noise than the TIE-based method. For details, please refer to [Yan, Wu, Liu 2010].

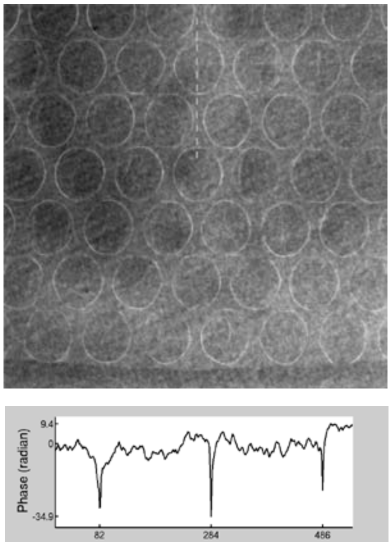

Fig. 4. (Upper) Retrieved phase maps of the bubble wrap with the AP-based method. (Lower) Profile of the retrieved phase values along the marked line.

Moreover, we also analyzed the phase maps retrieved from the experimental images of a phantom by using the AP-based and TIE-based methods, respectively. We applied these two methods to experimental projection images of an air-bubble wrap phantom for retrieving the phase map of the bubble wrap. Fig. 3-(upper) shows the retrieved sample's phase map using TIE-based method. Apparently the retrieval with the TIE-based method is very unsatisfactory, as the bubble rims are hardly visible in the extremely cluttered background in the phase map. In a stark contrast, Fig. 4-(upper), which was retrieved using the AP-method, depicts the bubble rims prominently. In order to gauge the accuracies of the retrieved phase values, we measured the thicknesses of the flat bases of the wrap, and found that the approximate phase-shifts at the flat bases of the wrap is about -4.2 radian. On the other hand, according to the phase profile in with the AP-based method (Fig. 4(lower)), the average phase shift at the flat bases of the wrap is -1.05 radian, the two phase-shift estimates are reasonably close. In comparison, the phase profile with the TIE-based method (Fig. 3(lower),) depicts just messy up-down peaks buried in cluttered and noisy background. According to this profile, the phase-shift values at the bases fluctuate over a wide range from 0 to +87.5

radian with an average of +27.3 radian, contradicting to the fact that x-ray phase shifts should be negative. This stark comparison shows that the conventional TIE-based phase retrieval method is unstable against the noise in the wrap's projection images, while the AP-based phase retrieval method is shown in the experiment to be superior to the TIE-based method for the robustness in performing the phase retrieval. For details, please refer to [Yan, Wu, Liu 2011].

Extending the research works on the phase retrieval methods, as a by-product of this project, we made a progress in understanding the apparent linear attenuation coefficients in the inline phase contrast tomography. In the inline phase contrast x-ray tomography the reconstructed apparent linear attenuation coefficient values in the tomography may be greatly larger than sample's linear attenuation coefficients or even be negative. These "artifacts" may cause faulty interpretation of sample structures, and impede even qualitative characterizations for tissues and materials. In this period we derived a general formula to quantitatively relate the apparent linear attenuation coefficient values in cone-beam phase contrast tomography to sample's linear attenuation coefficients and refractive indices. This formula overcomes the gross inaccuracy of the existing formula in the literature in analyzing high-resolution phase contrast tomography, and it will be useful for correctly interpreting and quantifying the apparent linear attenuation coefficients in cone-beam x-ray phase contrast tomography in the biomedical and material science applications. This result advanced the understanding of the image contrast mechanism of phase contrast tomography. For details, please refer to [Yan and Wu 2011].

Development of system software package

In this project we developed efficient coding with the software modules for the image registration, flat-filed correction, and phase retrievals. In addition, we developed as well phase contrast imaging simulation software incorporating parallel programing.

Characterization of the x-ray phase imaging system (Task 2)

Investigating the effects of x-ray beam hardening on detective quantum efficiency (DQE) and radiation dose

A comprehensive quantitative determination of the performance of an imaging system is the detective quantum efficiency (DQE), as it represents the transfer function of the signal-noise ratio of the system. The goal of this study was therefore to provide an initial investigation of the effects of a range of beam hardening levels on the DQE and the average glandular dose. The DQE and the average glandular dose were both measured under the same experimental conditions for a range of beam hardening levels. The comparison of all quantities comprising the DQE exhibits very close correlation between the results obtained without added beam hardening to the results corresponding to the range of beam hardening levels. For the specific experimental conditions utilized in this study, the results are an indication that the use of hardened x-ray beam holds the potential to reduce the radiation dose without decreasing the performance of the system. For details, please refer to [Wong, Wu, Liu. 2011].

Evaluating Image quality, phase map accuracy and associated radiation dose reduction

We have conducted preliminary imaging experiments using 100, 120, 140 kVp and with four different phantoms, the ACR MAP phantom, a contrast-detail phantom, an acrylic step-edge, and a breast tissue-equivalent phantom. As current breast imaging (mammography and breast tomosynthesis) employs exclusively low x-ray tube voltages (25-40 kVp), our strategy is to utilize the phase contrast extracted out with the phase retrievals to compensate for the attenuation-contrast loss associated with the use of high tube-voltages, thereby achieving significant radiation doses reduction. We images the phantoms with different geometric

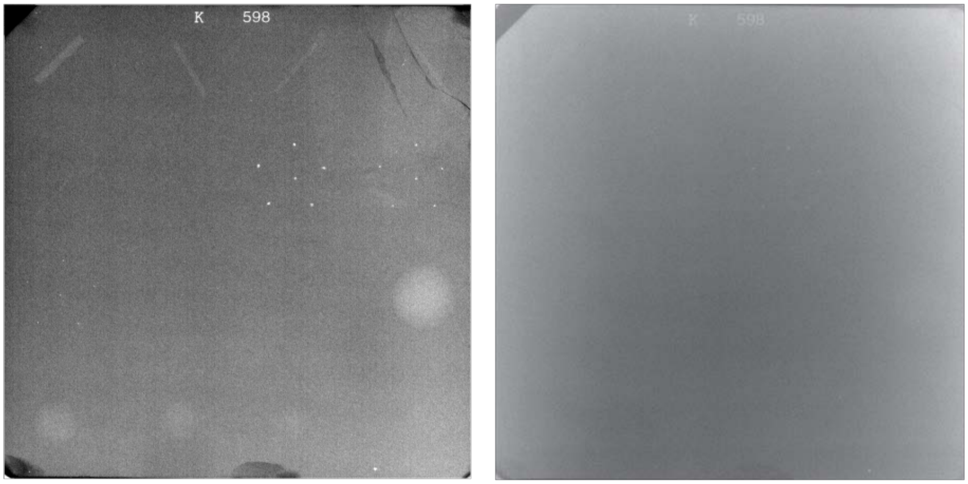

Fig. 5. Two images of an ACR accreditation phantom acquired with the 100 kVp and the same dose to phantom. (left) Phase contrast image of the phantom with M = 2. (right) Contact radiograph of the phantom.

configurations including the settings with magnification factors of 1, 2, 2.5, 3. Observer studies were performed utilizing the ACR MAP and contrast-detail phantoms for qualitative and quantitative comparisons, such as those in terms of the feature scoring and contrast-noise ratio (CNR). In this way we validated the optimal geometric configurations for phase contrast visibility as determined in the system design based on the theoretical phase contrast visibility analysis [Wu, Liu 2004]. In addition to phantom image quality evaluation, in order to characterize the performance of the prototype system, we checked as well the accuracy of the retrieved phantom phase maps, and verified the radiation dos reduction achieved.

Study on ACR MAP Phantom

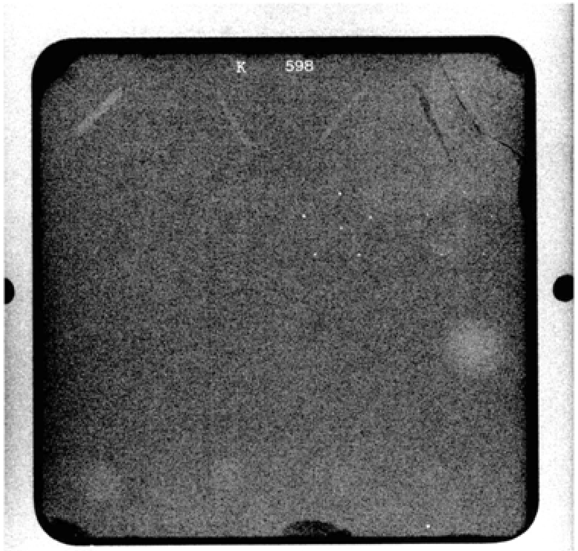

Fig. 6. Phase map of an ACR accreditation phantom retrieved by using the duality-based method from a single phase-sensitive projection. The projection was acquired with 120 kVp and a glandular dose of 85 mrad, a very low dose compared to that employed in mammography. The phase map provides as well the phase-shift values, e.g., the phase-shift of the first mass including the acrylic base is found as -1106 radians.

Fig. 5 shows two images of a ACR MAP phantom acquired with the prototype system. The Fig. 5-(left) is a phase-sensitive projection acquired at 100 kVp and a magnification factor of 2. For comparison, the Fig. 5-(right) shows the contact radiograph of the phantom acquired with the same kVp and the same phantom dose. Both images were acquired without any anti-scatter grid. The loss of the attenuation contrast associated with the high tube voltage is responsible for the poor contrast shown in Fig. 5-(right), though the x-ray scatter contributed to the image contrast degradation as well. In contrast, the phase-sensitive projection image in Fig. 5-(left) scores much better in visibilities of the fibers, specks and masses in the phantom.

In order to fully exhibit the phase contrast of phantom components and quantify their projective electron densities, we retrieved the phantom's phase maps. As an example, shown in Fig. 6 is a phase map of an ACR phantom retrieved by applying our PAD-based phase retrieval method to a single phase-sensitive projection acquired with the prototype system. The exposure was at 120 kVp and with an estimated average glandular dose of 0.85

mGy. As is shown in Fig. 6, the ACR-phantom phase map scores 4 fibers, 3 specks group, and 3.5 masses for the feature-visibilities.

To accurately estimate the average glandular doses involved in experiments, we extended our previously published tables of the normalized average glandular doses (D_{gN}) for conventional mammography to high-energy x-ray imaging. We performed the Monte Carlo simulations of x-ray transport and energy deposition in breast for photon energies ranging up to 150 keV. The D_{gN} -values for each of photon energies were then weighted according to the measured x-ray spectrum (at 100, 120 and 140 kVp respectively) to computed the D_{gN} -values associated with each of the x-ray spectra. In this way we found the average glandular dose is the 0.85 mGy for the image shown in Fig. 6. While this dose is likely overestimated because of the tube-voltage ramping effects, this overestimated dose value is still very low compared to the phantom dose levels of 1.5-2.5 mGy commonly employed in conventional mammography. The Konica mammography CR-plate detector employed in the experiment is really not quantum-efficient for this experiment, because its thin scintillator layer is designed for mammography, not suitable for high tube-voltage imaging with such as 120 kVp used in this experiment. More contrast-to-noise ratio (CNR) enhancement and dose-savings can be achieved in future by using a high-resolution detector with improved quantum-efficiencies. In fact, a high-resolution flat panel detector with higher quantum-efficiencies has been planned for future experiments.

Moreover, the ACR-phantom phase map in Fig. 6 provides as well phase-shift values. From Fig. 6 we found that the retrieved phase-shift of the first mass including the acrylic base is -1106 radians. Note that x-ray phase-shift should be of a negative value. A more negative value indicates a larger projected electron density. Compared to the first mass, the retrieved phase-shift of the phantom's acrylic frame differs by -35 radians, and the phase-shift of the wax-insert (including the acrylic substrate) differs by +10 radians. To check the accuracies of these retrieved phase values, we computed phase-shifts based on the ray-tracing through a digital model of the ACR MAP phantom. Compared to the ray-tracing based phase-shift value of the first mass, the phase value of the acrylic frame differs by -36 radians, and the phase value of the wax-insert differs by +8 radians. These results are in excellent agreement with the phase retrieval results. However, the first mass's phase value computed based on the ray-tracing is -887 radians, which differs from its retrieved phase value by 20%. This difference may be due to the uncertainty in the average photon energy caused by the tube-voltage ramping in the experiment, and the accuracy can be improved with better exposure control. In a summary, the study shows that the phase-retrieval based high-kVp phase-sensitive projection technique is able to significantly reduce radiation doses and to enable quantitative imaging based on the retrieved phase-shit values.

Extending this study, we also found a novel way to determine the breast density by using the retrieved phase-shift values of a breast. The volumetric breast density (VBD) is the fraction of the volume of fibroglandular tissue in the breast. High breast density inferred from mammograms is associated with two- to four-fold increase in the risk for breast cancer. Public awareness of breast density being as a high risk factor pushes many states passing breast density notification legislations for breast imaging. Current mammography-based method for VBD-measurement is based on small differences in the linear attenuation coefficients of breast fibroglandular tissue and adipose tissue. But breast linear attenuation coefficients vary in a complicated way with different tube targets, filtrations and operating voltages. Hence one has to measure VBD with simultaneous exposure of a calibration phantom alongside the breast for system calibrations. Other methods require laborious system calibrations with different tube targets/filters and voltages. Note that current digital breast tomosynthesis is unable to provide the VBD either, since the limited angular projections in tomosynthesis cannot recover the breast linear attenuation coefficients from the image reconstruction. Instead of measuring tissues' linear attenuation coefficients as a surrogate of the breast density, we recently developed for the first time an x-ray phase-shifts based method of breast density measurement. In order to measure VBD, we developed an x-ray phase-shifts-based method of breast density measurement. We found that the retrieved breast phase map from a single projection can be used to compute the VBD as $VBD = \left\{ \sum_r \left(-\varphi(\vec{r}) / \langle \lambda \rangle r_e - \rho_{e,ad} T_c \right) \right\} \Big/ \left[N_p T_c \left(\rho_{e,fg} - \rho_{e,ad} \right) \right]$, where $\varphi(\vec{r})$ denotes the retrieved breast phase map, and T_c is the breast compression thickness, $\rho_{e,fg} = 3.448 \times 10^{23} / \mathrm{cm}^3$ and $\rho_{e,ad} = 3.108 \times 10^{23} / \mathrm{cm}^3$ are the electron densities of the fibroglandular tissue and adipose tissue, respectively. We have numerically validated this novel method of breast density measurement with very good accuracies. For details, refer to [Wu, Yan, Liu. 2012].

Study on contrast-to-noise ratios with a contrast detail phantom

We investigated the effect of phase retrievals on the contrast-to-noise ratios (CNRs) with a contrast-detail phantom (CD-Phantom). Shown in Fig. 7-(left) is the phase contrast projection image of the CD-phantom acquired at 120 kVp and with a magnification factor of 2.5.
In Fig.7-(left) the phase contrast is exhibited as the enhanced edges of the test-disks. Using the PAD-based method as described earlier, we performed phase retrieval from the phantom's phase contrast image. The retrieved phase map of the CD-phantom is shown in Fig. 7-(right). We measured the bulk CNRs with the disk boundaries excluded in both the images. We found that the disk CNRs in the phase map (Fig. 7-(right)) are greatly enhanced, and are about four-times the disk CNRs in the phase contrast image (Fig. 7-(left).) The CNR of a given disk is proportional to the square root of the radiation dose used in exposure. Hence the PAD-based phase retrieval has good potential of greatly reducing radiation doses for achieving a given CNR-level.

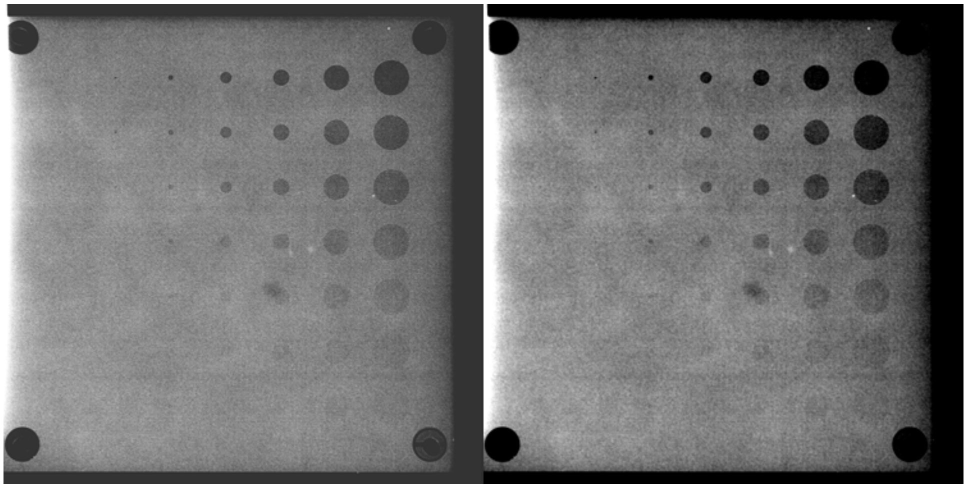

Fig. 7. (left) Phase contrast projection image of a contrast detail phantom acquired at 120 kVp. (right) Retrieved phase map from the acquired phase contrast image.

Study on the PAD-phase retrieval performance at a synchrotron facility

In a collaborative research with Dr. T. Xiao group of Shanghai Institute of Applied Physics, we investigated the performance of the PAD-based phase retrieval method in the phase tomography. Shown in Fig. 8(a-b) are the tomograms of a slice of a four-component phantom. The image in Fig. 8(a) is reconstructed directly from 900 phase-contrast angular projections, which were acquired with 60-keV of synchrotron radiation by Xioa group, using the standard filtered backprojection (FBP) algorithm. The strong edge-enhancement demonstrated in Fig. 8(a) is resulted from the phase contrast. However, high noise-levels are found in this image as well. On the other hand, the image in Fig. 8(b) is the tomogram that is FBP-reconstructed from 900 angular phase-maps, which were retrieved from the same projection set by using the PAD-based phase retrieval method. Apparently the tomogram Fig. 8(b) reconstructed from the angular phase-maps demonstrates much higer bulk CNRs for sample components. Actually the bulk CNRs in Fig. 8(b) are about ten to fifteen times higher than that in Fig. 8(a). The striking bulk CNR enhancement achieved by using the PAD-based method in this experiment shows again that the PAD-based phase retrieval method has good potential to tremendously reduce the radiation doses involved in imaging. For details, please refer to [Liu et al. 2012].

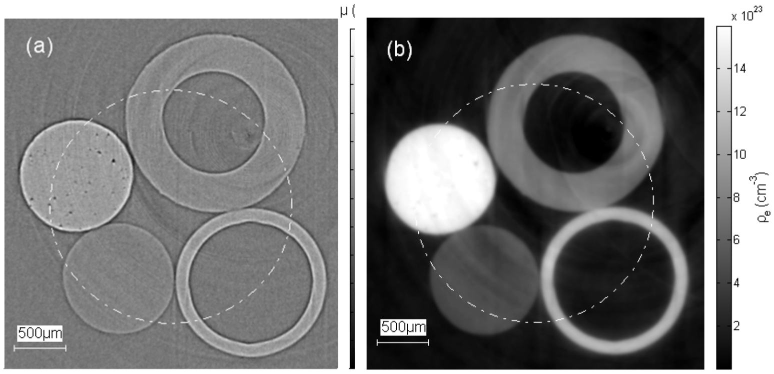

Fig. 8. Reconstructed tomograms of a sample slice at 60 keV. The white dash-dot circles in the two images are the markers. (a) Tomogram reconstructed directly from 900 phase-contrast angular projections. (b) Tomogram reconstructed from 900 angular phase-maps retrieved by using the PAD-based phase retrieval method.

Key Research Accomplishments

- Designed and built a high-voltage x-ray imaging prototype that enables x-ray phase imaging and radiation dose reduction, as is demonstrated in phantom imaging.

- Developed an innovative phase-attenuation duality based (PAD-based) method, which greatly facilitating the low doe phase retrieval for soft tissue body parts such as breast.

- With phantom imaging we demonstrated that the PAD-based phase retrieval greatly enhance the contrast-to noise ratios of images, hence it has good potential for reducing radiation doses in breast imaging.

- Developed a robust general phase retrieval method, the attenuation-partition based (AP-based) method for general clinical imaging. This method was demonstrated to be superior to the mostly used phase retrieval method in literature (TIE-based method) in performing robust phase retrieval for low-dose imaging.

- Advancing the understanding of the image contrast mechanism in phase contrast tomography, we derived a general formula relating the apparent linear attenuation coefficients to the sample's linear attenuation coefficients and refractive indices in phase contrast tomography.

- Considering the high breast density is one of the biggest risk factors for breast cancer, we proposed for the first time an x-ray phase-shifts based method of breast density measurement, as a quantitative imaging application of the phase imaging.

Reportable Outcomes

We have published seven papers in peer-reviewed journals to report the research results from this project and presented the works in national conferences as well.

Peer-Reviewed Journal Article:

Wu X and Yan A. 2009. Phase retrieval from one single phase contrast x-ray image, *Optics Express* 17, 11187-11196.

Yan A, Wu X, Liu H. 2010. Performance analysis of the attenuation-partition based iterative phase retrieval algorithm for in-line phase-contrast imaging, Optics Express 18: 16074-16089.

Yan A and Wu X. 2011. Apparent linear attenuation coefficients in phase contrast x-ray tomography, Nuclear Instruments and Methods in Physics Research, B 269 1841-1843.

Yan A, Wu X, Liu H. 2011. Robustness of phase retrieval methods in x-ray phase contrast imaging: A comparison, Medical Physics 38: 5073-5080.

Wong M, Wu X, Liu H. 2011. The effects of x-ray beam hardening on detective quantum efficiency and radiation dose, Journal of X-Ray Science and Technology 19: 509-519. (In Appendix 5)

Wu X, Yan A, Liu H. 2012. X-ray phase-shifts-based method of volumetric breast density measurement, Medical Physics 39: 4239-4244.

Liu H, Ren Y, Guo H, Xue Y, Xie H, Xiao T, Wu X. 2012. Phase retrieval for hard X-ray computed tomography of samples with hybrid compositions, Chinese Optics Letters 10: 12110 1-4.

Published Abstract and Conference Presentation:

X. Wu, A. Yan , H. Liu: “Contrast mechanism and origin of artifacts in phase-sensitive x-ray volumetric imaging”, *Medical Physics* 36: 2785 (2009).

X. Wu, A. Yan , H. Liu: “Contrast mechanism and origin of artifacts in phase-sensitive x-ray volumetric imaging.” Oral Presentation at the 51st Annual Meeting of the American Association of Physicists in Medicine, July 29, 2009, Anaheim, California

X. Wu**,** A. Yan, H. Liu, Improving robustness of phase retrieval in x-ray phase contrast imaging, Medical Physics 37: 3357 (2010)

X. Wu, A. Yan , H. Liu, “Improving robustness of phase retrieval in x-ray phase contrast imaging,” Oral Presentation at the 52nd Annual Meeting of the American Association of Physicists in Medicine, July 19, 2010, Philadelphia, PA.

A. Yan, X. Wu, M. A. Yan, X. Wu, and H. Liu: Development of a prototype phase-sensitive x-ray breast imaging system”, DoD Breast Cancer Research Program Era of Hope 2011 Conference, Aug. 3-Aug. 5, 2011, Orlando, Florida.

H. Liu H, X. Wu: Development and characterization of phase sensitive x- ray imaging systems, The 53rd Annual Meeting of the American Association of Physicists in Medicine, July 31-Aug. 4, 2012, Vancouver, Canada.

Conclusion

Aiming to develop a low-dose and quantitative x-ray phase imaging technique for facilitating breast cancer detection, in this project we designed and built a high-voltage x-ray imaging prototype that enables x-ray phase imaging and radiation dose reduction, as is demonstrated in phantom imaging. We developed an innovative phase attenuation duality based (PAD-based) method, which greatly facilitating the low doe phase retrieval for soft tissue body parts such as breast. The phantom imaging demonstrated that the PAD-based phase retrieval greatly enhance the contrast-to noise ratios of images, hence it has good potential for reducing radiation doses in breast imaging. We also developed a robust general phase retrieval method, the attenuation-partition based (AP-based) method for general clinical imaging. This method was demonstrated to be superior to the mostly used phase retrieval method in literature (TIE-based method) in performing robust phase retrieval for low-dose imaging. Advancing the understanding of the image contrast mechanism in phase contrast tomography, we derived a general formula relating the apparent linear attenuation coefficients to the sample's linear attenuation coefficients and refractive indices in phase contrast tomography. Considering the high breast density is one of the biggest risk factors for breast cancer, we proposed for the first time an x-ray phase-shifts based method of breast density measurement, as a quantitative imaging method of the phase-sensitive breast imaging. These results obtained and the techniques developed in this project contribute significantly to advancing the development of phase-sensitive low-dose and quantitative breast imaging.

References:

Allen L and Oxley M. 2001. Phase retrieval from series of images obtained by defocus variation, Optics Communications 199: 65-75.

Wu X and Liu H. 2004. A new theory of phase-contrast x-ray imaging based on Wigner distributions. *Medical Physics* 31, 2378-2384.

Wu X, Liu H, Yan A. 2005. X-ray phase-attenuation duality and phase retrieval, Optics Letters 30: 379-381.

Wu X and Yan A. 2009. Phase retrieval from one single phase contrast x-ray image, *Optics Express* 17, 11187-11196.

Yan A, Wu X, Liu H. 2010. Performance analysis of the attenuation-partition based iterative phase retrieval algorithm for in-line phase-contrast imaging, Optics Express 18: 16074-16089

Yan A and Wu X. 2011. Apparent linear attenuation coefficients in phase contrast x-ray tomography, Nuclear Instruments and Methods in Physics Research, B 269 1841-1843.

Yan A, Wu X, Liu H. 2011. Robustness of phase retrieval methods in x-ray phase contrast imaging: A comparison, Medical Physics 38: 5073-5080.

Wong M, Wu X, Liu H. 2011. The effects of x-ray beam hardening on detective quantum efficiency and radiation dose, Journal of X-Ray Science and Technology 19: 509-519.

Wu X, Yan A, Liu H. 2012. X-ray phase-shifts-based method of volumetric breast density measurement, Medical Physics 39: 4239-4244.

Liu H, Ren Y, Guo H, Xue Y, Xie H, Xiao T, Wu X. 2012. Phase retrieval for hard X-ray computed tomography of samples with hybrid compositions, Chinese Optics Letters 10: 12110 1-4.

Appendices

(1) List of Personnel Receiving Pay From the Research Effort

Xizeng Wu, Ph.D.
Aimin Yan, Ph.D.
Hong Liu, Ph.D.
Molly Donovan Wong, Ph.D.
Der-yu Kau

(2) List of peer-reviewed journal articles appended for review

Wu, X, Yan, A. 2009. Phase retrieval from one single phase contrast x-ray image, *Optics Express* 17, 11187-11196.

Yan A, Wu X, Liu H. 2010. Performance analysis of the attenuation-partition based iterative phase retrieval algorithm for in-line phase-contrast imaging, Optics Express 18: 16074-16089

Yan A, Wu X. 2011. Apparent Linear Attenuation Coefficients in Phase Contrast X-Ray Tomography, Nuclear Instruments and Methods in Physics Research, B 269 1841-1843.

Yan A, Wu X, Liu H. 2011. Robustness of phase retrieval methods in x-ray phase contrast imaging: A comparison, Medical Physics 38: 5073-5080.

Wong M, Wu X, Liu H. 2011. The effects of x-ray beam hardening on detective quantum efficiency and radiation dose, Journal of X-Ray Science and Technology 19: 509-519.

Wu X, Yan A, Liu H. 2012. X-ray phase-shifts-based method of volumetric breast density measurement, Medical Physics 39: 4239-4244.

Liu H, Ren Y, Guo H, Xue Y, Xie H, Xiao T, Wu X. 2012. Phase retrieval for hard X-ray computed tomography of samples with hybrid compositions, Chinese Optics Letters 10: 12110 1-4.

Phase retrieval from one single phase contrast x-ray image

Xizeng Wu and Aimin Yan
Department of Radiology, University of Alabama at Birmingham, Birmingham, AL 35233, USA
xwu@uabmc.edu, ayan@uabmc.edu

Abstract: Phase retrieval is required for achieving artifact-free x-ray phase-sensitive 3D imaging. A phase-retrieval approach based on the phase-attenuation duality with high energy x-rays can greatly facilitate for phase sensitive imaging by allowing phase retrieval from only one single projection image. The previously derived phase retrieval formula is valid only for small Fresnel propagator phases corresponding to common clinical imaging tasks. In this work we presented a new duality-based phase retrieval formula that can be applied for cases with large Fresnel propagator phases corresponding to high spatial resolution imaging. The computer simulation demonstrated superiority of this new formula over the previous phase retrieval formula in reconstructing the high frequency components of imaged objects. A modified Tikhonov regularization technique has been devised for phase retrieval in cases of very high resolution and large object-detector distance such that some Fresnel propagator phases may be close or greater than π. This new phase retrieval formula lays the foundation for implementing high-resolution phase-sensitive 3D imaging of soft tissue objects.

© 2009 Optical Society of America

OCIS codes: 340.7440 (X-ray imaging); 030.1670 (Coherent optical effects)

References and links

1. S. Wilkins, T. Gureyev, D. Gao, A. Pogany, and A. Stevenson, “Phase-contrast imaging using polychromatic hard X-rays,” Nature **384**, 335 – 338 (1996).
2. A. Snigirev, I. Snigireva, V. Kohn, S. Kuznetsov, and I. Shelokov, “On the possibilities of x-ray phase contrast microimaging by coherent high-energy synchrotron radiation,” Rev. Sci. Instrum. **66**, 5486 – 5492 (1995).
3. K. Nugent, T. Gureyev, D. Cookson, D. Paganin, and Z. Barnea, “Quantitative Phase Imaging Using Hard X Rays,” Phy. Rev. Lett. **77**, 2961 – 2965 (1996).
4. A. Pogany, D. Gao, and S. Wilkins, “Contrast and resolution in imaging with a microfocus x-ray source,” Rev. Sci. Instrum. **68**, 2774 – 2782 (1997).
5. F. Arfelli, V. Bonvicini, and et al, “Mammography with synchrotron radiation: phase-detected Techniques,” Radiology **215**, 286 – 293 (2000).
6. D. Paganin, S. Mayo, T. Gureyev, P. Miller, and S. Wilkins, “Simultaneous phase and amplitude extraction from a single defocused image of a homogeneous object,” J. Microsc. **206**, 33 – 40 (2002).
7. S. Mayo, T. Davis, T. Gureyev, P. Miller, D. Poganin, A. Pogany, A. Stevenson, and S. Wilkins, “X-ray phase-contrast microscopy and microtomography,” Opt. Express **11**, 2289 – 2302 (2003).
8. X. Wu and H. Liu, “A general theoretical formalism for X-ray phase contrast imaging,” J. X-ray Sci. and Tech. **11**, 33 – 42 (2003).
9. X. Wu and H. Liu, “Clinical implementation of phase-contrast x-ray imaging: Theoretical foundations and design considerations,” Med. Phys. **30**, 2169 – 2179 (2003).
10. X. Wu and H. Liu, “A new theory of phase-contrast x-ray imaging based on Wigner distributions,” Med. Phys. **31**, 2378 – 2384 (2004).

#110095 - $15.00 USD Received 14 Apr 2009; revised 20 May 2009; accepted 17 Jun 2009; published 19 Jun 2009

11. E. Donnelly, R. Price, and D. Pickens, "Experimental validation of the Wigner distributions theory of phase-contrast imaging," Med. Phys. **32**, 928 – 931 (2005).
12. D. Zhang, M. Donvan, L. Fajardo, A. Archer, X. Wu, and H. Liu, "Preliminary feasibility study of an in-line phase contrast x-ray imaging prototype," IEEE Trans. Biomed. Eng. **55**, 2249 – 2257 (2008).
13. X. Wu, H. Liu, and A. Yan, "X-ray phase-attenuation duality and phase retrieval," Opt. Lett. **30**(4), 379 – 381 (2005).
14. X. Wu and H. Liu, "X-Ray cone-beam phase tomography formulas based on phase-attenuation duality," Opt. Express **13**, 6000 – 6014 (2005).
15. P. Cloetens, R. Mache, M. Schlenker, and S. Lerbs-Mache, "Quantitative phase tomography of Arabidopsis seeds reveals intercellular void network," PNAS **103**, 14,626 – 14,630 (2006).
16. X. Wu, H. Liu, and A. Yan, "Phase-Contrast X-Ray Tomography: Contrast Mechanism and Roles of Phase Retrieval," Eur. J. Radiology **68**, S8 – S12 (2008).
17. J. Guigay, M. Langer, R. Boistel, and P. Cloetens, "Mixed transfer function and transport of intensity approach for phase retrieval in the Fresnel region," Opt. Lett. **32**, 1617 – 1619 (2007).
18. ICRU, "Tissue Substitutes in Radiation Dosimetry and Measurement," in *Report 44 of the International Commission on Radiation Units and Measurements* (Bethesda, MD, 1989).
19. N. Dyson, *X-Rays in Atomic and Nuclear Physics* (Longman Scientific and Technical, Essex, UK, 1973).
20. T. Gureyev, Y. Nesterets, D. Paganin, A. Pogany, and S. Wilkins, "Linear algorithms for phase retrieval in the Fresnel region. 2. Partially coherent illumination," Opt. Comm. **259**, 569 – 580 (2006).
21. M. Born and E. Wolf, *Principles of Optics*, 6th ed. (Pergamon, Oxford, 1980).
22. F. Meng, H. Liu and X. Wu, "An iterative phase retrieval algorithm for in-line phase imaging," Opt. Express **15**, 8383 – 8390 (2007)
23. M. Langer, P. Cloetens, J.P. Guigay and F. Peyrin, "Quantitative comparison of direct phase retrieval in in-line phase tomography," Med. Physics **35**, 4556 – 4566 (2008)
24. A. Yan, X. Wu and H. Liu, "An attenuation-partition based iterative phase retrieval algorithm for in-line phase-contrast imaging" Opt. Express **16**, 13330 – 13341 (2008)

---

1. Introduction

Conventional x-ray imaging for soft tissues (such as breast, brain, liver, etc.) is limited in its sensitivity for detecting subtle tissues pathological changes, since the imaging relies on the small difference in x-ray attenuation between the lesions and soft tissues of variable structure. However, as x-ray wave passes through tissues, x-ray undergoes phase-shifts as well. The amount of x-ray phase shift ϕ by tissues is

$$\phi(\vec{r}) = -\left(\frac{hc}{E}\right) r_e \int \rho_e(\vec{r},z)dz = -\left(\frac{hc}{E}\right) r_e \rho_{e,p}(\vec{r}), \tag{1}$$

where r_e is the classical electron radius, h is the Plank constant and c the speed of light, E is x-ray photon energy. Here ρ_e denotes tissue electron density, and the integration of electron density ρ_e is over the x-ray path and the integral is the projected electron density $\rho_{e,p}$ [1, 2, 3]. It turns out that x-ray phase-shift differences between tissue and lesions are about one thousand times larger than their attenuation differences [1, 2, 3]. Hence the phase-sensitive imaging has the potential to greatly enhance the lesion detection sensitivity and specificity, and reduce the radiation dose associated with x-ray imaging. In the inline phase contrast imaging as studied in previous works, the x-rays with shifted phases diffract from the object to the detector, and the diffracted x-rays form bright and dark fringes at tissue boundaries. The edge enhancement thus generated relies on the spatial coherence of the x-ray source, and Laplacian and gradients of x-ray phase-shifts caused by the object, and gradients of the objects attenuation [4, 5, 6, 7, 8, 9, 10, 11, 12, 13, 14]. The procedure of disentangling tissue phase-shifts from the mixed contrast mechanism and retrieving the phase maps from acquired phase contrast images is called the phase retrieval. Phase retrieval technique plays a central role in phase-sensitive x-ray imaging. By means of phase retrieval, one can reconstruct a quantitative map of phase-shifts, a phase image of the imaged object [3, 6, 13, 15, 16]. According to Eq. (1), a retrieved phase image is equivalently a map of imaged objects quantitative projected electron densities. Therefore, tissue phase images can provide quantitative tissue characterization,

#110095 - $15.00 USD Received 14 Apr 2009; revised 20 May 2009; accepted 17 Jun 2009; published 19 Jun 2009

which potentially can increase the sensitivity and specificity of a diagnosis. Moreover, phase retrieval is a necessary procedure for phase-sensitive volumetric imaging such as the phase-sensitive tomography and tomosynthesis [7, 14, 15]. In the phase-sensitive imaging, x-ray does NOT propagate along straight lines because of x-ray refraction and diffraction at tissue interface and boundaries. The diffraction fringes generated by phase contrast at tissue interfaces will obviously render conventional volumetric image reconstruction methods erroneous, since conventional volumetric reconstruction methods assume that x-rays propagate along straight lines. The phase-sensitive CT experiments showed that conventional tomography reconstruction algorithms applied to phase-contrast projections can lead to erroneous tomography images with artifacts such as the streaks and negative densities [7]. The exact mechanism of the phenomenon was revealed in one of our recent work. In fact, if we denote the imaged objects linear attenuation coefficient by $\mu(\vec{r})$ and its electron density by $\rho_e(\vec{r})$, with the conventional filtered backprojection method the reconstructed "apparent attenuation coefficients" $\mu_{\text{recon}}(\vec{r})$ was found as [17]:

$$\mu_{\text{recon}}(\vec{r}) = \mu(\vec{r}) - R_2 \cdot \frac{r_e \lambda^2}{2\pi} \cdot \left(\frac{\partial^2}{\partial x^2} + \frac{\partial^2}{\partial y^2} + \frac{\partial^2}{\partial z^2} \right) \rho_e + \mu_{\text{mixed}}(\vec{r}), \tag{2}$$

where R_2 denotes the object-detector distance, λ the x-ray wavelength. Eq. (2) shows that the reconstructed tomogram consists of three sub-tomograms. The first sub-tomogram is the tomogram of the tissue linear attenuation coefficients $\mu(\vec{r})$. The second sub-tomogram is a scaled map of the 3-D Laplacian of tissue electron densities. The third sub-tomogram $\mu_{\text{mixed}}(\vec{r})$ represents the artifacts reflecting the global variation of both $\mu(\vec{r})$ and $\rho_e(\vec{r})$, but is not representing the local variations of $\mu(\vec{r})$ and $\rho_e(\vec{r})$. It is this term that causes artifacts such as the streaks in reconstruction images. In order to correctly deal with volumetric reconstruction issue, as a general strategy one should first disentangle tissue phase-shifts from the mixed contrast mechanism from acquired phase-sensitive projections and retrieve the phase maps for all projections, then reconstruct the 3D images of object attenuation coefficients and electron densities, respectively.

For phase retrieval one in general needs to acquire at least two and mostly four to five images with different object-detector distances [3, 15]. This requirement is imposed by the x-ray wave nature and its wave equation [3, 8, 9, 10]. Multiple image-acquisitions for a phase retrieval increase radiation dose associated with the technique. For phase sensitive tomography or tomosynthesis, multiple image-acquisitions for each projection-angle make phase-sensitive tomography and tomosynthesis implementation especially cumbersome: multiple phase-contrast images have to be acquired with different object-detector distances for all the projections during a scan, and the number of required projections can be as high as one thousand. In addition, the image data alignment procedure is quite time-consuming. Moreover, radiation dose is multiplied for multiple image acquisition per projection view as well. Therefore, an important challenge is to find an effective and low-dose approach for phase retrievals for phase-sensitive imaging. Many studies were conducted addressing this challenge [6, 13, 14]. We proposed a unique solution for phase-sensitive imaging with high energy x-rays. We noted that with increasing x-ray energy tissues photoelectric absorption decreases as $1/E^n$ with $n \approx 3-4$. but tissues phase shift decreases much slower, and only as $1/E$ as is shown in Eq. (1). Therefore, phase-sensitive imaging with x-rays can fully take advantage of phase contrast and greatly reduce radiation doses associated with x-ray imaging, by taking advantage of the dual relation between the high energy x-rays phase-shifts and attenuation for soft tissues. Furthermore, analyzing the tissue attenuation data, we observed that the soft tissue attenuation cross sections are very well approximate by that of x-ray incoherent scattering for x-rays of about 60 keV to 500 keV. Under this circumstance, we noted that soft-tissue attenuation and soft-tissue phase are all related to the projected electron density, we called this new notion as the phase-attenuation duality. Based

#110095 - $15.00 USD   Received 14 Apr 2009; revised 20 May 2009; accepted 17 Jun 2009; published 19 Jun 2009

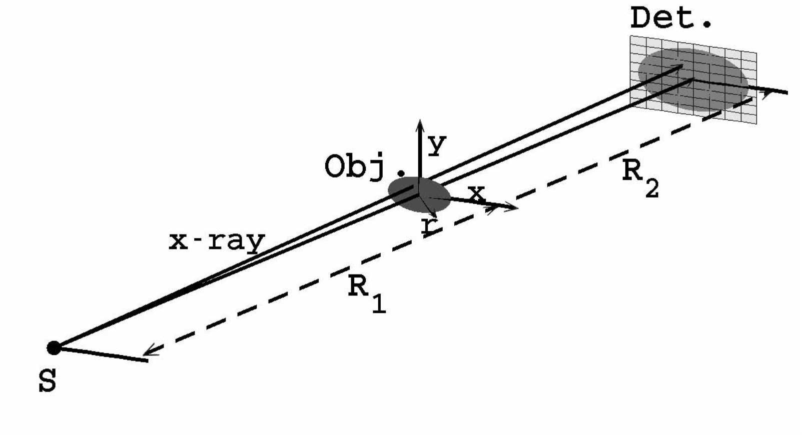

Fig. 1. A shematic diagram for the measuring system

on this concept of phase-attenuation duality, we found a way to retrieve a phase-map from only one single recorded image, that is, the retrieved phase map is given by [13]:

$$\phi(\vec{r}) = \frac{\lambda r_e}{\sigma_{\mathrm{KN}}} \ln \left\{ \left(1 - \left(\lambda^2 r_e R_2/(2\pi M \sigma_{\mathrm{KN}})\right) \nabla^2\right)^{-1} \left(\frac{M^2 I(M\vec{r}; R_1 + R_2)}{I_{\mathrm{in}}} \right) \right\}, \tag{3}$$

where R_1 is the distance from the point x-ray source to object, R_2 is the distance from object to detector, $M = (R_1 + R_2)/R_1$ is the geometric magnification, $\vec{r}$ is the position vector (see Fig. 1.) In Eq. 3, $I(M\vec{r}; R_1 + R_2)$ is the measured image intensity at detector plane, and I_{in} is the intensity at entrance, the operator ∇^2 denotes the Laplacian operator. In Eq. (3) σ_{KN} is the Klein-Nishina total cross section, that is, the total cross section for x-ray Compton scattering with a free electron [17]. Note that σ_{KN} is x-ray energy dependent, as is shown below. We point out that the high sensitivity of x-ray phase change is realized as the high ratio $\lambda r_e/\sigma_{\mathrm{KN}} \gg 1$ in this circumstance. In fact, for clinical imaging photon energy is no higher than 150 keV, and in this case $\lambda r_e/\sigma_{\mathrm{KN}} \sim 10^3$. In other words, with this duality the high sensitivity of phase imaging manifests itself as the high ratio of x-ray wavelength over the classical electron radius. Compared to the common multiple-acquisition based phase retrieval approaches in the literature [3, 6, 15], our duality-based phase retrieval method is a conveniently implemented method with tremendous dose-saving for many potential applications such as mammography. These advantages will be critical for phase-sensitive volumetric imaging such as breast tomosynthesis and computed tomography.

However, there is a limitation on applicability of the phase retrieval formula Eq. (3). In fact. Eq. (3) is not valid for the cases with very high spatial resolution and with large object-detector distances. The physics behind this can be intuitively explained as follows. In fact, in inline phase-sensitive imaging the phase contrast is formed by the diffraction from the object to the detector of x-rays with shifted phases. The Fresnel diffraction can be thought as a x-ray wave-front filtering with the Fresnel propagator $\exp(i\pi\lambda z\vec{u}^2)$, where λ is the wavelength and $\vec{u}$ is the wave-front transverse spatial frequency vector, and $z = R_2/M$ in terms of the parameters in Eq. (3). So the phase of the propagator, i.e. $\pi\lambda z\vec{u}^2$, determines how strongly the wave-front exit from the object will be diffracted in x-ray propagation. The phase retrieval formula Eq. (3) was derived by linearizing Fresnel propagator phase under the assumption of $\pi\lambda z\vec{u}^2 \ll 1$ [8, 13]. This linearizing is equivalent to simplifying x-ray wave equation of motion to the transport of intensity of equation (TIE) [8]. However, for cases with very high spatial resolution and with

#110095 - $15.00 USD Received 14 Apr 2009; revised 20 May 2009; accepted 17 Jun 2009; published 19 Jun 2009

large object-detector distances, such as cases with phase-sensitive imaging experiments with synchrotron based x-ray sources, or the high resolution imaging experiments with biological specimen or small animals, the high spatial resolution or large propagation distances make Fresnel propagator phases $\pi\lambda z\vec{u}^2$ larger than 1 for many transverse spatial frequencies of x-ray wave-front. For example, for 60 keV x-rays, if $M = 1$ and $R_2 = 2$m, detector pixel is 5 μm, then $\pi\lambda z\vec{u}^2 = 1.299$. For these cases one cannot linearize Fresnel propagators and should consider the full exponential propagators instead. In section 2, we will first briefly review the concept of the phase-attenuation duality and how it greatly simplify the phase retrieval for soft-tissue objects. We will then derive a new and general PA-Duality based phase retrieval formula, as the main result of this work. With this general formula, one can retrieve the phase from one single phase contrast image and is valid for cases involved with large Fresnel propagator phases. Hence this new phase retrieval formula extends its applicability to cases with very high spatial resolution and with large object-detector distances. In section 3, we show the simulation results with the general formula for phase retrieval.

2. Phase-attenuation duality and phase retrieval from one single phase contrast image for soft tissue objects

As is explained in previous works [3, 4, 8, 9, 10], in phase-sensitive imaging the imaged object can be modeled by a two-dimensional transmission function $T(\vec{r}) = A_0(\vec{r})e^{i\phi_0(\vec{r})}$, where $\phi_0(\vec{r})$ denotes the x-ray phase-shift caused by the object, and $A_0(\vec{r})$ denotes the x-ray transmission, or the attenuation-map of object. For sake of clarity in exploring the effects of non-linearity of the Fresnel propagators, we assume the x-ray source is a quasi-monochromatic point source in following derivations. We will discuss more general x-ray sources in section 3.

Let R_1 denote the source-object distance and R_2 the object-detector distance. The geometric magnification factor M is equal to $(R_1 + R_2)/R_1$. We also assume that one encounters only moderate variation of the object phase function $\phi(\vec{r})$ such that $|\phi(\vec{r} + \lambda R_2\vec{u}/2M) - \phi(\vec{r} - \lambda R_2\vec{u}/2M)| \ll 1$ [3]. Transmitting from the object, x-rays undergo attenuation and phase-shift, and diffract over a distance R_2 to the detector. An important task is to find out the formula of the image intensity as function of the objects transmission function and imaging geometry. A general solution had been found in one of our previous works [3]. Starting from the paraxial Fresnel-Kirchhoff diffraction theory, we found out in this work that the Fourier transform of x-ray irradiance at detector plane is given by:

$$\hat{\mathscr{F}}\left(I(\vec{r}_D)\right) = \frac{I_{\text{in}}}{M^2}\left\{\cos\left(\frac{\pi\lambda R_2\vec{u}^2}{M}\right)\left(\hat{\mathscr{F}}\left(A_0^2\right) - i\frac{\lambda R_2}{M}\vec{u}\cdot\hat{\mathscr{F}}\left(\phi\nabla A_0^2\right)\right) + \right.$$
$$\left. + 2\sin\left(\frac{\pi\lambda R_2\vec{u}^2}{M}\right)\left(\hat{\mathscr{F}}\left(A_0^2\phi\right) + i\frac{\lambda R_2}{4M}\vec{u}\cdot\hat{\mathscr{F}}\left(\nabla A_0^2\right)\right)\right\}, \qquad (4)$$

where $I(\vec{r}_D)$ denotes the x-ray irradiance at the detector entrance, and the symbol $\hat{\mathscr{F}}(\cdot)$ denotes the 2-D Fourier transform and I_{in} is the intensity of the incident x-ray upon the object, and $\vec{u}$ is the spatial frequency vector in the object plane. Note that the Fresnel propagator phases $\pi\lambda R_2\vec{u}^2/M$ enter Eq. (4) as the argument of sinusoidal transfer functions. For cases with moderate spatial resolutions $\vec{u}$ and R_2 , Eq. (4) is much simplified, and the inverse Fourier transformation of the simplified Eq. (4) can be written as [8]:

$$I(\vec{r}; R_1 + R_2) = \frac{I_{\text{in}}}{M^2}\left\{A_0^2\left(\frac{\vec{r}}{M}\right) - \frac{\lambda R_2}{2\pi M}\nabla\cdot\left(A_0^2\nabla\phi\left(\frac{\vec{r}}{M}\right)\right)\right\}. \qquad (5)$$

Equation (5) is the TIE-based formula for image irradiance, which was first derived by Nugent and colleagues[3]. Recently Guigay et al showed the limitations of Eq. (5) with theoretical analysis and experiments [17]. They found that for in-line phase-sensitive imaging with long R_2 and high resolutions such that $\pi\lambda R_2\vec{u}^2/M > 1$, the phase retrieval based on Eq. (5) would be inaccurate, one has to use the general formula Eq. (4) for accurate quantitative phase imaging.

Furthermore, we note that soft tissues encountered in clinical imaging are composed almost exclusively by atoms of the light elements with the atomic numbers $Z < 10$. For example, the composition of breast tissue consists mainly of light elements such as hydrogen, carbon, nitrogen and oxygen. In contrast, the sum of weight fractions of other heavier elements in breast tissue is only less than 1% [18]. The same is true for other soft tissues such as the brain grey/white matter [18]. Analyzing the tissue attenuation data, we observed that the soft tissue attenuation cross sections are very well approximated by that of x-ray incoherent scattering for x-rays of about 60keV to 500keV[19]. In addition, the incoherent scattering functions become linearized as well [19]. Under this circumstance, while the phase-shift is caused by the coherent x-ray scattering, but soft tissue attenuation is determined by the incoherent x-ray scattering for soft tissues, so both the x-ray phase-shift and attenuation by soft tissues are all determined by the projected electron density for these high energy x-rays. We called this complementary relationship between phase-shift and attenuation for soft tissues as the phase-attenuation duality. When the P-A duality holds, x-ray attenuation and phase shift by the object is related in following way:

$$\phi(\vec{r}) = -\lambda r_e \rho_{e,p}(\vec{r}), \qquad A_0^2(\vec{r}) = \exp(-\sigma_{\mathrm{KN}}\rho_{e,p}(\vec{r})), \tag{6}$$

where σ_{KN} is the total cross section for x-ray Compton scattering with a free electron:

$$\sigma_{\mathrm{KN}} = 2\pi r_e^2 \left\{ \frac{1+\eta}{\eta^2}\left[\frac{2(1+\eta)}{1+2\eta} - \frac{1}{\eta}\ln(1+2\eta)\right] + \frac{1}{2\eta}\ln(1+2\eta) - \frac{1+3\eta}{(1+2\eta)^2} \right\}, \tag{7}$$

where $\eta = E_{\mathrm{photon}}/m_e c^2$, here we denote the photon energy of the primary x-ray beam by E_{photon}, and $m_e c^2$ is the rest electron energy and equal to 511keV. The duality condition can be used to simplify Eq. (4). In fact, we can rewrite Eq. (4) as

$$\begin{aligned} \hat{\mathscr{F}}\left(I(\vec{r}_D)\right) = \frac{I_{\mathrm{in}}}{M^2}\Bigg\{ &\cos\left(\frac{\pi\lambda R_2\vec{u}^2}{M}\right)\left[\hat{\mathscr{F}}\left(A_0^2\right) - \frac{\lambda R_2}{2\pi M}\hat{\mathscr{F}}\left(\nabla\cdot\left(A_0^2\nabla\phi\right)\right)\right] + \\ &+ 2\left[\sin\left(\frac{\pi\lambda R_2\vec{u}^2}{M}\right) - \frac{\pi\lambda R_2\vec{u}^2}{M}\cos\left(\frac{\pi\lambda R_2\vec{u}^2}{M}\right)\right]\hat{\mathscr{F}}\left(A_0^2\phi\right) - \\ &- \frac{\lambda R_2}{4\pi M}\sin\left(\frac{\pi\lambda R_2\vec{u}^2}{M}\right)\hat{\mathscr{F}}\left(\nabla^2 A_0^2\right)\Bigg\}. \end{aligned} \tag{8}$$

Especially with the duality condition we found

$$\begin{aligned} &\hat{\mathscr{F}}\left(\nabla\cdot\left(A_0^2\nabla\phi\right)\right) = \left(-4\pi^2\vec{u}^2\right)\left(\tfrac{\lambda r_e}{\sigma_{\mathrm{KN}}}\right)\cdot\hat{\mathscr{F}}\left(A_0^2\right), \\ &\hat{\mathscr{F}}\left(A_0^2\phi\right) = \lambda r_e \hat{\mathscr{F}}\left(\tfrac{\partial A_0^2}{\partial\sigma_{\mathrm{KN}}}\right) \approx \tfrac{\lambda r_e}{\sigma_{\mathrm{KN}}}\hat{\mathscr{F}}\left(A_0^2 - 1\right). \end{aligned} \tag{9}$$

In Eq. (9) we made an approximation of dropping the negligible contribution of the higher order terms of $\sigma_{\mathrm{KN}}/\lambda r_e$. The approximation is based on $\sigma_{\mathrm{KN}}/\lambda r_e \approx 10^{-3}$, and we assumed $|\phi\left(\vec{r} + \lambda R_2\vec{u}/2M\right) - \phi\left(\vec{r} - \lambda R_2\vec{u}/2M\right)| \ll 1$, moderate variations of object phase shifts. Substituting Eqs. (9) into Eq. (8), we found:

$$\hat{\mathscr{F}}\left(\frac{M^2 I(\vec{r}_D)}{I_{\mathrm{in}}}\right) \approx \left[\cos\left(\frac{\pi\lambda R_2\vec{u}^2}{M}\right) + \left(2\frac{\lambda r_e}{\sigma_{\mathrm{KN}}} + \frac{\pi\lambda R_2\vec{u}^2}{M}\right)\sin\left(\frac{\pi\lambda R_2\vec{u}^2}{M}\right)\right]\cdot\hat{\mathscr{F}}\left(A_0^2\right). \tag{10}$$

Equation (10) is the central result of this work, it is the formula for x-ray irradiance for high resolution soft tissue imaging with high energy x-rays. In the derivation the parameter $\lambda r_e/\sigma_{\mathrm{KN}}$

plays a significant role. It is interesting to note that Gureyev et al obtained a similar result in ref.[20] (Eq.(24)) with the exception that the term $\pi\lambda R_2\vec{u}^2/M$ in Eq. (10) was absent. The differences may lie in the different assumptions made regarding the object transmission functions and x-ray energies. Gureyev and coauthors assumed the objects as single material homogeneous objects [20], but our results are for heterogeneous objects of the light elements imaged with high energy x-rays (60 keV or higher), i.e., for the cases the phase-attenuation duality holds. In addition, in their derivation they separated the slowly and rapidly varying components of the amplitude and phase, and they assumed that the magnitude of the rapidly varying components are much smaller than 1, but we did not make such limiting assumption in derivation of Eq. (10). We stress that the Klein-Nishina cross-section is energy dependent shown in Eq. (7) and $\lambda r_e/\sigma_{\text{KN}}$ is about 1000 for inline x-ray energy range used in diagnostic imaging. This large $\lambda r_e/\sigma_{\text{KN}}$ represents the high sensitivity of phase contrast in tissue differentiation, but it also makes the x-ray irradiance formula Eq. (10) getting very much simplified. It is easy to verify that for the low resolution cases such as those with $\pi\lambda R_2\vec{u}^2/M \ll 1$, Eq. (10) is reduced to

$$\hat{\mathscr{F}}\left(\frac{M^2 I(\vec{r}_D)}{I_{\text{in}}}\right) = \left(1 + 2\left(\frac{\lambda r_e}{\sigma_{\text{KN}}}\right)\left(\frac{\pi\lambda R_2\vec{u}^2}{M}\right)\right)\cdot\hat{\mathscr{F}}\left(A_0^2\right), \tag{11}$$

we recover our previous result as shown in [13]. On the other hand, for general cases $\pi\lambda R_2\vec{u}^2/M \sim 1$ or $\pi\lambda R_2\vec{u}^2/M > 1$ Eq. (11) cannot be applied, and one should use Eq. (10) for phase retrieval as is shown below.

3. Simulation results

Comparing Eq. (10) and Eq. (11) for use in performing phase retrieval, the only difference lies in the inverse filters derived for retrieving $\hat{\mathscr{F}}\left(A_0^2\right)$. For phase retrieval based on Eq. (10) the inverse filter is found as

$$\frac{1}{\cos(\alpha) + (2\gamma+\alpha)\sin(\alpha)} = \frac{1}{\delta\cdot\cos(\alpha_1)}, \tag{12}$$

where $\alpha = \pi\lambda R_2\vec{u}^2/M$, the FT-space Fresnel Propagator phase as defined in section 1, and $\gamma = \lambda r_e/\sigma_{\text{KN}}$, which represents the phase contrast enhancement as explained earlier. $\delta = \sqrt{1+(2\gamma+\alpha)^2}$ and $\alpha_1 = \alpha - \sin^{-1}[(2\gamma+\alpha)/\delta]$. On the other hand, for phase retrieval based on Eq. (11) the inverse filter will be

$$\frac{1}{1+2\gamma\alpha}. \tag{13}$$

Since $\gamma \sim 10^3$, the filters in Eq. (12) and Eq. (13) are close when α is small. When α is getting bigger, close to or greater than π (α_1 close to $\pi/2$), the difference between the two inverse filters is getting bigger. Figure 2 shows a plot of the two filters, with respect to the change of α. The inverse filter in Eq. (12), depicted in Fig. 2 as the solid line, changes the sign when α passes through $k\pi$ (and thus α_1 passes through $(k-1/2)\pi$) and diverges to ∞ when $\alpha_1 = (k-1/2)\pi$, $k = 1,2,\cdots$. On the other hand, the filter in Eq. (13), depicted as the dashed line in Fig. 2, keeps positive and approaches zero as α gets bigger. So the difference of the retrieved phase maps using Eq. (10) and Eq. (11) will be highly dependent on the value of the Fresnel propagator phase $\alpha = \pi\lambda R_2\vec{u}^2/M$.

To demonstrate this phenomenon, we performed two simulations. First, we set the phase shift ϕ to be a sine-function in x direction with period of 32 pixel size and constant in y direction. Assuming the pixel pitch is p μm, the spatial frequency corresponding to ϕ, in x direction, is $\mu_{x0} = 1/32p$ $1/\mu$m. In our simulations, for the purpose of simplification, the magnification M as well as the intensity at entrance, I_{in}, are assumed to be 1. The x-ray photon energy is set

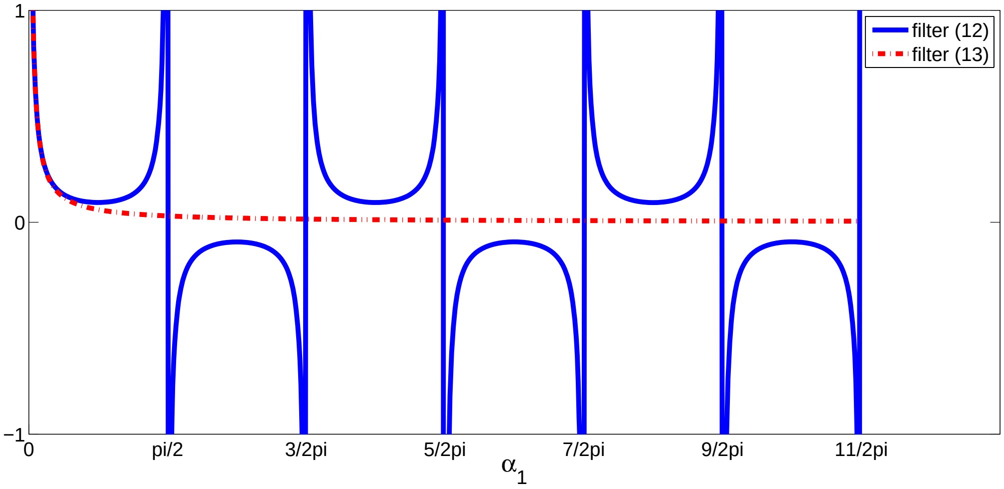

Fig. 2. Plots of filters (13) and (12)

to 60 keV. This gives the x-ray wavelength $\lambda = 2.0667 \times 10^{-11}$ m and the total cross section for x-ray Compton scattering with a free electron $\sigma_{\mathrm{KN}} = 5.4526 \times 10^{-29}$ m^2 as determined from Eq. (7). The classical electron radius r_e is set to 2.82×10^{-15} m. By assuming the detectors resolution $p = 1$ μm and the phase shift $\phi(x,y) = 0.5\sin(32px) - 1$, according to the phase-attenuation duality discussed earlier, the attenuation map is related to the phase map as $A_0^2(x,y) = \exp\left[\sigma_{\mathrm{KN}}/\lambda r_e \cdot \phi\right] = \exp\left[(\sin(32px) - 2)/2\gamma\right]$, with $\gamma = \lambda r_e/\sigma_{\mathrm{KN}} = 1.0726 \times 10^3$. We then performed Fresnel diffraction to determine the phase-contrast image irradiances at distances downstream[21], and the retrieved maps of A_0^2 were found by using the inverse filters of Eq. (12) and Eq. (13), which were derived based on Eq. (10) and Eq. (11), respectively. Because of the large value of γ, phase contrast image irradiances $\{I\}$ were found be maps with each I being dominated by two single frequency component at $u_x = \pm u_{x0}$ ($u_{x0} = 1/32p = 1/32 \times 10^6$ m) plus a zero frequency component. This being so, the shape and variation of the retrieved A_0^2-maps were determined by their dominant frequency component at frequencies $u_x = \pm u_{x0}$. In order to clearly show the differences between phase retrievals based on Eq. (10) and Eq. (11), we examined the ratio of the dominant frequency components of the two retrieved A_0^2-maps based on Eq. (10) and Eq. (11), respectively. We found the ratio being $r = (1 + 2\gamma\alpha)/(\delta \cdot \cos(\alpha_1))$ for a given object-detector distance R_2. This ratio reflects the capability of achieving accurate phase retrieval with Eq. (10) against Eq. (11). For small $\alpha \ll 1$, that is, for small Fresnel propagator phases, this ratio is 1, so Eq. (10) against Eq. (11) both are equally good for the accurate phase retrieval. However, when α is chosen such that $\cos(\alpha_1)$ is close to 0, this ratio can be very large. For example by setting $R_2 = 49.55$ m, we have α mentioned above equals to π, the ratio $r = (1 + 2\gamma)/(\delta \cdot \cos(\alpha_1)) \approx 6700$. This large ratio means that the retrieved A_0^2-map based on Eq. (11) has diminished image-contrast and erronous values, as is shown in Fig.3(c). The phase retrieval result based on Eq. (10), shown in Fig. 3(d), however is much more accurate. When $R_2 = 49.55$ m, the FT-space Fresnel Propagator phase $\alpha = \pi\lambda R_2 \vec{u}^2/M \approx \pi$. So we have, from Eq. (10), $\hat{\mathscr{F}}\left((M^2/I_{\mathrm{in}})I\right) \approx -\hat{\mathscr{F}}\left(A_0^2\right)$, which is different from the result $\hat{\mathscr{F}}\left((M^2/I_{\mathrm{in}})I\right) \approx \left[1 + 2\pi(\lambda r_e/\sigma_{\mathrm{KN}})\right]\hat{\mathscr{F}}\left(A_0^2\right)$ derived from the conventional TIE prediction (Eq. (11)), which does not hold for such large Fresnel Propagator phases. This phenomenon is shown in Fig. (3)(b), where the intensity I is acquired with Fresnel diffraction, in which the dark-white area in A_0^2 is reversed. Note that the inverse filter in Eq. (12) is singular at $\alpha_1 = (k-1/2)\pi$, $k = 1,2,\cdots$, because of the zero-crossing of $\cos(\alpha_1)$. To deal with the singularity associated with the zero-crossing of $\cos(\alpha_1)$, one should regularize the inverse filter. A common regularization technique is the Tikhonov regularization, which modifies $1/\cos(\alpha_1)$ in the filter of Eq. (12) to $\cos(\alpha_1)/(\cos(\alpha_1)^2+\kappa^2)$, where κ is the Tikhonov regularization parameter. In this specific example of the sinusoidal object, however, since we know $\hat{\mathscr{F}}(I)$ is dominated by frequency-components only at $u_x = \pm u_{x0}$ and $(u,v) = (0,0)$, by setting $\hat{\mathscr{F}}(I) = 0$ at all other frequency points purposely, we can avoid the problem caused by the zero-crossing of the inverse filter.

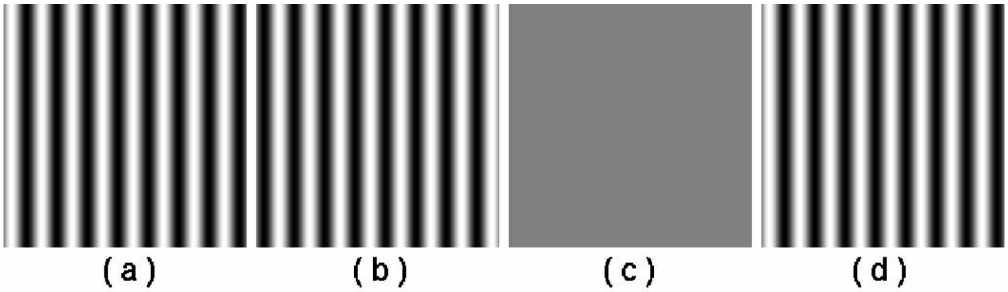

Fig. 3. Comparation of the quality of the retrieved results A_0^2 using Eq. (11) and Eq. (10). $A_0^2 = \exp[\phi/\gamma]$, where phase shift $\phi = 0.5\sin(32px)-1$, pixel pitch $p = 1\mu$m, and object to detector distance $R_2 = 49.55$m. (a) is the true A_0^2; (b) is the phase-contrast intensity image I acquired from Fresnel diffraction; (c) is retrieved A_0^2 using Eq. (11); (d) is retrieved A_0^2 using Eq. (10).

In another simulation, we set all the parameters the same as the previous simulation except replacing the test-object with the well-known Lena image as is shown in Fig. 4(a). The simulation results for the case of $R_2 = 5$ m are shown in Figures 4(c)-4(d). The phase-contrast image I, shown in Fig. 4(b), is acquired with Fresnel diffraction from the object downstream to the detector [21]. Figure 4(c) shows the retrieved image with the inverse filter of Eq. (13), which is based on Eq. (11). Since the filter of Eq. (13) is incorrect when the Fresnel propagator phase α is big, say close or greater than π, the high frequency components of the object was unduly suppressed in the phase-retrieval. This deficiency is reflected in Fig. 4(c) such that the retrieved image gets blurred in locations with high contrast changes, such as the hair, the edge of the hat and body. In contrast, the phase retrieval using the inverse filter of Eq. (12), which is based on Eq. (10), preserves objects high frequency components, as is shown in Fig. 4(d).

As stated above, a regularization must be used to overcome the difficulty associated with the zero-crossing in the denominator of inverse filter in Eq. (13). The zero-crossing occurs obviously at $\alpha_1 = (k-1/2)\pi$, $k = 1,2,\cdots$. The Tikhonov regularization would replace $1/\cos(\alpha_1)$ in the inverse filter of Eq. (13) by the following

$$\frac{\cos(\alpha_1)}{\cos(\alpha_2)^2+\kappa^2}, \tag{14}$$

where κ is a small constant. However, this form of regularization is not optimal since it will deviate from the original inverse filter when α_1 is small. In other words, the test-object's low frequency components would not be fully reconstructed in the retrieval. In order to get around this drawback, we note that the zero-crossing occurs only when α_1 is close or greater than $\pi/2$, while the most low frequency components have $\alpha < 1$. Hence we set the regularization parameter $\kappa = 0$ when α is less than some threshold value α_0, and $\kappa > 0$ when α is greater than

Received 14 Apr 2009; revised 20 May 2009; accepted 17 Jun 2009; published 19 Jun 2009

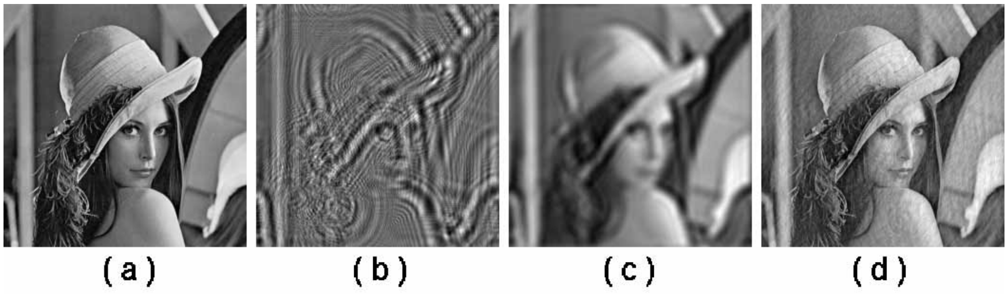

Fig. 4. Comparation of the retrieved results using Eq. (11) and Eq. (10) with $R_2 = 5\text{m}$. (a) is the true A_0^2; (b) is the phase-contrast image I acquired from Fresnel diffraction; (c) is retrieved using Eq. (11); (d) is retrieved using Eq. (10).

α_0. In our simulation, we set this threshold $\alpha_0 = 0.8$, so $\kappa = 0$ when $\alpha < 0.8$, and $\kappa = 0.12$ when $\alpha > 0.8$. We can see from the image in Fig. 4(c) that most of the low frequency information is preserved. On the other hand, the quality of the results can also be numerically determined by computing the error comparing to the true A_0^2 image. By taking the L_2-measure, which is defined as the integrated squared errors, we have the absolute errors for methods (10) and (11) being 0.014 and 0.021 respectively.

4. Conclusions

Phase retrieval is required for achieving artifact-free x-ray phase-sensitive 3D imaging. Multiple image-acquisitions per projection are required in general for phase retrieval [3, 4, 15, 17, 22, 23, 24]. This requirement impedes the implement of x-ray phase-sensitive 3D imaging, especially for phase-sensitive 3D imaging in clinical applications. A phase-retrieval approach based on the phase-attenuation duality with high energy x-rays can greatly facilitate for phase sensitive imaging by allowing phase retrieval from only one single projection image. However, the previously derived phase retrieval formula is valid only for small Fresnel propagator phases corresponding to common clinical imaging tasks. In this work we generalized the previous phase retrieval formula to Eq. (10), which can be applied for cases with large Fresnel propagator phases corresponding to high spatial resolution imaging. The computer simulation demonstrated superiority of this new formula over the previous duality-based phase-retrieval formula in reconstructing the high frequency components of imaged objects. In addition, a modified Tikhonov regularization technique has been devised for phase retrieval in cases of very high resolution and large object-detector distance such that some Fresnel propagator phases may be close or greater than π. This new phase retrieval formula of Eq. (10) lays the foundation for implementing high-resolution phase-sensitive 3D imaging of soft tissue objects.

Acknowledgements

This research was supported in part by the Department of Defense Breast Cancer Research Program under award number W81XWH-08-1-0613.

Performance analysis of the attenuation-partition based iterative phase retrieval algorithm for in-line phase-contrast imaging

Aimin Yan,[1,*] **Xizeng Wu,**[1,*] **and Hong Liu** [2]

[1] *Department of Radiology, University of Alabama at Birmingham,*
Birmingham, AL 35233, USA

[2] *Center for Bioengineering and School of Electrical and Computer Engineering,*
University of Oklahoma, Norman, OK 73019, USA

[*] *Corresponding authors: ayan@uabmc.edu, xwu@uabmc.edu*

Abstract: The phase retrieval is an important task in x-ray phase contrast imaging. The robustness of phase retrieval is especially important for potential medical imaging applications such as phase contrast mammography. Recently the authors developed an iterative phase retrieval algorithm, the attenuation-partition based algorithm, for the phase retrieval in inline phase-contrast imaging [1]. Applied to experimental images, the algorithm was proven to be fast and robust. However, a quantitative analysis of the performance of this new algorithm is desirable. In this work, we systematically compared the performance of this algorithm with other two widely used phase retrieval algorithms, namely the Gerchberg-Saxton (GS) algorithm and the Transport of Intensity Equation (TIE) algorithm. The systematical comparison is conducted by analyzing phase retrieval performances with a digital breast specimen model. We show that the proposed algorithm converges faster than the GS algorithm in the Fresnel diffraction regime, and is more robust against image noise than the TIE algorithm. These results suggest the significance of the proposed algorithm for future medical applications with the x-ray phase contrast imaging technique.

© 2010 Optical Society of America

OCIS codes: 340.7440 (X-ray imaging); 030.1670 (Coherent optical effects)

References and links

1. A. Yan, X. Wu, and H. Liu, "An attenuation-partition based iterative phase retrieval algorithm for in-line phase-contrast imaging," Opt. Express **16**, 13,330 – 13,341 (2008).
2. S. Wilkins, T. Gureyev, D. Gao, A. Pogany, and A. Stevenson, "Phase-contrast imaging using polychromatic hard X-rays," Nature **384**, 335 – 338 (1996).
3. A. Snigirev, I. Snigireva, V. Kohn, S. Kuznetsov, and I. Shelokov, "On the possibilities of x-ray phase contrast microimaging by coherent high-energy synchrotron radiation," Rev. Sci. Instrum. **66**, 5486 – 5492 (1995).
4. K. Nugent, T. Gureyev, D. Cookson, D. Paganin, and Z. Barnea, "Quantitative Phase Imaging Using Hard X Rays," Phy. Rev. Lett. **77**, 2961 – 2965 (1996).
5. A. Pogany, D. Gao, and S. Wilkins, "Contrast and resolution in imaging with a microfocus x-ray source," Rev. Sci. Instrum. **68**, 2774 – 2782 (1997).
6. F. Arfelli, V. Bonvicini, and et al, "Mammography with synchrotron radiation: phase-detected Techniques," Radiology **215**, 286 – 293 (2000).

#126430 - $15.00 USD Received 2 Apr 2010; revised 11 Jun 2010; accepted 9 Jul 2010; published 15 Jul 2010

7. D. Paganin, S. Mayo, T. Gureyev, P. Miller, and S. Wilkins, "Simultaneous phase and amplitude extraction from a single defocused image of a homogeneous object," J. Microsc. **206**, 33 – 40 (2002).
8. S. Mayo, T. Davis, T. Gureyev, P. Miller, D. Poganin, A. Pogany, A. Stevenson, and S. Wilkins, "X-ray phase-contrast microscopy and microtomography," Opt. Express **11**, 2289 – 2302 (2003).
9. X. Wu and H. Liu, "A general theoretical formalism for X-ray phase contrast imaging," J. X-ray Sci. and Tech. **11**, 33 – 42 (2003).
10. X. Wu and H. Liu, "Clinical implementation of phase-contrast x-ray imaging: Theoretical foundations and design considerations," Med. Phys. **30**, 2169 – 2179 (2003).
11. X. Wu and H. Liu, "A new theory of phase-contrast x-ray imaging based on Wigner distributions," Med. Phys. **31**, 2378 – 2384 (2004).
12. E. Donnelly, R. Price, and D. Pickens, "Experimental validation of the Wigner distributions theory of phase-contrast imaging," Med. Phys. **32**, 928 – 931 (2005).
13. D. Zhang, M. Donvan, L. Fajardo, A. Archer, X. Wu, and H. Liu, "Preliminary feasibility study of an in-line phase contrast x-ray imaging prototype," IEEE Trans. Biomed. Eng. **55**, 2249 – 2257 (2008).
14. X. Wu, H. Liu, and A. Yan, "X-ray phase-attenuation duality and phase retrieval," Opt. Lett. **30**(4), 379 – 381 (2005).
15. X. Wu and H. Liu, "X-Ray cone-beam phase tomography formulas based on phase-attenuation duality," Opt. Express **13**, 6000 – 6014 (2005).
16. P. Cloetens, R. Mache, M. Schlenker, and S. Lerbs-Mache, "Quantitative phase tomography of Arabidopsis seeds reveals intercellular void network," PNAS **103**, 14,626 – 14,630 (2006).
17. X. Wu, H. Liu, and A. Yan, "Phase-Contrast X-Ray Tomography: Contrast Mechanism and Roles of Phase Retrieval," Eur. J. Radiology **68**, S8 – S12 (2008).
18. D. Paganin and K. Nugent, "Noninterferometric Phase Imaging with Partially Coherent Light," Phy. Rev. Lett. **80**, 2586 – 2589 (1998).
19. X. Wu and H. Liu, "A dual detector approach for X-ray attenuation and phase imaging," J. X-ray Sci. and Tech. **12**, 35–42 (2004).
20. X. Wu and H. Liu, "Phase-space evolution of x-ray coherence in phase-sensitive imaging," Appl. Opt. **47**, E44 – E52 (2008).
21. M. Teague, "Deterministic phase retrieval: a Green's function solution," J. Opt. Soc. Am. **73**, 1434 – 1441 (1983).
22. T. Gureyev, Y. Nesterets, D. Paganin, A. Pogany, and S. Wilkins, "Linear algorithms for phase retrieval in the Fresnel region. 2. Partially coherent illumination," Opt. Comm. **259**, 569 – 580 (2006).
23. J. Guigay, M. Langer, R. Boistel, and P. Cloetens, "Mixed transfer function and transport of intensity approach for phase retrieval in the Fresnel region," Opt. Lett. **32**, 1617 – 1619 (2007).
24. X. Wu and A. Yan, "Phase Retrieval From One Single Phase Contrast X-Ray Image," Opt. Express p. Opt. Express **17**, 11187 – 11196 (2009).
25. L. Allen and M. Oxley, "Phase retrieval from series of images obtained by defocus variation," Opt. Comm. **199**, 65 – 75 (2001).
26. R. W. Gerchberg and W. O. Saxton, "A practical algorithm for the determination of the phase from image and diffraction plane pictures," Optik **35**, 237 – 246 (1972).
27. J. Fienup, "Reconstruction of an object from the modulus of its Fourier Transform," Opt. Lett. **3**, 27 – 29 (1978).
28. J. Fienup, "Phase retrieval algorithms: a comparison," Appl. Opt. **21**, 2758 – 2769 (1982).
29. N. Dyson, *X-Rays in Atomic and Nuclear Physics* (Longman Scientific and Technical, Essex, UK, 1973).
30. X. Wu, A. Dean, and H. Liu, *Biomedical Photonics Handbook*, chap. 26, pp. 26-1 – 26-34 (CRC Press, Tampa, Fla., 2003).
31. J. H. Hubbell, W. I. Veigele, E. A. Briggs, et al., "Atomic form factors, incohoerent scattering functions, and photon scattering cross sections," Journal of Physical Chemistry Reference Data **4**, 471–538 (1975);
32. L. Rudin, "Images, numerical analysis of singularities and shock filters," Report #TR:5250:87, Caltech, C,S, Dept. (1987).
33. L. I. Rudin, S. Osher, and E. Fatemi, "Nonlinear total variation based noise removal algorithms," Physica D **60**, 259 – 268 (1992).
34. X. Wu, G.T. Barnes and D.M. Tucker, "Spectral dependence of glandular tissue dose in screen-film mammography," Radiology **179**, 143 – 148 (1991).
35. X. Wu, E.L. Gingold, G.T. Barnes and D.M. Tucker, "Normalized average glandular dose in Molybdenum target-Rhodium filter and Rhodium target-Rhodium filter mammography," Radiology **193**, 83 – 89 (1994).
36. J. Seldin and J. Fienup, "Numerical investigation of the uniqueness of phase retrieval," J. Opt. Soc. Am. A **7**(3), 412 – 427 (1990).
37. F. Roddier and C. Roddier, "Wavefront reconstruction using Iterative Fourier transforms," Appl. Opt. **30**, 1325 – 1327 (1991).
38. C. Roddier and F. Roddier, "Wave-front reconstruction from defocused images and the testing of ground-based optical telescopes," J. Opt. Soc. Am. A **10**, 2277 – 2287 (1993).
39. T. Gureyev, A. Roberts, and K. Nugent, "Partially coherent fields, the transport-of-intensity equation, and phase uniqueness," J. Opt. Soc. Am. A **12**, 1942 – 1946 (1995).

#126430 - $15.00 USD Received 2 Apr 2010; revised 11 Jun 2010; accepted 9 Jul 2010; published 15 Jul 2010

40. T. Gureyev and K. Nugent, “Phase retrieval with the transport-of-intensity equation. II. Orthogonal series solution for nonuniform illumination,” J. Opt. Soc. Am. A **13**, 1670 – 1682 (1996).
41. A. Tychonoff and V. Arsenin, *Solution of Ill-posed Problems* (Winston & Sons, Washington, 1977).

---

1. Introduction

Differing from the conventional x-ray imaging, which relies on the small differences in x-ray attenuation changes between tissues variable structure, inline phase contrast imaging is based on the tissues’ phase-shifts diffraction from the object to the detector. Since x-ray phase-shift differences between tissue and lesions are about one thousand times larger than attenuation differences [2, 3, 4], x-ray phase contrast imaging has the potential to enhance the lesion detection sensitivity and specificity, and reduce the radiation dose compared to conventional x-ray imaging. In the inline phase contrast imaging, the diffracted phase-shifts form bright and dark fringes at tissue boundaries and this bright and dark fringes are called edge enhancement. The edge enhancement relies on the spatial coherence of the x-ray source, the Laplacian and gradients of x-ray phase-shifts caused by the tissue, and the gradients of the objects attenuation [5, 6, 7, 8, 9, 10, 11, 12, 13, 14, 15]. One procedure of phase contrast imaging is to disentangle tissue phase-shifts from the mixed contrast mechanism and recover the phase maps from acquired phase contrast images. This procedure is called phase retrieval. Phase retrieval technique plays a central role in phase contrast x-ray imaging. By means of phase retrieval, one can reconstruct a quantitative map of phase-shifts, a phase image of the imaged object [4, 7, 14, 16, 17]. The amount of x-ray phase-shifts ϕ by tissues is determined by

$$\phi(\vec{\mathbf{r}}) = -\left(\frac{hc}{E}\right) r_{\mathrm{e}} \int \rho_e(\vec{\mathbf{r}}, z)\, dz = -\left(\frac{hc}{E}\right) r_{\mathrm{e}} \rho_{\mathrm{e,p}}(\vec{\mathbf{r}}), \tag{1}$$

where r_{e} is the classical electron radius, h the Plank constant, c the speed of light, E the x-ray photon energy, and $\rho_{\mathrm{e,p}}$, the integration of the electron density ρ_e over the x-ray path, is called the projected electron density [2, 3, 4]. So a retrieved phase map is equivalently a map of imaged object’s quantitative projected electron densities. Moreover, phase retrieval is also a necessary procedure for phase-sensitive volumetric imaging, such as the phase sensitive tomography and tomosynthesis, to acquire the artifact free 3D images of object attenuation coefficients and electron densities [8, 15, 16].

Phase retrieval is based on x-ray propagation equation derived either from the Fresnel diffraction or the Wigner distribution based phase-space formalism [5, 18, 9, 19, 20]. To be specific, let $\phi(\vec{\mathbf{r}})$ be the x-ray phase-shift caused by the imaged object, and $A_0(\vec{\mathbf{r}})$ the x-ray transmission, or the attenuation-map of the object. Then the Fourier transform of the x-ray intensity, $\hat{\mathscr{F}}(I)(\vec{u}) = \int_{\mathbb{R}^2} I(\vec{x}) \exp[2\pi i \vec{x} \cdot \vec{u}]\, d\vec{x}$, at position away from the object with distance R_2, of the monochromatic point x-ray source starting at a place away from the object R_1 distance, can be modeled by the following [9]

$$\begin{aligned}
\hat{\mathscr{F}}(I)\left(\frac{\vec{\mathbf{u}}}{M}; R_1 + R_2\right) = I_{\mathrm{in}} \Bigg\{ & \cos\left(\frac{\pi\lambda R_2}{M}\vec{\mathbf{u}}^2\right) \cdot \hat{\mathscr{F}}\left(A_0^2\right) + \\
& + \left[2\sin\left(\frac{\pi\lambda R_2}{M}\vec{\mathbf{u}}^2\right) - \left(\frac{2\pi\lambda R_2}{M}\vec{\mathbf{u}}^2\right) \cdot \cos\left(\frac{\pi\lambda R_2}{M}\vec{\mathbf{u}}^2\right)\right] \cdot \hat{\mathscr{F}}\left(A_0^2\phi\right) - \\
& - \cos\left(\frac{\pi\lambda R_2}{M}\vec{\mathbf{u}}^2\right) \cdot \frac{\lambda R_2}{2\pi M} \cdot \hat{\mathscr{F}}\left(\nabla \cdot \left(A_0^2 \nabla \phi\right)\right) - \\
& - \frac{\lambda R_2}{4\pi M} \sin\left(\frac{\pi\lambda R_2}{M}\vec{\mathbf{u}}^2\right) \cdot \hat{\mathscr{F}}\left(\nabla^2 A_0^2\right) \Bigg\},
\end{aligned} \tag{2}$$

#126430 - $15.00 USD Received 2 Apr 2010; revised 11 Jun 2010; accepted 9 Jul 2010; published 15 Jul 2010
(C) 2010 OSA

where I_{in} is the incident x-ray intensity at R_1, λ the wavelength of the monochromatic point x-ray source and $M = (R_1 + R_2)/R_1$ is the geometric magnification. When the FT-Space Fresnel propagator $\pi\lambda R_2 \vec{u}^2/M \ll 1$, Eq. (2) can be simplified to the Transport of Intensity Equation (TIE) [21, 4, 9]

$$I(\vec{\mathbf{r}}; R_1 + R_2) = \frac{I_{\text{in}}}{M^2}\left\{A_0^2\left(\frac{\vec{\mathbf{r}}}{M}\right) - \frac{\lambda R_2}{2\pi M}\nabla\cdot\left(A_0^2\nabla\phi\right)\left(\frac{\vec{\mathbf{r}}}{M}\right)\right\}. \tag{3}$$

It is worthy to note that Eq. (3) is valid only for moderate resolution images. For high resolution images, i.e. when the FT-Space Fresnel propagator $\pi\lambda R_2 \vec{u}^2/M$ is close or greater than π, any phase retrieval algorithms based on Eq. (3) need to be substituted to Eq. (2) [22, 23, 24]. In this paper, the algorithms discussed are all based on Eq. (3), i.e. the moderate resolution is satisfied.

Numerous algorithms have been suggested on how to effectively recover the phase-shift from the phase contrast images. Among these, two algorithms are most widely used. One is the TIE algorithm implemented by Allen and Oxley in [25]. The other is the GS algorithm developed first by Gerchberg and Saxton in [26] and later improved by Fienup [27, 28]. These two algorithms have both their advantages and disadvantages. The TIE algorithm is a direct approximate method which is fast but is unstable with noisy data; the GS algorithm on the other hand is relatively more stable than the TIE algorithm[25] but the converging speed is slow especially for the field of medical imaging. In [1], the authors developed an Attenuation-Partition Based Algorithm (APBA) based on the phase-attenuation duality property of soft tissues under higher x-ray energy. This algorithm is fast and stable for potential medical imaging. We compared the performance of this algorithm with the TIE algorithm for two groups of data under the condition of medical imaging in [1], including the phase retrieval from phase-contrast images of a breast lumpectomy specimen. In this paper, we will make a systematic analysis about this algorithm and compare its performance with the one of the GS algorithm and the TIE algorithm with simulated data.

The paper is organized as follows. In Section 2, we first summarize the attenuation-partition based algorithm (APBA), which is motivated by our observation of the phase-attenuation duality[14]. Then we give a measure, called total variation, used to evaluate the closeness of two image data. This measure is used as a quantitative standard in comparing the performance between different algorithms in the following section. In Section 3, we first develop a breast specimen model which can reflect the attenuation and phase changes with respect to the x-ray energy change (Section3.1), and then compare the performance of the algorithm with the GS algorithm (Section 3.2) and the TIE algorithm (Section 3.3). Finally, we conclude this paper in Section 4.

2. The attenuation-partition based algorithm (APBA) and an image accuracy measure

2.1. *The Attenuation-Partition Based Algorithm*

The attenuation-partition based algorithm (APBA) is a recently developed iterative algorithm for phase retrieval[1]. It was derived from our previous notion of the phase-attenuation duality[14], and it takes advantage of the correlation between the attenuation and phase-shift for phase retrieval. As is well known, tissue's attenuation change A_0 in the diagnostic x-ray imaging arose from three x-ray and tissue interactions: the photoelectric absorption, the coherent scattering, and the incoherent scattering[29, 30, 9, 14]. However, among the three interactions, the attenuation caused by incoherent scattering A_{KN}, which is dominated by the x-ray Compton scattering, deserves a special attention. This is because both of A_{KN} and the x-ray phase-shift ϕ are determined by the tissue's projected electron density:

$$A_{\text{KN}}(\vec{\mathbf{r}}) = \exp\left[-\frac{\sigma_{\text{KN}}}{2}\rho_{\text{e,p}}(\vec{\mathbf{r}})\right], \qquad \phi(\vec{\mathbf{r}}) = -\lambda r_{\text{e}}\rho_{\text{e,p}}, \tag{4}$$

#126430 - $15.00 USD Received 2 Apr 2010; revised 11 Jun 2010; accepted 9 Jul 2010; published 15 Jul 2010

where λ is the x-ray wavelength, r_e the classical electron radius, $\rho_{e,p}$ the projected electron density as defined in Eq. (1), and σ_{KN} is the total cross section for x-ray Compton scattering with a free electron:

$$\sigma_{KN}(E_{\text{photon}}) = 2\pi r_e^2 \left\{ \frac{1+\eta}{\eta^2} \left[\frac{2(1+\eta)}{1+2\eta} - \frac{1}{\eta} \log(1+2\eta) \right] + \right. \\ \left. + \frac{1}{2\eta} \log(1+2\eta) - \frac{1+3\eta}{(1+2\eta)^2} \right\}, \quad (5)$$

with $\eta = E_{\text{photon}}/m_e c^2$. Here we denote the photon energy of the primary x-ray beam by E_{photon} and $m_e c^2$ is the rest electron energy. Eq.(4) suggests clearly that the x-ray attenuation and phase-shift by tissue has certain correlation. Our idea is to utilize this correlation for facilitating the phase retrieval.

Of course, the extent of this correlation between phase and attenuation depends on the x-rays photon energy as well as the tissues physical composition. For example, for light elements with atomic numbers $Z \leq 10$, x-ray attenuation is dominated by the Compton scattering for x-rays of 60 keV or higher, i.e. $A_0 \approx A_{KN}$[14]. We call this relationship between phase-shift and attenuation the phase-attenuation duality. The phase-attenuation duality can be used for phase retrieval as follows. Consider a phase contrast imaging setting with a point source of wavelength λ. The object is at a distance R_1 from the source. We denote R_2 as the distance from object to detector plane, $M = (R_1 + R_2)/R_1$ the geometric magnification factor, I_{in} the entrance x-ray intensity at R_1, and $I_D(\vec{r}_D)$ the x-ray intensity at the detector plane. For convenience, we denote $I = M^2 \cdot I_D(\vec{r}_D)/I_{\text{in}}$ as the normalized intensity of phase-contrast image. When the phase-attenuation duality holds, the phase map $\phi(\vec{r})$ can be robustly retrieved from just a single projection image[14]:

$$A_{KN}^2(\mathbf{r}) = \mathfrak{D}(I) = \hat{\mathscr{F}}^{-1}\left(\frac{\hat{\mathscr{F}}(I)}{1+4\pi^2 \tilde{k} \tilde{\mathbf{u}}^2} \right), \qquad \phi(\vec{r}) = \left(\frac{\lambda r_e}{\sigma_{KN}} \right) \ln\left(A_{KN}^2(\vec{r}) \right), \quad (6)$$

where

$$\tilde{k} = \frac{\lambda R_2}{2\pi M} \cdot \frac{\lambda r_e}{\sigma_{KN}}, \quad (7)$$

and $\mathfrak{D}$, for sake of convenience, is called the “duality transform” acting on the normalized image I.

In general imaging cases, such as with low energy x-rays or an object contains calcified tissues such as calcification, this phase-attenuation duality does not hold. However, we can still factor out tissue’s total attenuation A_0 as

$$A_0(\mathbf{r}) = A_{KN}(\mathbf{r}) \cdot A_{pe,coh}(\mathbf{r}), \quad (8)$$

where we denote the attenuation caused by photoelectric absorption and coherent scattering by $A_{pe,coh}$. Strictly speaking, σ_{KN} is only Compton scattering cross-section, it may be slightly different from the incoherent scattering cross-section for high-Z elements. This is because while Compton scattering is x-ray scattering from the free electrons, the incoherent scattering is that from the bound atomic electrons[31]. So when we factor $A_0 = A_{KN} \cdot A_{pe,coh}$ (Eq. (8)) we actually factor the small residual binding effect of atomic electrons into $A_{pe,coh}$. With this understanding, Eqs.(4) and (8) are rigorously valid. The notion of Eq. (6) and Eq. (8) led us to the development of the attenuation-partition based algorithm [1]. While the derivations and the algorithm details of this method can be found from Ref. [1], a brief description of the method is as follows. Our goal is to retrieve the phase map from the two normalized images: one is the object’s attenuation image A_0^2 acquired with $R_2 = 0$, and the other is the acquired phase contrast image $I = M^2 \cdot I_D(\vec{r}_D)/I_{\text{in}}$ with $R_2 > 0$. Employing the acquired phase contrast image I and the duality transform Eq. (6), we will first obtain an estimate for the attenuation-component A_{KN} and phase map ϕ. We then rewrite Eq. (8) as

$$A_0 = A_{\text{KN}} - \delta A, \qquad \delta A = A_{\text{KN}}(1 - A_{\text{pe,coh}}), \tag{9}$$

and find the correction term δA using the estimate of A_{KN}. We then employing the Fresnel Diffraction transform (as defined in Eq. (11)) to transport the wavefield $\delta A e^{i\phi}$ from R_1 to R_2. We can find $\delta I = \left|\mathfrak{F}_{\mathfrak{r}}\left(\delta A e^{i\phi}\right)\right|^2$, which is the difference between phase contrast image I and the "duality-only" counterpart $I_{\text{KN}} = \left|\mathfrak{F}_{\mathfrak{r}}\left(A_{\text{KN}} e^{i\phi}\right)\right|^2$. With the corrected "duality-only" image intensity $I_{\text{KN}} = \left(\sqrt{I} + \sqrt{\delta I}\right)^2$ we can start a new round of iterations by repeating above procedure. For a rigorous analysis of the iterative algorithm and its convergence interesting readers are referred to [1]. Note that the equation $\sqrt{I} = \sqrt{I_{KN}} - \sqrt{\delta I}$ is generally valid, since it is actually a result of x-ray Fresnel diffraction and extremely smallness of hard x-ray wavelength compared to finest resolution achievable in the phase contrast imaging. While interesting readers can find the mathematical proof of this equation in [1], an intuitive explanation of this formula comes from the x-ray propagation. In such a wave propagation process, or the so-called semiclassical wave propagation, the phase of a wave field evolves essentially according to the free-space Hamilton-Jacobi equation from its initial phase value. So if we denote the Fresnel free propagation as a Fresnel transform $\mathfrak{F}_{\mathfrak{r}}$ acting on the initial wavefield, therefore the two resulted wavefields $\mathfrak{F}_{\mathfrak{r}}\left(A_{\text{KN}} \exp[i\phi]\right)$ and $\mathfrak{F}_{\mathfrak{r}}\left(\delta A \exp[i\phi]\right)$ would have the same resultant phases, so the resultant amplitude from the two-wave superposition is given as $\sqrt{I} = \sqrt{I_{KN}} - \sqrt{\delta I}$.

The above iterative procedure can be summarized in flow chart Fig. 1 and the Algorithm

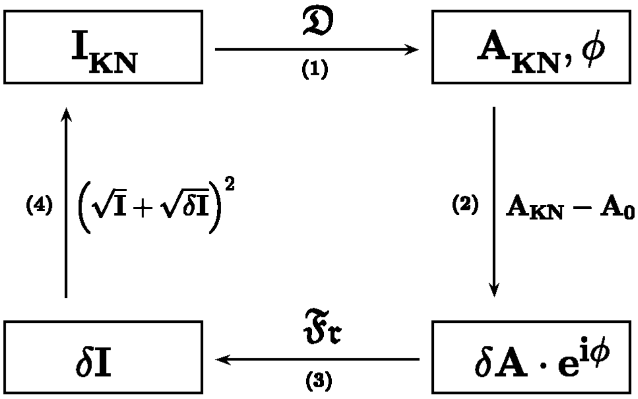
$\mathbf{I_{KN}}$
$\mathfrak{D}$
(1)
$\mathbf{A_{KN}}, \phi$
(2)
$\mathbf{A_{KN} - A_0}$
$\mathfrak{F}_{\mathfrak{r}}$
(3)
$\delta\mathbf{A} \cdot \mathbf{e^{i\phi}}$
$\delta\mathbf{I}$
(4)
$\left(\sqrt{\mathbf{I}} + \sqrt{\delta\mathbf{I}}\right)^2$

Fig. 1. Flow chart of APBA

Algorithm. *In an imaging experiment, assume we have performed two imaging measurements. One image (radiograph) is the attenuation image A_0^2 acquired at SID= R_1, another is a normalized phase-contrast image $I = M^2 \cdot I_D(\vec{r}_D)/I_{\text{in}}$ acquired at SID= $R_1 + R_2$. With A_0^2 and I as well as the initial δI, usually 0, as known inputs, we first assume $I_{\text{KN}} = \left(\sqrt{I} + \sqrt{\delta I}\right)^2$. Then*

(1). *Compute $A_{\text{KN}} = \sqrt{\mathfrak{D}\left(I_{\text{KN}}\right)}$ and ϕ from the duality transform Eq. (6).*

(2). *Compute δA from*

$$\delta A = A_{\mathrm{KN}} \cdot (1-P), \qquad P = A_0 / A_{\mathrm{KN}}. \tag{10}$$

Equations (9) and (10) are in fact the same equations. The advantage of Eq. (10) over (9) is that we can set a threshold for P. We know $P = A_{\mathrm{pe,coh}}$ in the ideal case and $A_{\mathrm{pe,coh}}$ is bounded between 1 and A_0. The computation rounding error or the presence of measured noise in the acquired data can make the value of P over pass these bounds in the iterative computations. By setting a threshold upper bound $\mathrm{ubd} = 1$ *and lower bound* $\mathrm{lbd} = \min(A_0)$*, the minimum value of A_0, to P in the iterative computations, we can make the algorithm more stable. Moreover, if we know a better* lbd *for $A_{\mathrm{pe,coh}}$, other than the minimum of A_0, the converging speed of the algorithm can be greatly improved.*

(3). *Compute δI by Fresnel propagate $\delta A e^{i\phi}$ from position R_1 to R_2: $\delta I = \left|\mathfrak{F}_{\mathfrak{r}}\left(\delta A e^{i\phi}\right)\right|^2$ with*

$$\mathfrak{F}_{\mathfrak{r}}(T)(\vec{r}) = \frac{1}{\lambda R_2} \int_{\mathbb{R}^2} \exp\left[i \frac{\pi M}{\lambda R_2} \left(\frac{\vec{r}}{M} - \vec{\xi} \right)^2 \right] T(\vec{\xi}) d\vec{\xi}. \tag{11}$$

(4). *Compute $I_{\mathrm{KN}} = \left(\sqrt{I} + \sqrt{\delta I}\right)^2$. Go to (1) for next iteration.*

The number of iterations or an accuracy measure can be used to determine when to exit the program: assuming $\|\cdot\|$ is some kind of norm, that can effectively reflect the accuracy of the retrieved data as an image, if $\|\delta I_{k+1} - \delta I_k\|$ is less than a predefined threshold value β, or the iteration step exceeds a predefined maximum number of iteration steps, then ϕ is the retrieved phase and the iteration stops; otherwise further iteration is needed.

An appropriate image accuracy measure should be a measure that can effectively reflect the accuracy of the data AND at the same time correctly reflect the visual perception of the data as an image, since an image's visual perception is crucial for diagnostic radiology. In the next subsection the authors suggest a measure which can be employed as an appropriate image accuracy measure, which was first investigated by Rudin in [32].

2.2. An Image Accuracy Measure

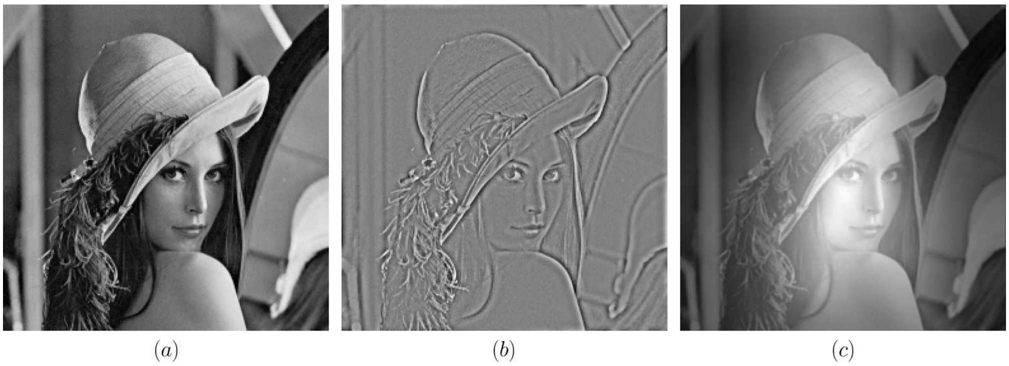
(a) (b) (c)

Fig. 2. Example "Lena" images used in measuring the closeness between images. (a) ϕ_1, (b) ϕ_2, (c) ϕ_3

A continuous signal is generally represented as a function of vector variables: $f(\mathbf{\vec{r}})$. A sampled signal will be represented as a one- (or higher) dimensional sequence of real numbers. In

#126430 - $15.00 USD Received 2 Apr 2010; revised 11 Jun 2010; accepted 9 Jul 2010; published 15 Jul 2010

this paper, we will denote the continuous two dimensional image as an intensity function of two dimensional variables, such as $f(x,y)$, or $f(\vec{\mathbf{r}})$, $\vec{\mathbf{r}}=(x,y)$. The sampled 2-D image will be represented by $f(i,j)$, $i=1,2,\cdots,m$, $j=1,2,\cdots,n$. In practice, to estimate a true signal in noise, the most frequently used methods are based on the least squares criteria and thus an intuitive measure for the closeness of two image functions f and g is, similar to statistical standard deviation, based on:

$$\operatorname{std}(g,f) := \frac{\left[\int_\Omega \left(g(\vec{\mathbf{r}})-f(\vec{\mathbf{r}})-\mu\right)^2 d\vec{\mathbf{r}}\right]^{1/2}}{V(\Omega)}, \tag{12}$$

where Ω is the finite domain of image functions f and g, $V(\Omega)$ represents the area of domain Ω, and $\mu = \int_\Omega (g-f)d\vec{\mathbf{r}}/V(\Omega)$ is the statistical mean value of $g-f$. In [32], L. I. Rudin investigated the relation of edge formation of the 2-D digital image and the singularities of the image function and pointed out that the image intensity function belongs to the space of functions of bounded total variation. Rudin et al.[33] pointed out that the proper norm for images is the total variation (TV) norm, which is the L_1 norm of the gradient of the image function, and not the L_2 norm. For two image functions f and g, we define the TV norm of $g-f$ as the closeness of the two images:

$$\operatorname{TV}(g,f) := \frac{\int_\Omega |\nabla(g-f)|\, d\vec{\mathbf{r}}}{V(\Omega)} = \frac{\int_\Omega \sqrt{\left(\frac{\partial(g-f)}{\partial x}\right)^2 + \left(\frac{\partial(g-f)}{\partial y}\right)^2}\, d\vec{\mathbf{r}}}{V(\Omega)}, \tag{13}$$

where ∇ is the gradient operator. Since std is the form of L_2 norm, it is not suitable as a measure to represent the closeness between two images. For example, for the three "Lena" image functions shown in Fig. 2, the std measures of $\phi_1-\phi_2$ and $\phi_1-\phi_3$ are $\operatorname{std}(\phi_1,\phi_2)=0.206$, $\operatorname{std}(\phi_1,\phi_3)=0.472$ respectively. But the image ϕ_3 is much more closer to ϕ_1 than ϕ_2 does in visual perception. This is because the digital representation of an image depends not only on the pixel values, it also depends on the contrast changes between neighbor pixels. An image's visual perception is crucial for diagnostic radiology. This contrast changes between neighbor pixels can better be represented by the gradient changes of the image functions. For example, the TV measures of $\phi_1-\phi_2$ and $\phi_1-\phi_3$ are $\operatorname{TV}(\phi_1,\phi_2)=0.0247$ and $\operatorname{TV}(\phi_1,\phi_3)=0.0138$ respectively, more appropriate in reflecting the visual perception. In this paper, we will use the TV norm (13) as the measure for closeness between two compared image functions.

Note that the TV norm between two image functions, say g and f, equals 0 if and only if g differs from f by a constant. This feature does not affect its appropriateness for phase retrieval since it is well known that the recovered phase ϕ is unique up to a constant with given information about the attenuation-map A_0 and the phase-contrast intensity-map I.

3. Simulation Tests

In order to investigate the performance of the algorithm constructed above, we perform computer simulations in this section. In Section 3.1, we first construct a breast tissue model that represents the phase-shifts and attenuation of breast tissues and embedded microcalcifications for different x-ray energies. In our simulation tests, the distances of source point to object, R_1, and object to detector, R_2, are set to 26 inches (0.66 m) respectively. In this way the magnification factor $M=(R_1+R_2)/R_1$ is equal to 2. For convenience, the incident x-ray intensity I_{in} at R_1 is set to M^2 (4). We compare the performance of our algorithm, APBA, with two other widely used algorithms: the Gerchberg-Saxton (GS) algorithm (Section 3.2) and the TIE algorithm (Section 3.3).

#126430 - $15.00 USD Received 2 Apr 2010; revised 11 Jun 2010; accepted 9 Jul 2010; published 15 Jul 2010

3.1. A breast specimen model

The tissue's phase-shift and attenuation are determined not only by the tissue's physical composition, but also by the x-ray energy. With different x-ray energy, the same tissue has different phase-shift and attenuation change. Simulation models used in literature often do not incorporate these changes. In this subsection, we construct a breast specimen model that can represent tissue attenuation and phase shifts according to employed x-ray energies as well as tissue's compositions.

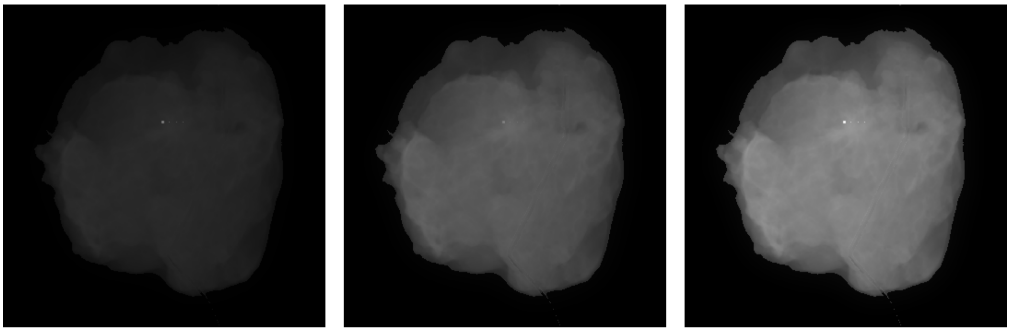

(a) (b) (c)

Fig. 3. Image manifest of (a) $A^2_{\text{pe,coh}}$, (b) A^2_{KN} and (c) A^2_0 when x-ray energy equals 35.5 keV.

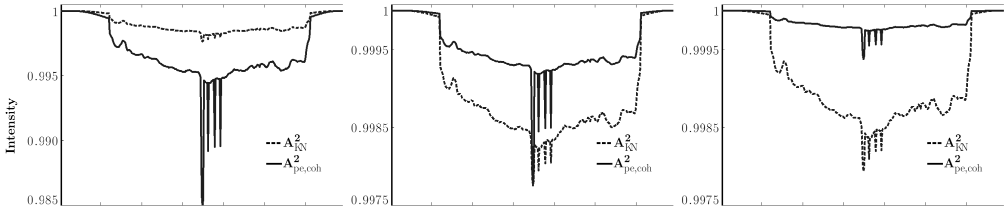

(a) (b) (c)

Fig. 4. Profiles of $A^2_{\text{pe,coh}}$, the solid lines, and A^2_{KN}, the dotted lines, when x-ray energy equals (a) 18.5 keV, (b) 35.5 keV and (c) 59.5 keV.

In our model the tissue has two physical compositions: the 50% glandular-50% adipose breast tissue and the microcalcifications. In order to simulate the morphological aspects of breast tissues, we adopted a radiograph of a breast lumpectomy specimen with pixel values rescaled and the metal localization wire removed by replacing the pixel value at wire position with a mean pixel value at near by positions. It is difficult to remove all the residual trace of the wire this way as can be seen from the following image display especially for the phase contrast image (Fig. 5(c)). In the phase contrast image (Fig. 5(c)), the small residual variation from the original wire-track really got enhanced. The linear attenuation coefficients and electron densities for the 50% glandular-50% adipose breast tissues are computed from the tissue's elemental composition and the interpolated elemental mass attenuation coefficients from the standard reference in the mammographic radiation dosimetry [34, 35]. Moreover, each mass attenuation coefficient is further broken down to two components: one from x-ray photoelectric absorption and coherent scattering, and another from incoherent scattering. In this way, the total attenuation is partitioned as a product of $A^2_{\text{pe,coh}}$ and A^2_{KN} as defined in Eq. (8) above.

In addition, to simulate the microcalcifications in breast, four small ellipsoids of calcium carbonate (CaCO3) are embedded in the specimen model. The diameter of the ellipsoids can be adjusted in simulating different size of the microcalcifications. In the following simulations, to test phase-contrast sensitivity, we set the diameters of the four ellipsoids to 10, 5, 10, and 5 microns in x-ray direction and 300, 200, 300, 200 microns in detector plane respectively.

The attenuation image A_0^2 of the specimen model simulated with 35.5 keV x-ray, and its two corresponding partition images A_{KN}^2 and $A_{\mathrm{pe,coh}}^2$, are shown in Fig. 3. For a comparison, the profiles of A_{KN}^2 and $A_{\mathrm{pe,coh}}^2$ along the line passing through the microcalcifications are shown in Fig. 4 simulated with x-ray energy equals 18.5, 35.5 and 59.5 keV, respectively. We can see that the contribution of $A_{\mathrm{pe,coh}}^2$ to the total attenuation A_0^2 gets smaller when x-ray energy is getting higher. Especially, when x-ray energy equals 59.5 keV, the contribution of $A_{\mathrm{pe,coh}}^2$ for the soft tissue can almost be neglect, as is expected.

3.2. Comparison with the GS Algorithm

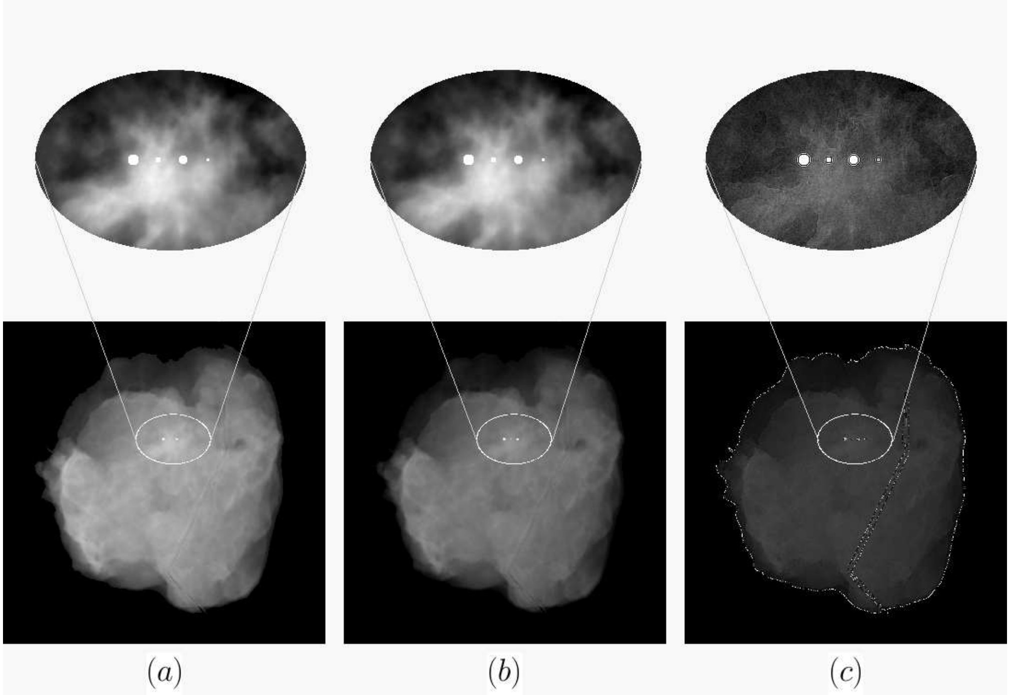

Fig. 5. Image representation of the inputs generated from the simulation model and Fresnel propagation. (a) the phase map ϕ; (b) the attenuation map A_0^2; and (c) the normalized Fresnel propagated phase contrast image I with object to detector distance $R_2 = 26$ in (0.66 m).

The GS algorithm is an iterative algorithm for phase retrievals from a pair of images at two planes related by the Fourier transform. For details readers are referred to [26]. The GS algorithm is a classical algorithm which is widely used in electron microscopy, wave front sensing, astronomy, crystallography, and many other fields involving phase recovery [27, 28, 36].

By replacing the Fourier Transform in the GS algorithm with the Fresnel transform of Eq. (11), we get a modified version of the GS algorithm extended to the *Fresnel diffraction regime*. Our previous simulation tests showed that this modified GS algorithm converges very slow for object-detector distance $R_2 \approx 1\,\mathrm{m}$, and converges faster for larger R_2, such as images acquired at synchrotron beam lines. But this is generally not applicable to the field of clinical imaging, due to the physical constraints such as compact sizes of hospital rooms.

In our simulation tests, we compare the performance of APBA and that of the GS algorithm. The photon energy of the point x-ray source is set to 35.5 keV, and the distances from the source to object and object to detector are set to $R_1 = R_2 = 26$ inches (0.66 m) respectively. For convenience, the incident x-ray intensity I_{in} at R_1 is set to M^2, where $M = (R_1 + R_2)/R_1$ is the magnification factor. The phase map ϕ and the attenuation A_0^2 are generated from our phantom model for 35.5 keV x-ray. Fig. 5 shows the simulated images of the phase map ϕ, the attenuation image A_0^2 and the phase-contrast image I.

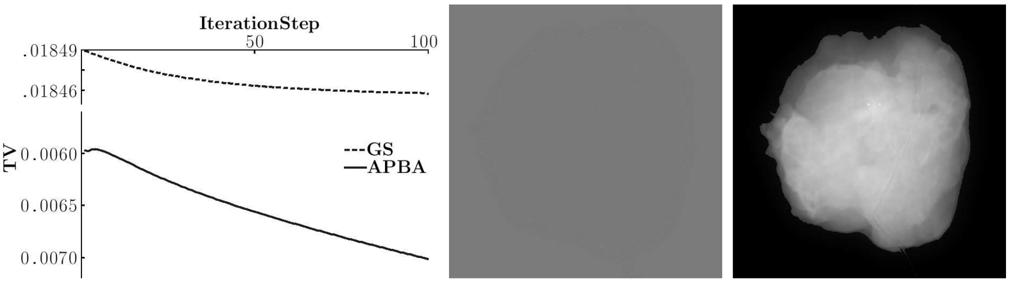

(a) (b) (c)

Fig. 6. Comparison of the performance of the GS algorithm and APBA. (a) plot of the accuracy measures with respect to iteration steps. The plot with solid line represents the APBA. The one with dashed line represents the GS algorithm; (b) recovered phase map with the GS algorithm after 100 iterations; (c) recovered phase map with APBA after 100 iterations.

In the simulation test, the iteration for our attenuation-partition based algorithm (APBA) and the GS algorithm are performed 100 steps. The corresponding recovered phase images are shown in Fig. 6(b) and (c). In Fig. 6(a), the solid line represents the change of total variation (TV) of the retrieved phase using attenuation-partition based algorithm with respect to the iteration steps. The dashed line represents the change of TV of the retrieved phase using the (modified) GS algorithm with respect to iteration steps. We can see that the converging speed of the (modified) GS algorithm is much slower than that of attenuation-partition based algorithm (the change of TV of APBA from step 1 to step 100 is $1.04E-3$, almost 33 times greater than that, $3.17E-5$, of the GS algorithm.) In addition, from the visual perception point of view, we see that the phase map retrieved with the attenuation-partition based algorithm (APBA) is much better than that retrieved with the (modified) GS algorithm.

The main difference between APBA and the GS algorithm is that APBA takes the advantage of the phase-attenuation correlation property, although the extent of this correlation is not known in *priori*, but the GS algorithm does not. From this example we see that the phase-attenuation correlation is a very important information that shouldn't be neglected in the algorithm development for phase retrieval.

3.3. *Comparison with the Transport of Intensity (TIE) algorithm*

We have mentioned the transport of intensity equation in Eq. (3) in Section 1. Since Teague proposed the TIE algorithm for phase retrieval in 1983 [21], numerous phase retrieval algorithms have been suggested on how to effectively search the numerical solution of the TIE [4, 20, 25, 37, 38, 39, 40]. Among the methods of solving the above TIE for the phase map, the one based on Fast Fourier Transform, proposed by Nugent et al. [4], and Allen and Oxley in [25], is the most widely used. In the form of pseudo-differential operator, the solution phase map ϕ is given by

$$\phi(\vec{\mathbf{r}}) = -\frac{2\pi M}{\lambda R_2}\nabla^{-2}\left\{\nabla\cdot\left[\frac{\nabla\left[\nabla^{-2}\left(I-A_0^2\right)\right]}{A_0^2}\right]\right\}, \tag{14}$$

for the given normalized phase-contrast image I and attenuation image A_0^2. Here ∇ is the gradient operator, and ∇^{-2} is the inverse Laplacian operator.

The advantage of this algorithm is that it does not require the boundary information in solving the TIE (assuming the image data is periodic); it is a deterministic method and thus the algorithm is fast and accurate comparing to most iterative algorithms. In this section we compare the performance of the TIE algorithm and that of APBA for two kind of cases: first for the ideal case without any noise and any image misalignment, then for cases simulating practical situation with x-ray imaging noise and possible image misalignment. In these simulation tests, the imaging geometries are the same as in the previous subsection, and x-ray energy is again 35.5 keV .

For the ideal case without any noise and any image misalignment, the performance comparison results are shown in Fig. 7. For the ideal case the TIE algorithm is accurate both in TV measure and visual perception. APBA can also achieves this accuracy but needs 1110 iteration steps to have its TV measure of 0.00215226, an error smaller than that of 0.00215269 with the TIE algorithm.

However, the real test lies in the performance for the cases simulating practical situation with x-ray imaging noise and possible image misalignment. Obviously only the performance in these cases really matters in phase contrast imaging applications, especially for clinical imaging applications where the imposed radiation limits dictates existence of substantial x-ray quantum noise in acquired images. Implemented in the Fourier space, the inverse Laplacian ∇^{-2} in Eq. (14) is singular at zero spatial frequency. This singularity will amplify the noise in the images and result in failure of accurate phase retrieval for the TIE algorithm. To overcome this difficulty, some kind of regularization must be used. The most widely used regularization is Tikhonov regularization, which replaces ∇^{-2} by $|\vec{\mathbf{u}}|^2/(|\vec{\mathbf{u}}|^4+\kappa^2)$, for some "favorable" constant parameter κ, called the Tikhonov regularization parameter. In this regularization scheme, the singularity is regularized, and the favorable parameter κ means the retrieved phase ϕ_κ corresponding this κ is as close to the true phase ϕ as possible. Roughly speaking, the regularization

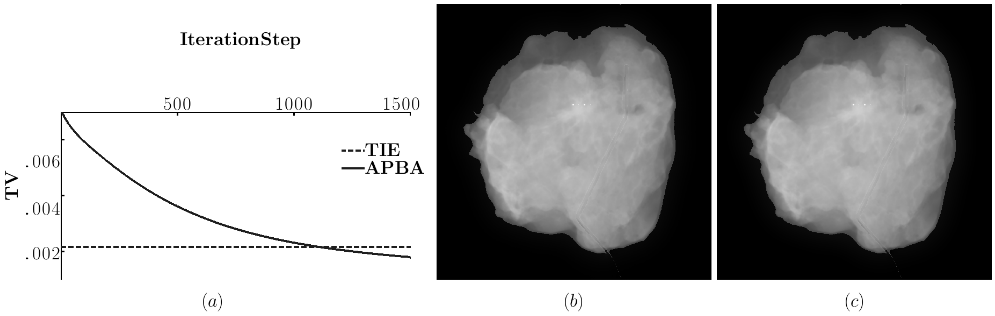

Fig. 7. Comparison of APBA and the TIE algorithm with pure data. (a) plot of the accuracy measure with respect to iteration steps. The plot with solid line represents the APBA. The one with dashed line represents the TIE algorithm. It needs 1110 steps for the TV measure, 0.00215226, of APBA to achieve to the TV measure, 0.00215269, of TIE; (b) recovered phase using the TIE algorithm; (c) recovered phase using APBA after 1500 iteration steps.

#126430 - $15.00 USD Received 2 Apr 2010; revised 11 Jun 2010; accepted 9 Jul 2010; published 15 Jul 2010
(C) 2010 OSA

parameter κ is inversely proportional to the images signal-noise ratio. Two problems, however, arise to this regularization. First, the true phase ϕ is not known in real situations. So the regularization parameter κ is not a priori, which makes it difficult in practical applications. Second, this Tikhonov regularization is based on finding a stable solution to $Ax = y$, in Hilbert spaces X, Y, by solving the minimization problem

$$x_\kappa = \arg\min_{x\in X} \|Ax - y\|_Y^2 + \kappa \|x\|_X^2 . \tag{15}$$

It is L_2 norm dependent. Since the proper norm for image data is the total variation (TV) norm [33], a favorable solution under the Tikhonov regularization principle can not be guaranteed a best solution in visual perception. Moreover, for relatively noisy acquired images, the TIE-based algorithm, even with Tikhonov regularization, often failed to retrieve the phase maps[1].

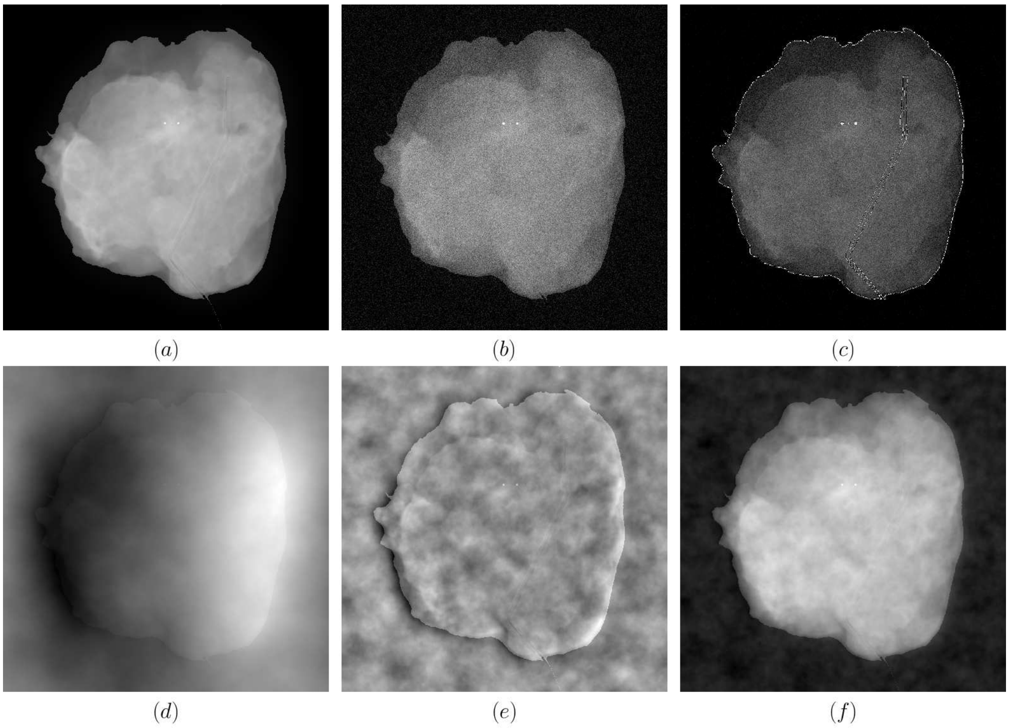

Fig. 8. Comparison of the TIE algorithm and APBA with noise added. (a) True phase map ϕ; (b) attenuation map A_0^2; (c) the normalized phase contrast image I; (d) recovered phase map with the TIE algorithm, no Tikhonov regularization is used; (e) recovered phase map with the TIE algorithm with Tikhonov regularization; (f) recovered phase map with APBA after 10 iteration steps. In the simulation, the acquired data is assumed to have a level of $\delta_b = 0.03\%$ detector noise and one pixel misalignment between A_0^2 and I horizontally.

In the following, we will compare the performance of APBA and the TIE-algorithm when noise is present. In the practice of phase retrieval, there are generally two kinds of image data errors. One is the noise associated with image acquisitions, including the quantum noise of x-ray photon detections and detector electron noise. We assume the quantum noise dominates as is the case in most imaging applications. The other is the error caused by the misalignment between the attenuation map A_0^2 and phase-contrast image I. This is because usually the attenuation image and corresponding phase contrast image are generally acquired in two separate x-ray exposures. The misalignment could be resulted from the shift or tilting of the object or detector between the exposures. In the simulation, we associate each pixel value of an image a photon count N, so that $P(i,j) = c \cdot N(i,j)$, where c is a constant. Assuming the noise has a Poisson distribution, with variance $\sigma^2 = N$ at each pixel. In the simulation we assign a background noise level for each simulated image. This background noise level is defined as the ratio $\delta_b = \sigma_b/N_b$ corresponding to the direct exposure area (where $A^2 = 1$) outside the object in background. The Poisson statistics dictates that $N_b = 1/\delta_b^2$ and in this way the photon count $N(i,j)$ can be determined accordingly at each pixel. Once $N(i,j)$ is determined, the statistical errors at each pixel can be assigned using a computer simulated random Poisson distribution generator with mean corresponding to the photon counts $N(i,j)$. In the simulations below, the background noise level δ_b is set to 0.0003. The images with the noise added are shown in Fig. 8(b) and (c). The quality of an image depends not only on the noise level but also on the extent of image contrast change. With the assumption $P(i,j) = c \cdot N(i,j)$ above, one can easily see that $\delta_b = \sigma_{P_b}/\overline{P_b}$ is the statistical coefficient of variation in absorbed photon numbers in background. $\delta_{oi} = \sigma_{P_{oi}}/\overline{P_{oi}}$, the coefficient of variation of the object image, on the other hand, is the structural coefficient of variation of the sampled image, which reflects the image's normalized extent of image contrast change. We will use the ratio δ_{oi}/δ_b to reflect the image quality. The larger the ratio, the higher the image quality. In our simulation models, when $\delta_b = 0.0003$, the corresponding ratio δ_{oi}/δ_b for attenuation A_0^2 and phase-contrast image I, Fig. 8(b) and (c), are 1.67 and 6.35 respectively. Because of the phase-contrast effect, the image quality of the phase-contrast image I is higher than the attenuation image A_0^2 although they have the same background noise level.

Three simulation tests are performed in the comparison: case1: assume the acquired data A_0^2 and I has noise present but perfectly aligned; case 2: assume acquired data has no noise but has one pixel misalignment horizontally; case 3: assume acquired data has combined detector noise as well as one pixel misalignment. One bias in simulation for the TIE-algorithm should be mentioned: with the known true phase value, a favorable Tikhonov regularization parameter κ can be searched, but in practice this search is hardly feasible. In each case mentioned above, three phase retrievals are performed: 1. using the TIE-algorithm without Tikhonov regularization; 2. using the TIE-algorithm and the favorable Tikhonov regularization parameter; 3. using APBA with 10 step iteration. The Total variation (TV) of the results are listed in Tab. 1 and the recovered phase images for case 3 are shown in Fig. 8(d) – (f). The results using Tikhonov regularization are better than those not using Tikhonov regularization but worse than those using APBA. The influence of misalignment to APBA is little but disaster to the TIE algorithm. From the profile, shown in Fig. 9, along a line passing through the microcalcifications we can see that the values of the phase recovered from APBA is very close to the true phase value, but the values of the phase recovered from the TIE algorithm are distorted.

4. Discussion and Conclusion

Table 1. TV comparison of the TIE algorithm and APBA. In the table, κ is the Tikhonov regularization parameter, Δ represents the sampling step-size in FT-space.

	TV =		
	Case 1	Case 2	Case 3
TIE: no Tikhonov	0.0406	0.0808	0.0886
TIE: with Tikhonov	$\kappa = 0.7828\Delta^2$ 0.0399	$\kappa = 4.4421\Delta^2$ 0.153	$\kappa = 4.1076\Delta^2$ 0.0379
APBA	0.0283	0.0086	0.0290

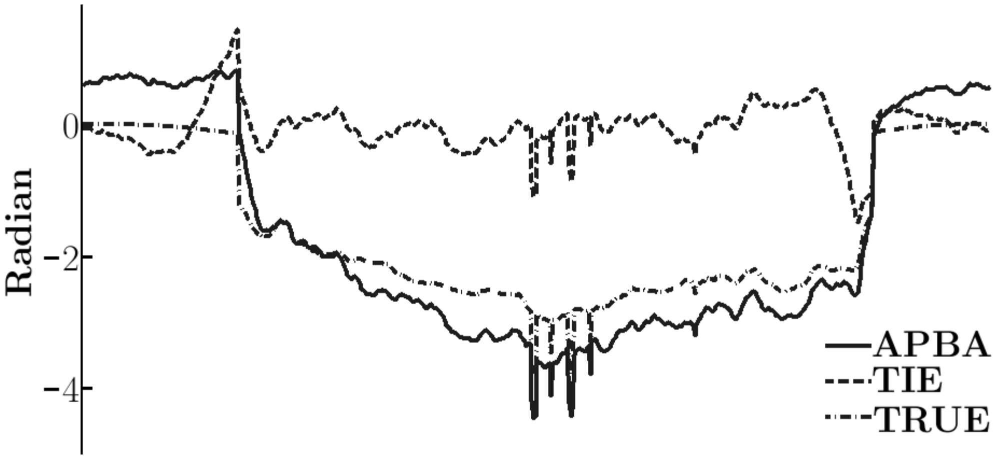

Fig. 9. Profiles, along a line passing through the microcalcifications, of the recovered phase using APBA, the solid line, and using the TIE algorithm with Tikhonov regularization, the dashed line, in Case 3. The dash-dotted line is the true phase.

In above analysis, we assumed that the x-ray source is a quasi-monochromatic point source. In practice, one often employs conventional incoherent and polychromatic sources such as x-ray tubes for imaging. In the experiments with an x-ray tube source, the previous formula Eqs. (2–3) of the phase contrast image intensities should be modified. Since in the APBA method the duality transform is derived based on Eq. (3), hence the Eq. (6) should be modified accordingly. In our previous works we have studied this problem [20]. With the Wigner function based phase space formalism, we have proved that the coherence degree of a finite-size focal spot can be accounted for by the optical transfer function $OTF_{G.U.}(\vec{u}/M)$ for the geometrical unsharpness associated with the finite-size source [20]:

$$OTF_{G.U.}\left(\frac{\vec{u}}{M}\right) = \frac{\int I_{\text{spot}}(\vec{\xi})\exp\left[i2\pi\vec{\xi}\cdot\frac{(M-1)\mathbf{\vec{u}}}{M}\right]d\vec{\xi}}{\int I_{\text{spot}}(\vec{\xi})d(\vec{\xi})}$$

where $I_{\text{spot}}(\vec{\xi})$ is the intensity distribution of the focal spot. We found the generalized TIE equation with an x-ray tube source, that is, the x-ray intensity at the detector is given by [20]:

$$I(\vec{\mathbf{r}};R_1+R_2) = \frac{I_{\text{in}}}{M^2}\hat{\mathscr{F}}^{-1}\left(OTF_{G.U.}\left(\frac{\vec{\mathbf{u}}}{M}\right)\right)\otimes\left\{A^2\left(\frac{\vec{\mathbf{r}}}{M}\right) - \frac{R_2\langle\lambda^2\rangle}{2\pi M\langle\lambda\rangle}\nabla\cdot\left(A^2\nabla\phi\left(\frac{\vec{\mathbf{r}}}{M}\right)\right)\right\},$$

where operator $\otimes$ denotes the convolution, A^2 is the total attenuation of the imaged object, ϕ is the spectrally averaged phase-shift caused by the object, and $\langle\cdot\rangle$ means the spectral average. Compare above equation with Eq. (3) and it is clear that the TIE-based phase retrieval method needs only two modifications: (i). Fourier space de-convolution of the measured intensity from $OTF_{G.U.}(\vec{u}/M)$, (ii). Replacing wavelength with the spectral-averaged $\langle\lambda^2\rangle/\langle\lambda\rangle$. In the same fashion, the duality transform $\mathfrak{D}$ defined in Eq. (6) should be modified with (i). Fourier space de-convolution of the measured intensity from $OTF_{G.U.}(\vec{u}/M)$; (ii). A replacement of the parameter $\tilde{k}$ defined in Eq.(7) with the spectral-average

$$\langle\tilde{k}\rangle = \frac{r_e R_2}{2\pi M}\cdot\left\langle\frac{\lambda^2}{\sigma_{\text{KN}}}\right\rangle.$$

#126430 - $15.00 USD Received 2 Apr 2010; revised 11 Jun 2010; accepted 9 Jul 2010; published 15 Jul 2010
(C) 2010 OSA

Otherwise, the APBA flow chart is the same as that for the case with a quasi-monochromatic point source.

Phase retrieval is a crucial step for quantitative imaging such as reconstructing the 3-D distribution of tissue linear attenuation coefficients and refraction indices. However, images acquired in medical applications are relatively noisy, due to the radiation dose constraints, with low phase contrast effect, due to physical constraints such as compact sizes of hospital rooms. An phase retrieval algorithm which is robust to noise is necessary for potential medical phase contrast imaging. In [1], the authors developed an algorithm, called attenuation-partition based phase retrieval algorithm. It is an iterative algorithm which takes advantage of the correlation between the attenuation and phase-shift. The phase retrieval results from experimental images show that this algorithm is fast and robust [1]. In this work, we systematically compared the performance of this algorithm with other two widely used phase retrieval algorithms, namely the Gerchberg-Saxton (GS) algorithm and the Transport of Intensity Equation (TIE) algorithm. The systematical comparison is conducted by analyzing phase retrieval performances with a digital breast specimen model. We show that the proposed algorithm converges faster than the GS algorithm in the Fresnel diffraction regime, and is more robust against image noise than the TIE algorithm. These results suggest the significance of the proposed algorithm for future medical applications with the x-ray phase contrast imaging technique.

Acknowledgements

This research was supported in part by the Department of Defense Breast Cancer Research Program under award number W81XWH-08-1-0613 and the NIH grant 1R01CA142587.

#126430 - $15.00 USD Received 2 Apr 2010; revised 11 Jun 2010; accepted 9 Jul 2010; published 15 Jul 2010
(C) 2010 OSA

Author's personal copy

Nuclear Instruments and Methods in Physics Research B 269 (2011) 1841–1843

Contents lists available at ScienceDirect

Nuclear Instruments and Methods in Physics Research B

journal homepage: www.elsevier.com/locate/nimb

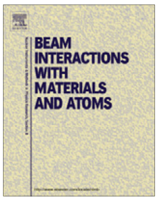

Short Communication

Apparent linear attenuation coefficients in phase contrast X-ray tomography

Aimin Yan, Xizeng Wu *

Department of Radiology, University of Alabama at Birmingham, 619 19th St. South, GSB 301 Birmingham, AL 35249, USA

ARTICLE INFO

Article history:
Received 20 April 2011
Received in revised form 11 May 2011
Available online 20 May 2011

Keywords:
X-ray phase contrast imaging
X-ray tomography

ABSTRACT

In the inline phase contrast X-ray tomography the reconstructed apparent linear attenuation coefficient values may be greatly larger than sample's linear attenuation coefficients or even be negative. In this work we present a general formula to quantitatively relate the apparent linear attenuation coefficient values in cone-beam phase contrast tomography to sample's linear attenuation coefficients and refractive indices. This formula overcomes the gross inaccuracy of the existing formula in the literature in analyzing high-resolution phase contrast tomography, and it will be useful for correctly interpreting and quantifying the apparent linear attenuation coefficients in cone-beam X-ray phase contrast tomography.

© 2011 Elsevier B.V. All rights reserved.

For many applications the X-ray attenuation contrast, such as mass–density differences between different material components, is too small to generate enough image contrast with conventional X-ray tomography. Taking advantage of highly sensitive X-ray phase shifts generated from X-ray coherent scattering, phase contrast X-ray tomography finds broad applications in material science and engineering, biomedical imaging and many other scientific fields [1–3]. In phase contrast X-ray tomography one first makes phase contrast angular projections, in which the refraction and diffraction of phase shifted X-rays form the edge-enhancing interference fringes at interfaces of different material components. From these angular projections 3-D tomograms are then reconstructed using the standard tomography reconstruction methods such as the filtered backprojection methods. The reconstructed phase-sensitive tomograms exhibit enhanced interfaces and layers of different materials and tissues [1–3]. However, these tomograms are not the maps of the linear attenuation coefficients (LACs) of the sample, rather they are the maps of the reconstructed apparent LACs, which may present anomalously large or even negative apparent LAC values at interfaces between different materials and tissues. These "artifacts" may cause faulty interpretation of sample structures, and impede even qualitative characterizations for tissues and materials [1,2,4–6]. As a result, for example, the apparent LAC values of small bronchi were found lower than that of air in phase contrast tomography experiments [2]. In order to correctly interpret and quantify the mixed contrast exhibited in phase contrast tomography, it is necessary to find out quantitative relations between the apparent LAC, on the one hand, and the actual LAC and refractive index, on the other. The previous studies found that the apparent LAC $\mu_{\text{apparent}}(\vec{r}_0)$ in X-ray phase contrast tomography is given by [7–9]:

$$\mu_{\text{apparent}}(\vec{r}_0) = \mu(\vec{r}_0) - \frac{R_2}{M}\cdot\left(\frac{\partial^2}{\partial x_1^2}+\frac{\partial^2}{\partial x_2^2}+\frac{\partial^2}{\partial x_3^2}\right)\Delta_{\text{refr}}(\vec{r}_0). \tag{1}$$

In this equation the first additive term $\mu(\vec{r}_0)$denotes the sample's actual LAC value at position $\vec{r}_0$, and the second additive term is proportional to the three-dimensional Laplacian of the sample's refractive index decrement $\Delta_{\text{refr}}(\vec{r}_0)$ [7–9]. In Eq. (1) R_2 denotes the sample-detector distance and M the magnification factor employed in angular projections. In the literature this second term is used to explain the edge enhancement and the anomalous values of large apparent LAC [7–9].

However, in high-resolution phase contrast tomography with micrometer-scale resolutions the applicability of Eq. (1) is called into question. Researchers recently found that Eq. (1) is invalid in some synchrotron radiation microtomography experiments [10]. In fact, in the derivation of Eq. (1) the phase-sensitive projections were modeled based on the so-called Transport of Intensity Equation (TIE) [7–9]. The TIE describes how the phase-shifted X-rays refract and diffract to form interference fringes at boundaries of material components [11,12]. However, we noted that TIE can only describe the moderate-resolution phase-sensitive projections with $\pi\lambda R_2/(4M\sigma^2) << 1$, where σ denotes the finest size resolved. In cases of high-resolution projections with micrometer-scale resolutions, the fine size resolved could be so small such that $\pi\lambda R_2/4M\sigma^2 \sim 1$ or larger, then TIE becomes inapplicable and Eq. (1) cannot quantify the apparent LAC values observed in high-resolution phase contrast tomography.

To overcome the limitations of Eq. (1), we derived a novel and general formula of apparent LAC values in phase contrast X-ray tomography. Instead of using the TIE, in the derivation we employed the general phase-sensitive projection formula that is

---

* Corresponding author. Tel.: +1 205 975 8135; fax: +1 205 975 4679.
E-mail addresses: ayan@uabmc.edu (A. Yan), xwu@uabmc.edu (X. Wu).

0168-583X/$ - see front matter © 2011 Elsevier B.V. All rights reserved.
doi:10.1016/j.nimb.2011.05.018

Author's personal copy

applicable for high-resolution projections as well [13–14]. We then applied the standard Feldkamp–Davis–Kresss (FDK) cone-beam reconstruction algorithm to the ray-sums of phase-sensitive angular projections [15]. We found that the apparent LAC value $\mu_{\text{apparent}}(\vec{r}_0)$ is given by

$$\mu_{\text{apparent}}(\vec{r}_0) = \cos\left(\frac{\lambda R_2}{4\pi M}\nabla^2_{3D}\right)\mu(\vec{r}_0) - \frac{4\pi}{\lambda} \times \sin\left(\frac{\lambda R_2}{4\pi M}\nabla^2_{3D}\right)\Delta_{\text{refr}}(\vec{r}_0), \tag{2}$$

where the three-dimensional Laplacian operator $\nabla^2_{3D} \equiv (\partial^2/\partial x_1^2 + \partial^2/\partial x_2^2 + \partial^2/\partial x_3^2)$. The operators $\sin\left((\lambda R_2/4\pi M)\nabla^2_{3D}\right)$ and $\cos((\lambda R_2/4\pi M)\nabla^2_{3D})$ in above equation are the pseudo-differential operators. The action of a pseudo-differential operator such as $\sin(c\nabla^2_{3D})$ on a function $g(\vec{r}_0)$ is defined as $\sin(c\nabla^2_{3D})g(\vec{r}_0) \equiv \int\int \exp(i2\pi(\vec{r}-\vec{r}_0)\cdot\vec{f})\cdot\sin\left(-4\pi^2 c\vec{f}^2\right)g(\vec{r})d^3\vec{r}d^3\vec{f}$. Note that Eq. (2) is indeed a generalization of Eq. (1). For experiments with moderate-resolutions or short sample-detector distances such that $\pi\lambda R_2/4M\sigma^2 << 1$, we then have $\cos((\lambda R_2/4\pi M)\nabla^2_{3D}) \approx 1$ and $\sin((\lambda R_2/4\pi M)\nabla^2_{3D}) \approx (\lambda R_2/4\pi M)\nabla^2_{3D}$. Thereby the first term on the RHS of Eq. (2) reduces to the actual LAC, the second term to a scaled Laplacian of $\Delta_{\text{refr}}(\vec{r}_o)$ and Eq. (2) recovers Eq. (1), as is expected.

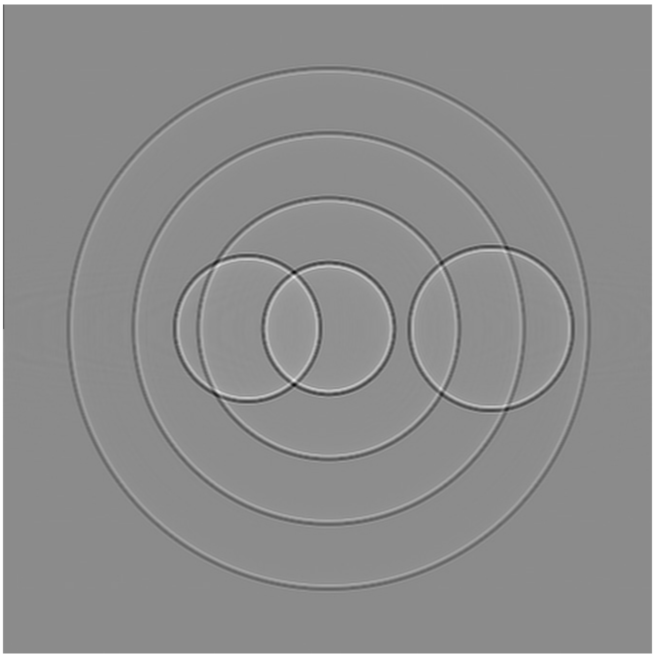

Fig. 1. Reconstructed apparent LAC map of a phantom slice from the phase-sensitive cone-beam tomography with mixed contrast.

In order to validate Eq. (2), we performed numerical simulations. In the simulations the X-ray source was a point source of 60 keV X-rays. The LACs and refractive indices of the numerical phantom were constructed as the sums of the LACs and refractive indices of six spheres of light elements with different radii and center positions. For each sphere the mass densities were designed to decrease radially and diminish rapidly at the sphere's boundary for generating phase contrast. Specifically we set $\mu(\vec{r}_0) = 0.215 \times \sum_{n=1}^{6} f_n(\vec{r}_0)(1/\text{cm})$ and $\Delta_{\text{refr}}(\vec{r}_0) = (7.548 \times 10^{-8}) \times \sum_{n=1}^{6} f_n(\vec{r}_0)$, where $f_n(\vec{r}_0) = \sqrt{R_n^2 - (\vec{r}_0 - \vec{r}_n)^2}/4R_n$ if $|(\vec{r}_0 - \vec{r}_n)| \leqslant R_n$ and $f_n(\vec{r}_0) = 0$ otherwise. Here $\vec{r}_n$ and R_n ($n = 1, 2, \ldots, 6$) denote the center position and radius of the respective sphere. In this way the LACs and refractive indices change continuously without any steps but vary rapidly at the sphere boundaries. Hence strong phase contrast would manifest around the boundaries of the spheres. The detector has 512 × 512 pixels with a sampling pitch of 2 μm. In the simulated scan the source traced a circle orbit, and the source and detector rotated together over an angular range of 360° in 0.5° steps. In order to simulate X-ray Fresnel diffractions involved in the angular projections, one needs to compute X-ray attenuation values and phase shifts of the exit rays in each of the projections. In general one needs to use the multislice propagation method to account for X-ray Fresnel diffractions inside the sample [16]. However, the settings described above satisfy the so-called thin object condition $T < p^2/2\lambda_0$, where T denotes the sample's thickness, p is the resolution and λ_0 the wavelength of 60 keV X-ray [16]. This

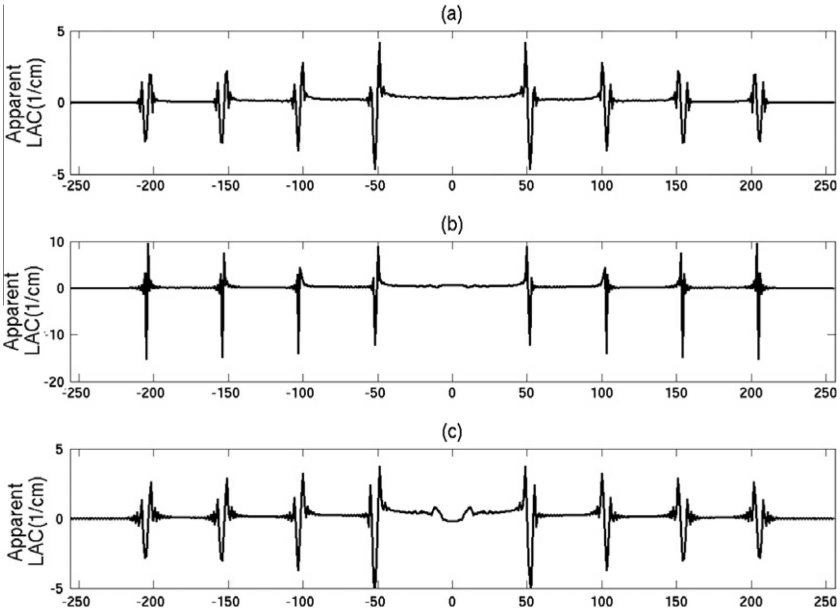

Fig. 2. Profiles of the apparent LACs along the vertical line passing the center of the central sphere. (a) Profile measured from Fig. 1. (b) Profile calculated based on Eq. (1). (c) Profile calculated based on the general formula Eq. (2).

Author's personal copy

Table 1
A comparison of the fringe peak–peak differences in Fig. 2(a)–(c).

	Fringe set 1	Fringe set 2	Fringe set 3	Fringe set 4	Fringe set 5	Fringe set 6	Fringe set 7	Fringe set 8
Peak–peak difference of apparent LACs in Fig. 2(a) (1/cm)	4.648	4.979	6.098	8.860	8.860	6.098	4.979	4.648
Error of calculated peak–peak difference based on Eq. (1) (Fig. 2(b)) (%)	429	346	199	136	136	199	346	429
Error of calculated peak–peak difference based on Eq. (2) (Fig. 2(c)) (%)	15.0	17.5	13.0	6.9	6.9	13.0	17.5	15.0

condition allows us to compute the X-ray attenuation values and phase shifts of the exit X-rays as the ray integrals of the sample's LACs and refractive index decrements. In this simulation a ray-tracing algorithm was used to compute the ray integrals such as $\int \mu dl$ and $\int \Delta_{\text{refr}} dl$ in each of the angular projections. The exit X-ray attenuation and phase shift were determined as $A^2 = \exp\left(-\int \mu dl\right)$ and $\varphi = -(2\pi/\lambda)\int \Delta_{\text{refr}} dl$, respectively [11–14]. Using the exit X-ray attenuation and phase shift from a given projection, we then simulated the free-space Fresnel diffractions of the exit X-rays propagating from the sample to the detector with a setting of $R_2 = 1$ m and $M = 2$ [16]. The Fresnel diffraction intensities in all the angular projections were log-transformed to calculate the ray-sums needed for tomographic image reconstruction. We applied the standard FDK algorithm for image reconstruction [15]. Fig. 1 shows a reconstructed slice of apparent LAC values in gray scale. This slice shows the edge-enhancing dark–bright fringes caused by phase contrast at the interfaces between the spheres. Fig. 2(a) shows the profile of the apparent LAC values along the vertical central line of Fig. 1. The ordinate denotes apparent LAC value in (1/cm) along the vertical line, while the abscissa denotes pixel location along the line. For the sake of comparison Fig. 2(b) and Fig. 2(c) show the profiles of the apparent LAC values along the vertical line, which were computed by using Eq. (1) and Eq. (2) respectively. Note that the ordinate scale in Fig. 2(b) is three times larger than that of Fig. 2(a) and (c). To facilitate the comparisons of the three profiles, we measured the fringe's peak-to-peak differences (the changes between peak and trough) at eight fringe sets for each of the three profiles shown in Fig. 2(a)–(c). Table 1 lists the measured fringe peak-to-peak differences of apparent LACs in Fig. 2(a), which is obtained from Fig. 1, the phantom's phase contrast tomogram simulated by using the Fresnel diffraction and FDK-reconstruction. Compared to these eight peak-to-peak differences in Fig. 2(a), the table lists as well the errors of the calculated peak–peak differences based on Eq. (1) (Fig. 2(b)) and Eq. (2) (Fig. 2(c)) respectively. From these comparisons, it is clear that the apparent LAC values calculated from Eq. (1) are grossly inaccurate with the errors amounting to several hundred percent, while the apparent LAC values calculated by means of Eq. (2) achieve reasonable quantitative accuracies as is shown in Table 1. In addition, the profile Fig. 2(c) shows two small bumps at the center of the profile. We found that these variations of apparent LACs are artifacts caused by omitting the small nonlinear terms in phase shifts in the derivation of Eq. (2). The omission of these nonlinear terms mainly affects the accuracies in computing the side-lobes of phase contrast fringes, thereby causes these two small bumps, which are associated with the distorted fringe side-lobes near the right boundary of the left off-center sphere in the phantom (Fig. 1).

In summary, we present a general formula (Eq. (2)) to quantitatively relate the apparent LAC values in cone-beam phase contrast tomography to sample's LAC and refractive index values. This formula overcomes the gross inaccuracy of the existing formula in the literature in analyzing high-resolution phase contrast tomography. We believe that this general formula will be useful for designing phase contrast tomography experiments, and for correctly interpreting and quantifying the apparent LAC values in cone-beam X-ray phase contrast tomography. For example, Eq. (2) can be used for computing the edge-enhancement profiles for analyzing presampling modulation transfer functions in synchrotron radiation microtomography [10].

Acknowledgment

This research was supported in part by the NIH Grant R01CA142587 and the DoD Breast Cancer Research Program award W81XWH-08-1-0613.

References

[1] S.R. Stock, Recent advances in X-ray microtomography applied to materials, Int. Mater. Rev. 53 (2008) 129–181.

[2] T. Sera, K. Uesugi, N. Yagi, Refraction-enhanced tomography of mouse and rabbit lungs, Med. Phys. 32 (2005) 2787–2792.

[3] W. Zhu, G. Gaetani, F. Fusseis, L. Montési, F. De Carlo, Microtomography of partially molten rocks: three-dimensional melt distribution in mantle peridotite, Science 332 (2011) 88–91.

[4] S. Mayo, T. Davis, T. Gureyev, P. Miller, D. Paganin, A. Pogany, A. Stevenson, S. Wilkins, X-ray phase-contrast microscopy and microtomography, Opt. Express 11 (2003) 2289–2302.

[5] E. Donnelly, R. Price, K. Lewis, D. Pickens, Polychromatic phase-contrast computed tomography, Med. Phys. 34 (2007) 3165–3168.

[6] Y. De Witte, M. Boone, J. Vlassenbroeck, M. Dierick, L. Van Hoorebeke, Bronnikov-aided correction for X-ray computed tomography, J. Opt. Soc. Am. A26 (2009) 890–894.

[7] P. Cloetens, M. Pateyron-Salome, J. Buffiere, G. Peix, J. Baruchel, F. Peyrin, M. Schlenker, Observation of microstructure and damage in materials by phase sensitive radiography and tomography, J. Appl. Phys. 81 (1997) 5878–5886.

[8] X. Wu, H. Liu, A. Yan, Phase-contrast X-ray tomography: contrast mechanism and roles of phase retrieval, Eur. J. Radiol. 68 (2008) S8–S12.

[9] W. Cai, R. Ning, Preliminary study of a phase-contrast cone-beam computed tomography system: the edge-enhancement effect in the tomographic reconstruction of in-line holographic images, Opt. Eng. 47 (2008) 1–12. 037004.

[10] R. Mizutani, K. Taguchi, A. Takeuchi, K. Uesugi, Y. Suzuki, Estimation of presampling modulation transfer function in synchrotron radiation microtomography, Nucl. Instrum. Meth. A 621 (2010) 615–619.

[11] M. Teague, Deterministic phase retrieval: a Green's function solution, J. Opt. Soc. Am. 73 (1983) 1434–1441.

[12] K. Nugent, T. Gureyev, D. Cookson, D. Paganin, Z. Barnea, Quantitative phase imaging using hard X-rays, Phys. Rev. Lett. 77 (1996) 2961–2965.

[13] X. Wu, H. Liu, A general theoretical formalism for X-ray phase contrast imaging, J. X-Ray Sci. Technol. 11 (2003) 33–42.

[14] J. Guigay, M. Langer, R. Boistel, P. Cloetens, Mixed transfer function and transport of intensity approach for phase retrieval in the Fresnel region, Opt. Lett. 32 (2007) 1617–1619.

[15] L. Feldkamp, C. Davis, J. Kress, Practical cone-beam algorithm, J. Opt. Soc. Am. A1 (1984) 612–619.

[16] J. Cowley, Diffraction Physics, 3rd ed., North-Holland, Amsterdam, 1995.

Robustness of phase retrieval methods in x-ray phase contrast imaging: A comparison

Aimin Yan and Xizeng Wu[a)]
Department of Radiology, University of Alabama at Birmingham, Birmingham, Alabama 35233

Hong Liu
Center for Bioengineering and School of Electrical and Computer Engineering, University of Oklahoma, Norman, Oklahoma 73019

(Received 31 May 2011; revised 4 July 2011; accepted for publication 8 July 2011; published 17 August 2011)

Purpose: The robustness of the phase retrieval methods is of critical importance for limiting and reducing radiation doses involved in x-ray phase contrast imaging. This work is to compare the robustness of two phase retrieval methods by analyzing the phase maps retrieved from the experimental images of a phantom.

Methods: Two phase retrieval methods were compared. One method is based on the transport of intensity equation (TIE) for phase contrast projections, and the TIE-based method is the most commonly used method for phase retrieval in the literature. The other is the recently developed attenuation-partition based (AP-based) phase retrieval method. The authors applied these two methods to experimental projection images of an air-bubble wrap phantom for retrieving the phase map of the bubble wrap. The retrieved phase maps obtained by using the two methods are compared.

Results: In the wrap's phase map retrieved by using the TIE-based method, no bubble is recognizable, hence, this method failed completely for phase retrieval from these bubble wrap images. Even with the help of the Tikhonov regularization, the bubbles are still hardly visible and buried in the cluttered background in the retrieved phase map. The retrieved phase values with this method are grossly erroneous. In contrast, in the wrap's phase map retrieved by using the AP-based method, the bubbles are clearly recovered. The retrieved phase values with the AP-based method are reasonably close to the estimate based on the thickness-based measurement. The authors traced these stark performance differences of the two methods to their different techniques employed to deal with the singularity problem involved in the phase retrievals.

Conclusions: This comparison shows that the conventional TIE-based phase retrieval method, regardless if Tikhonov regularization is used or not, is unstable against the noise in the wrap's projection images, while the AP-based phase retrieval method is shown in these experiments to be superior to the TIE-based method for the robustness in performing the phase retrieval. © *2011 American Association of Physicists in Medicine*. [DOI: 10.1118/1.3618731]

Key words: x-ray imaging, phase contrast, phase retrieval

I. INTRODUCTION

In recent years, the in-line phase-contrast x-ray imaging has attracted intensive research efforts. The in-line phase-contrast x-ray imaging is a technique using the free space diffraction of phase-shifted x-rays to form the interference fringes at tissues' boundaries and interfaces in images.[1–8] In fact, for over 100 years, the tissue attenuation differences have been the sole contrast mechanism for medical x-ray imaging. However, when x-rays traverse the body parts, as a wave x-rays undergo phase shifts as well. The amount of the phase shift along an exit ray is determined by the tissue refractive indices along the ray. Note that x-ray refractive index n is a complex number and equal to $n = 1 - \delta + i\beta$, where δ is the refractive index decrement and responsible for x-ray phase shift, while β is the imaginary part of the refractive index and responsible for x-ray attenuation. The amount of x-ray phase shift along an exit ray is given by $\varphi = -(2\pi/\lambda)\int \delta ds$, where λ is the x-ray wavelength, and the integral is over the ray path.[1,2] In other words, the phase shift is equal to the projection of refractive index decrements scaled by a factor $(2\pi/\lambda)$. On the other hand, x-ray attenuation along an exit ray is determined by the projection of the tissue linear attenuation coefficients along the ray, which is equal to $(4\pi/\lambda)\int \beta ds$.[1,2] We have estimated δ and β values for the biological tissues and found that the tissue δ values (10^{-6}–10^{-8}) are about 1000 times greater than their β values (10^{-9}–10^{-11}) for 10–150 keV x-rays.[8] Hence, the differences in x-ray phase shifts between different tissues are about 1000 times greater than their differences in the projected linear attenuation coefficients. Therefore, the phase-contrast imaging techniques may greatly increase the lesion-detection sensitivity for x-ray imaging. The settings for the inline phase-sensitive imaging are similar to that of conventional x-ray imaging, provided a source with very small focal spot and a sufficiently large object-detector distance are required.[5,7,8] In the inline imaging setting, x-rays undergo phase shifts as traversing the imaged object, and then diffract freely over a sufficiently large distance before reaching the detector. In this way, the tissues' phase contrast manifests as the dark-bright diffraction fringes at tissues' boundaries and interfaces in the measured images.[5,7,8] Hence, the inline phase contrast imaging has good potential of greatly enhancing the detection sensitivity and reducing radiation doses involved in the imaging.

However, as the interfaces and boundaries of the different tissue compartments are greatly accentuated in a phase-contrast image, the bulk phase contrast in a given tissue compartment, where the phase shifts may vary slowly, could get lost. This is because the phase contrast is proportional to the Laplacian and gradient differentials of the phase shifts, as is shown in Sec. II below. Moreover, the information about x-ray phase shifts are valuable for tissue characterizations, since x-ray phase shift along a ray is proportional to the projected tissue electron density, that is, $\varphi = -\lambda r_e \int \rho_e ds$, where r_e is the classic electron radius and ρ_e denotes the tissue electron density and the integral is over the ray path.[1,2] In order to fully exhibit tissue phase contrast and reconstruct tissue projected electron densities for quantitative tissue characterizations, one needs to extract the tissue phase shifts from the mixed contrast exhibited in a phase-sensitive projection. The procedure of retrieving the phase-shift map of an object from its phase-sensitive projections is called the phase retrieval.[10–14] A retrieved phase map is able to provide a quantitative map of the object's projected electron densities, which could be used for quantitative tissue characterizations.[12–14] Moreover, performing phase retrieval is necessary for reconstructing volumetric 3-D maps of tissue attenuation coefficients and refractive indices, respectively,[14,15] and for eliminating the phase-contrast caused artifacts in the volumetric 3-D images.[16]

Examining the robustness of phase retrieval methods against the projection noise, such as the x-ray photon quantum noise and others involved in the projection acquisitions, is an important task in phase contrast imaging. If a phase retrieval method is not robust against the noise, the method could become unstable and fail in phase retrievals if the acquired projection images had be contaminated with substantial noise. On the other hand, suppressing x-ray quantum noise may require using high radiation doses in the image acquisitions. For clinical applications, it is imperative to limit and reduce radiation doses involved, hence, it is critical to develop robust phase retrieval methods for future clinical applications of phase contrast imaging. The purpose of this work is to compare the robustness of two phase retrieval methods by means of analyzing the phase maps retrieved from the experimental projection images of an air-bubble wrap phantom. We will first introduce the phase retrieval method that is based on the transport of intensity equation (TIE), which describes how the phase contrast is encoded in the projection images.[10,11] This TIE-based method is the most commonly used method for phase retrieval in the literature. We will then introduce a recently developed phase retrieval method, namely the attenuation-partition based (AP-based) method.[13] In order to examine the robustness of these two methods against noises, we applied these two phase retrieval methods to experimental phantom images, namely a radiograph and a phase contrast image of the air-bubble wrap phantom, for the phase retrievals. We will analyze the retrieved phase maps obtained by using the two methods and compare their performances in the robustness against noises in the phantom images. In Sec. IV, we explain that these performance differences of the two phase retrieval methods are rooted in their different techniques employed to deal with the singularity problem involved in the phase retrievals. In addition, other factors that may affect the phase retrieval performance will be briefly discussed as well.

II. PHASE RETRIEVAL METHODS

In phase contrast images, the attenuation contrast and phase contrast are mixed together. In order to retrieve phase maps from phase contrast projection images, one should understand how the phase contrast is encoded in the projection images. This understanding can be gained from the x-ray propagation equation such as the TIE.[10,11] This equation can be derived either from the x-ray Fresnel-diffraction equation or the Wigner distribution based phase-space formalism.[9–11] If we denote the x-ray transmission image of an object, or equivalently its x-ray attenuation map by $A_o^2(\vec{r})$ and the x-ray phase-shift map of the object by $\varphi(\vec{r})$, then the detected x-ray intensities are given by[8,11,17]

$$I(\vec{r}_D) = \frac{I_{in}}{M^2}\left\{A_o^2(\vec{r}_D/M) - \frac{R_2\bar{\lambda}}{2\pi M}\nabla\cdot\left(A_o^2(\vec{r}_D/M)\nabla_{\varphi}(\vec{r}_D/M)\right)\right\} \tag{1}$$

where $\bar{\lambda}$ is the average x-ray wavelength of the polychromatic x-rays. In Eq. (1), I_{in} is the entrance x-ray intensity, R_1 is the source-object distance set in the projection, R_2 is the object-detector distance, $M = (R_1 + R_2)/R_1$, the magnification factor in the projection, and $\vec{r}_D$ denotes the position vector in the detector plane. In Eq. (1), the operator ∇ denotes the two-dimensional transverse gradient differential operator. For the purpose of this work, we assume that the x-ray source's focus spot is ideally point-like and the detector employed is an ideal detector. Obviously, the detected x-ray intensity $I(\vec{r}_D)$ is determined not only by attenuation map $A_o^2(\vec{r})$ in the projection, but also by the encoded phase contrast, that is, by the transverse Laplacian and gradient differentials of the phase-shift map $\varphi(\vec{r})$ in the projection. Since the phase contrast and attenuation contrast are mixed together in a phase contrast image, as is shown by Eq. (1), hence measuring a single phase-contrast image is not enough for retrieving the phase-shift map $\varphi(\vec{r})$ in the projection. Therefore, in general, at least two projection images are needed for retrieving the phase-shift map $\varphi(\vec{r})$ of the object.

The most commonly used phase retrieval method in the literature is the TIE-based method. In this method, two acquired projection images of an object are used for retrieving the phase-shift map of the object: one is a contact radiograph $A_o^2(\vec{r})$ of the object, the other is a phase contrast projection image $I(\vec{r}_D)$ of the object. One then is able to retrieve the phase-shift map $\varphi(\vec{r})$ by solving Eq. (1) for $\varphi(\vec{r})$ as follows[12]:

$$\varphi(\vec{r}) = -\left(2\pi M/\bar{\lambda}R_2\right)\nabla^{-2} \times \left\{\nabla\cdot\left[\frac{1}{A_o^2}\nabla\left(\nabla^{-2}\left(\frac{M^2 I}{I_{in}} - A_o^2\right)\right)\right]\right\}. \quad (2)$$

In above equation, the operator ∇^{-2} denotes the inverse of the Laplacian differential operator $\nabla^2 \equiv (\partial^2/\partial x^2 + \partial^2/\partial y^2)$. The inverse Laplacian operator ∇^{-2} is a pseudodifferential operator. The action on a function $g(\vec{r})$ of a pseudodifferential operator such as ∇^{-2} is defined as

$$\nabla^{-2}g(\vec{r}) \equiv \iint \exp(i2\pi(\vec{s}-\vec{r})\cdot\vec{f})\cdot\left(-1/\left(4\pi^2\vec{f}^2\right)\right) \times g(\vec{s})d^2\vec{s}\cdot d^2\vec{f}. \quad (3)$$

In Eq. (3), $\vec{s}$ and $\vec{f}$ denote the integral variables in the coordinate space and frequency space, respectively. Hence, one can compute the phase map $\varphi(\vec{r})$ by using Eq. (2) with the help of Eq. (3). The TIE-based method is effective and fast for phase retrievals in the cases with strong phase contrast effects and low noise levels as is shown in many cases discussed in the literature.[11,12] However, the Achilles heel of the TIE-based method lies at the inverse Laplacian operator ∇^{-2} involved in Eq. (2). The operator ∇^{-2} adds a zero-frequency singularity to Eq. (2), as is suggested by Eq. (3). As we will see below, the singularity may amplify the noise randomly embedded in the acquired images and result in instability in phase retrievals.

In order to get rid of the singular pseudodifferential operator ∇^{-2} involved in the TIE-based phase retrievals, we recently developed a novel phase retrieval method: the AP based method or the AP-based method for short.[13,18] Our idea in this method is to utilize the correlation between the x-ray phase shift and its attenuation to eliminate any singularity involved in the phase retrievals. As is well known, in the diagnostic x-ray imaging, x-ray attenuation A_o^2 arises from three x-ray-matter interactions: the photoelectric absorption, the coherent scattering, and the incoherent scattering. Correspondingly, we can partition the x-ray attenuation into two parts: the Compton scattering-caused attenuation A_{KN}^2 and the attenuation caused by photoelectric absorption and coherent scattering, which is denoted by $A_{pe,coh}^2(\vec{r})$. That is, we can partition the overall x-ray attenuation A_o^2 into a product of two parts

$$A_o^2(\vec{r}) = A_{KN}^2(\vec{r})\cdot A_{pe,coh}^2(\vec{r}). \quad (4)$$

The reason of factoring out A_{KN}^2 is that both of A_{KN}^2 and the phase-shift φ are determined by the tissue's electron density

$$A_{KN}(\vec{r}) = \exp\left[-\frac{\bar{\sigma}_{KN}}{2}\rho_{e,p}(\vec{r})\right], \quad \varphi(\vec{r}) = -\bar{\lambda}r_e\rho_{e,p}(\vec{r}) \quad (5)$$

where $r_e = 2.818\times10^{-15}$ m is the classical electron radius, $\rho_{e,p}$, the projected electron density along the ray path, that is, $\rho_{e,p}(\vec{r}) = \int_{ray}\rho_e(\vec{r},z)dz$, and $\bar{\sigma}_{KN}$ denotes the average Compton scattering cross-section for polychromatic x-rays. Note that Compton scattering cross-section is given by the Klein-Nishina total cross-section[19]

$$\sigma_{KN}(E) = 2\pi r_e^2\left\{\frac{1+\eta}{\eta^2}\left[\frac{2(1+\eta)}{1+2\eta} - \frac{1}{\eta}\log(1+2\eta)\right] + \frac{1}{2\eta}\log(1+2\eta) - \frac{1+3\eta}{(1+2\eta)^2}\right\}, \quad (6)$$

where $\eta \equiv E\ /511$ keV and it slowly varies with x-ray energy E for $E \ll 511$ keV. We observed that the extent of the correlation between phase and attenuation depends on the x-ray photon energies and the tissues elemental compositions. For example, for light elements with atomic numbers $Z < 10$ and x-rays of 60 keV or higher, the x-ray-matter interactions are dominated by the Compton scattering, hence, both the tissue attenuation and phase shift are all determined by tissues' electron density distributions. We call this relationship between phase shift and attenuation the phase-attenuation duality, and we define the so-called duality transform as[20]

$$\mathfrak{D}(I(\vec{r}_D)) \equiv \left(1 - \left(\bar{\lambda}^2R_2r_e/2\pi M\bar{\sigma}_{KN}\right)\nabla^2\right)^{-1}\cdot\left(\frac{M^2I(\vec{r}_D)}{I_{IN}}\right). \quad (7)$$

For the cases where the x-ray-matter interactions are dominated by the Compton scattering, we proved that the attenuation A_{KN}^2 can be found from a single phase contrast image $I(\vec{r}_D)$ by means of the duality transform such that $A_{KN}^2(\vec{r}) = \mathfrak{D}(I(\vec{r}_D))$.[20] With the help of the phase-attenuation duality, the phase-shift map of the object can be simply retrieved as

$$\varphi(\vec{r}) = \frac{\bar{\lambda}r_e}{\bar{\sigma}_{KN}}\ln A_{KN}^2(\vec{r}) = \frac{\bar{\lambda}r_e}{\bar{\sigma}_{KN}}\ln\mathfrak{D}(I(\vec{r}_D)). \quad (8)$$

We call this formula as the phase-attenuation duality-based phase retrieval formula.[20] One significant advantage of this duality-based phase retrieval formula is that the pseudodifferential operator $\left(1 - \left(\bar{\lambda}^2R_2r_e/2\pi M\bar{\sigma}_{KN}\right)\nabla^2\right)^{-1}$ involved in Eqs. (7) and (8) is free of any singularity. Therefore, the phase retrieval method based on the phase-attenuation duality is stable and robust against the noise in images.[20]

Unfortunately, the phase-attenuation duality does not hold in some other cases such as imaging with low energy x-rays or imaging bones and calcifications that contain substantial amount of heavy elements. In those cases, the retrieved phase map using Eq. (8) may provide merely coarse estimates of the real phase maps of the imaged objects. In order to overcome this limitation of the duality-based phase retrieval formula Eq. (8), recently we proposed to correct the errors iteratively through repeated comparisons of the computed estimates of the x-ray Fresnel-diffraction intensities against the acquired projection intensities. To implement this strategy, we developed the attenuation-partition based iterative algorithm, whose flow chart is shown in Fig. 1.[13] While interested readers can find the mathematical proofs of the algorithm in Ref. 13, here, we give a brief explanation of this algorithm flow chart in Fig. 1. In this flow chart, A_o^2 denotes the attenuation map of the imaged object measured from its contact radiograph and I is the acquired phase contrast image of the object. In the flow chart, I_{KN} denotes the simulated phase contrast image formed

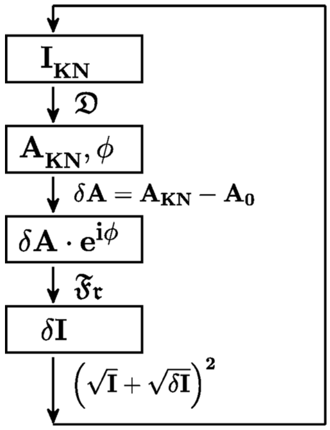
$\mathbf{I_{KN}}$
$\mathfrak{D}$
$\mathbf{A_{KN}}, \phi$
$\delta\mathbf{A} = \mathbf{A_{KN}} - \mathbf{A_0}$
$\delta\mathbf{A} \cdot \mathbf{e}^{\mathbf{i}\phi}$
$\mathfrak{F}_{\mathfrak{r}}$
$\delta\mathbf{I}$
$\left(\sqrt{\mathbf{I}} + \sqrt{\delta\mathbf{I}}\right)^2$

FIG. 1. Flow chart of the AP based iterative algorithm.

by using the estimated object's electron densities and by turning off the attenuation processes associated with x-ray photoelectric absorption and coherent scattering. In Fig. 1, two transforms are implemented in the iterations, one is the Fresnel-diffraction transform $\mathfrak{F}_{\mathrm{re}}$, which implements x-ray Fresnel-diffraction,[21] and the other is the duality transform $\mathfrak{D}$ as is defined in Eq. (7). According to this flow chart (Fig. 1) of the AP-based phase retrieval method, one first applies the duality transform $\mathfrak{D}$ to the acquired phase contrast image I to obtain an estimate of A_{KN}^2 and the phase map φ of the object. One then compares A_{KN}^2 against the measured A_o^2 and computes the error $\delta A \equiv A_{KN} - A_0$. Applying the Fresnel-diffraction transform $\mathfrak{F}_{\mathrm{re}}$ to the fictitious transmission function $\delta A \cdot \exp(i\varphi)$, one computes the I_{KN} -correction $\delta I \equiv \left|\mathfrak{F}_{\mathrm{re}}(\delta A \cdot \exp(i\varphi))\right|^2$, and a new estimate of I_{KN} is determined as $I_{KN} = (\sqrt{I} + \sqrt{\delta I})^2$. With this new estimate of I_{KN}, one can start a new round of the iteration as is indicated in the flow chart Fig. 1. The iteration converges when the I_{KN} does not change substantially with further iteration steps.[13]

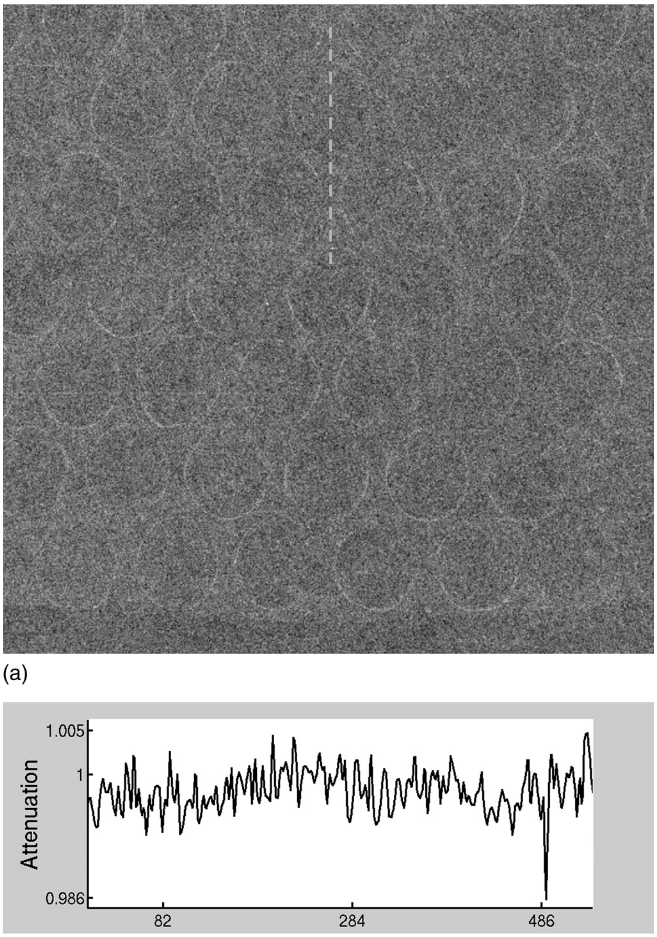

(a)

(b)

FIG. 2. (a) Contact radiograph of the bubble wrap acquired at 40 kVp and with a SID = 1.75 m. (b) Intensity profile along the marked line on (a).

III. COMPARISON OF THE TWO PHASE RETRIEVAL METHODS

In order to compare the robustness of above two phase retrieval methods, namely, the TIE-based method and the AP-based method, we applied the two methods for retrieving the phase map of a piece of air-bubble wrap. In the bubble wrap, the air packets are locked between two thin layers of low-density polyethylene films forming the air bubbles. Shown in Fig. 2(a) is a contact radiograph of the wrap. The x-ray source used was a micro-focus x-ray tube (L8121-02, Hamamatsu) with a focal spot size of 7 μm. The source has a tungsten target without added filtration and was operating at 40 kVp and 0.2 mA for a 30 s exposure. The average x-ray photon energy was estimated at 14.6 keV for the 40 kVp x-rays. In this acquisition, the source-detector distance (SID) was set to 1.78 m. The imaging detector employed was an aSe-based flat-panel detector (DirectRay, Hologic) with a pixel pitch of 140 μm. Since the thin polyethylene films and locked air bubbles in the wrap generate little differences in x-ray attenuation, hence, the wrap's radiograph in Fig. 2(a) exhibits only little image contrast, and the x-ray quantum noise in the acquisition masked the wrap's details such that the rims of many bubbles are not visible on the image. Figure 2(b) shows a profile of image intensities along the marked dash line on Fig. 2(a) and the profile reveals how the noisy intensity variations mask the low contrast rims of the bubbles. In contrast, Fig. 3(a) is a phase contrast image of the bubble wrap. This phase contrast image was acquired with a sample-detector distance $R_2 = 1.15\,\mathrm{m}$ and otherwise the same technique settings as that used for the radiograph, that is, with the same focal spot size, same tube voltage, same tube current and exposure time, same SID, and the same detector. However, in this projection, the phase-shifted x-rays were allowed to freely diffract over 1.15-m long distance on their way to the detector and to form the interference fringes at the bubble boundaries on the image. As is shown in Fig. 3(a), the phase contrast depicts not only the bubble rims, but also the dents inside the bubble domes. The enhancement is resulted from the rapid changes of the projected thicknesses of the polyethylene films at the bubble rims and the dents inside bubble domes. These rapid changes in the projected thicknesses of polyethylene generate as well rapid changes in x-ray phase shifts, since the x-ray phase shifts are given by $\varphi(\vec{r}) = -\lambda r_e \rho_e T_p(\vec{r})$, where ρ_e denotes polyethylene film's electron density and $T_p(\vec{r})$ denotes projected thickness of polyethylene along the ray. According to

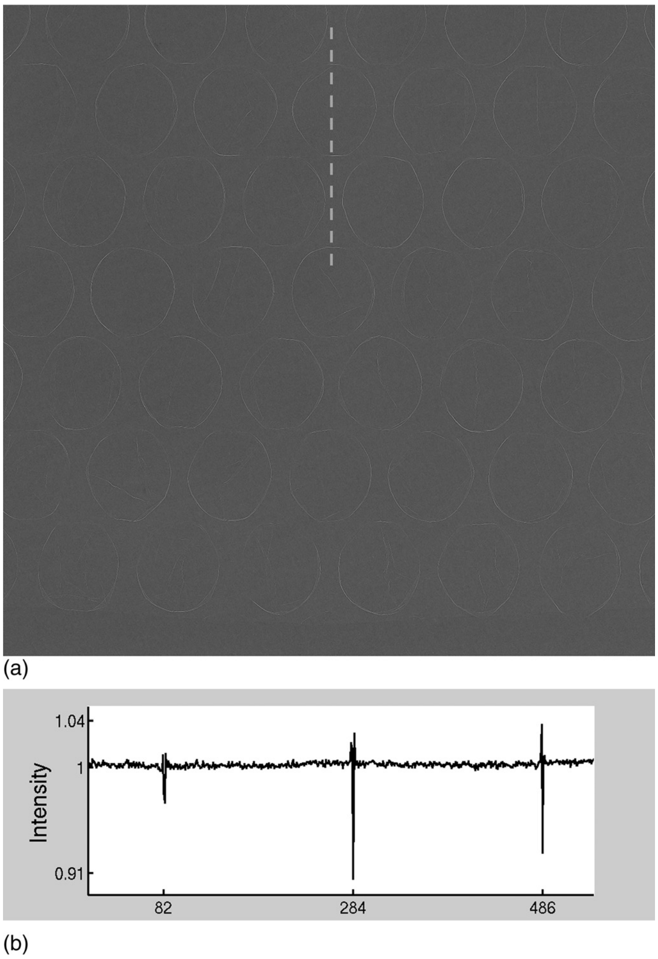

FIG. 3. (a) Phase contrast image of the bubble wrap, which was acquired at 40 kVp and with a SID = 1.75 m and a magnification factor M = 2.8. (b) Intensity profile along the marked line on Fig. 3(a).

Eq. (1), the Laplacian and gradient differentials of the rapid phase shifts generated large x-ray intensity variations, which manifest as the bright-dark fringes flank along the bubble rims in Fig. 3(a). Figure 3(b) shows a profile of image intensities along the marked dash line on Fig. 3(a), as the line traces the same positions as indicated by the dash line on Fig. 2(a). The downward and upward overshooting of the intensity values in the profile represent the bright and dark fringes at the bubble boundaries in phase contrast image Fig. 3(a). These up-down bipolar overshootings of intensities are much larger than the background noise, hence, the noise gets masked in Fig. 3(a). While the edge-enhancement generated by phase-contrast is generally useful for imaging the wrap, however, such edge-enhancements may lead interpretation errors in the characterization of the wrap's structure and composition. For example, in Fig. 3(a), the dark fringes flanked the enhanced bubble rims may be confused with possible structural breaks in the wrap sample, although we knew in advance that this wrap sample is free of any damage. In order to fully exhibit the wrap's phase contrast and correctly characterize the bubble wrap, it is necessary to perform the phase retrieval. In order to retrieve the wrap's phase-shift map from the wrap's radiograph [Fig. 2(a)] and its phase contrast image [Fig. 3(a)], we first employed the TIE-based phase retrieval formula Eq. (2). The retrieved phase map with the TIE-method is shown Fig. 4(a). Apparently, the phase retrieval failed completely, since no bubble is recognizable in Fig. 4(a). Although the failure can be

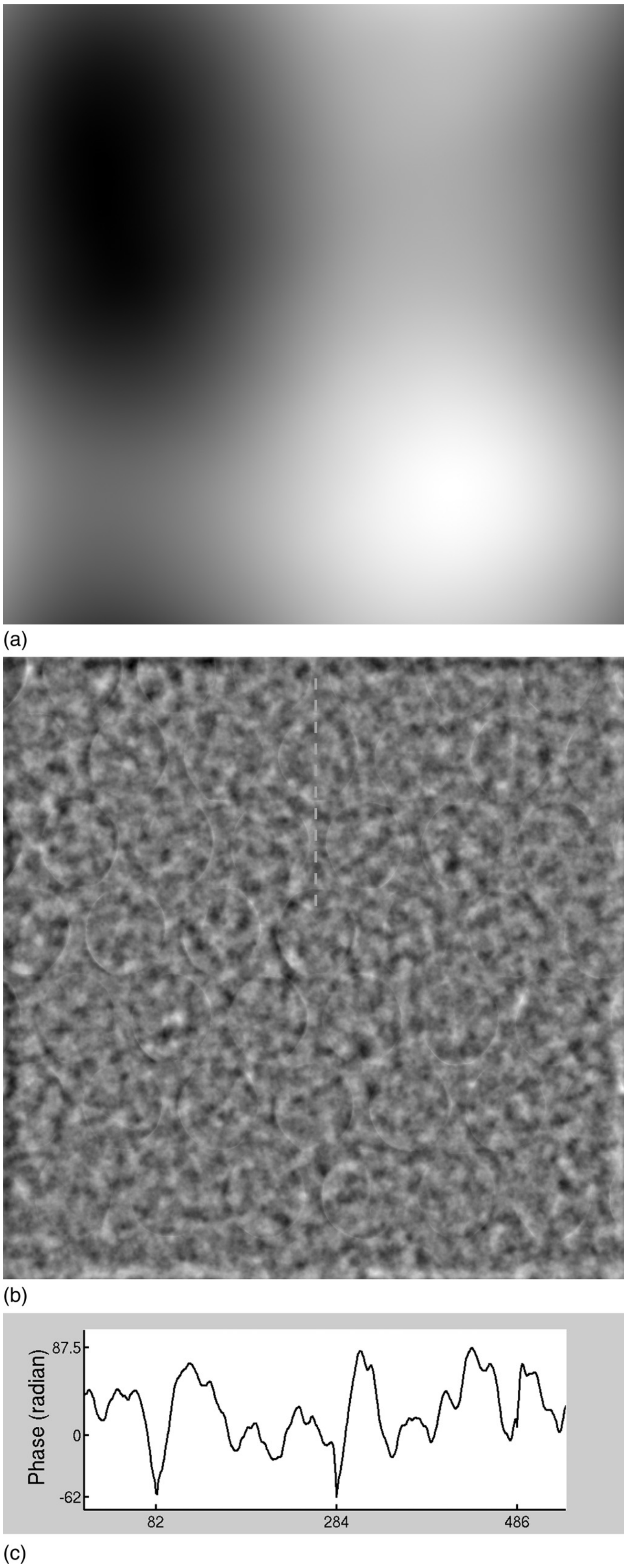

FIG. 4. Retrieved phase maps of the bubble wrap. (a) With the TIE-based method. (b) With the TIE-based method and Tikhonov regularization. (c) Profile of the retrieved phase values along the marked line on (b).

ascribed to the high-levels of the quantum noise presented in the radiograph of Fig. 2(a), but it is rooted in the intrinsic instability of the TIE-method. As we pointed out in Sec. II, the inverse Laplacian operator ∇^{-2} plugs in the zero-frequency singularity into the TIE-base phase retrieval formula Eq. (2). The singularity amplified the noise randomly embedded in the projections and results in the failure in the phase retrievals. To mend the instability of the TIE-method, one can try to apply the regularization techniques to tame the singularity-caused problems. A common regularization technique in the literature is Tikhonov regularization.[22] With this regularization scheme, one replaces the inverse Laplacian operator ∇^{-2} by a pseudodifferential operator $\nabla^2/[(\nabla^2)^2+\alpha^2]$, where α is the regularization parameter, which is roughly proportional to the images noise-signal ratios of the images.[22] In essence, Tikhonov regularization seeks the minimum-norm, least squares solution of Eq. (2). While the Tikhonov regularization of the inverse Laplacian operator may tame the instability, it sacrifices the phase retrieval accuracies. The performance in phase retrieval of Tikhonov regularization is highly dependent on the amounts of noise presented in the images. The regularization parameter α was selected through a trial by comparing the phase maps retrieved with a wide range of α-values such as $\alpha = \Delta u^2$, $5\,\Delta u^2$, $10\,\Delta u^2$, $50\,\Delta u^2$, $100\,\Delta u^2$, $200\,\Delta u^2$, $300\,\Delta u^2$, and $500\,\Delta u^2$, where Δu is the frequency sampling-step used in the phase retrieval. Figure 4(b) is the wrap phase map retrieved using the TIE-method and Tikhonov regularization with $\alpha = 200$ and $\Delta u^2 = 3.782 \times 10^{-8}\,\mu\text{m}^{-2}$, which was the α -value for the best results as determined from the trial. Apparently, these retrieval results are very unsatisfactory. In Fig. 4(b), the bubble rims are hardly visible in the extremely cluttered background. Figure 4(c) shows the profile of the retrieved phase values along the marked dash line on Fig. 4(b). As we will explain below that these phase values are grossly erroneous.

As a comparison, we have applied the AP-based method to the wrap's images in Figs. 2(a) and 3(a) for the phase retrieval as well. Following the method's iteration flow chart in Fig. 1, we succeeded in retrieving the wrap's phase map of the bubble wrap with ten iteration steps. Figure 5(a) is the retrieved phase map of the wrap with the AP-based method. In a stark contrast to Figs. 4(a) and 4(b) where the bubble rims are hardly visible, the bubble rims are prominently depicted in Fig. 5(a). A profile of retrieved phase values along the marked line on Fig. 5(a) is shown in Fig. 5(b). Note that all the marked lines in Figs. 3(a), 4(b), and 5(a), respectively correspond to the same line defined on the bubble wrap. In this way, one can easily compare the three profiles shown in Figs. 3(b), 4(c), and 5(b). In order to study the quantitative aspects of the retrieved phase maps of the wrap, remember that the amount of phase shift along a ray is given by $\varphi(\vec{r}) = -\lambda r_e \rho_e T_e(\vec{r})$, here, ρ_e denotes polyethylene film's electron density and $T_p(\vec{r})$ denotes projected thickness of polyethylene along the ray. Note that x-ray phase shifts should be of negative values, as x-ray refractive indices of tissues and materials are complex and their real part are less than one. The x-rays traversed longer paths in polyethylene at the bubble rims and incurred larger phase shifts, as compared to other parts of the wrap. For example, the three sharp negative peaks in the profile Fig. 5(b) reflect the large x-ray phase shifts incurred at the three rim locations along the marked line in Fig. 5(a). In order to gauge the accuracies of the retrieved phase values profiled in Fig. 5(b), one has to know the values of $T_p(\vec{r})$, the projected thicknesses in polyethylene films. Apparently, $T_p(\vec{r})$ depends on the local curvatures of bubble domes and the incident angles of the rays. While it is hard to measure $T_p(\vec{r})$ values in the bubbles, we measured the thicknesses of the flat bases between bubbles using a caliber ruler, and we found that the base thickness was about 0.055 mm. Knowing that the molecular formula of the low-density polyethylene film is $(C_2H_4)_n$ and its mass density is 0.925 g/cm^3, we calculated its electron density as $3.18 \times 10^{23}/\text{cm}^3$. Assuming approximately all rays have normal incidence, we find that the approximate phase shifts at the flat bases between bubbles is about -4.2 radian. On the other hand, according to the phase profile in Fig. 5(b), the average phase shift at the flat bases between bubbles is -1.05 radian. Obviously, these two estimates of the phase values though different, but are reasonably close. In comparison, the phase profile in Fig. 4(c), which was obtained by using the TIE-based method with Tikhonov regularization, depicts just messy up-down peaks buried in cluttered and

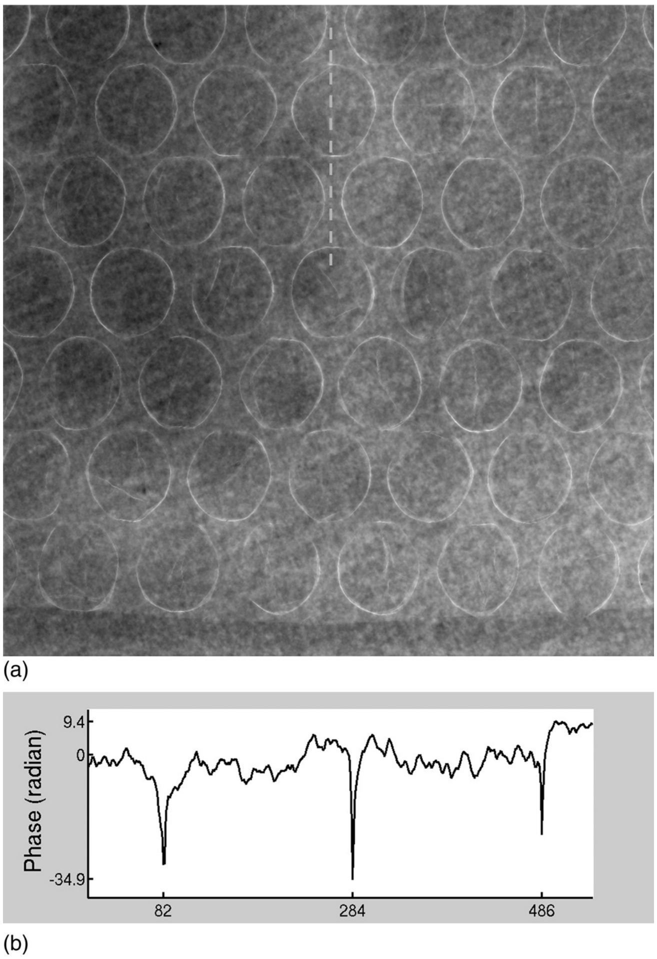

FIG. 5. (a) Retrieved phase maps of the bubble wrap with the AP-based method. (b) Profile of the retrieved phase values along the marked line on (a).

noisy background. In the phase profile, Fig. 4(c) only two negative peaks at the rims are barely recognizable, and the third expected negative peak completely disappears. According to this profile, the phase-shift values at the bases fluctuate over a wide range from 0 to $+87.5$ radian with an average of $+27.3$ radian, while x-ray phase shifts should be negative. Hence, the average phase value of flat bases estimated based on the profile, Fig. 4(c) is in a gross discrepancy with the thickness measurement-based estimate. Therefore, the above comparisons show clearly that the AP-based phase retrieval method is shown to be superior to the TIE-based method, regardless if the Tikhonov regularization is used, in performing the phase retrieval for the bubble wrap.

Before ending this section, we want to demonstrate the usefulness of performing the phase retrieval for tissue and material characterizations by comparing the bubble wrap's phase map in Fig. 5(a) to its phase contrast image in Fig. 3(a). As we pointed out earlier, the dark fringes which are flanking the bubble rims in the phase contrast image Fig. 3(a), may be confused for indicating possible structural breaks in the bubble wrap. In contrast to Fig. 3(a) riddled with the dark fringes, the retrieved phase map Fig. 5(a) does not present any dark fringes at all. This observation is also verified by comparing the phase profile Fig. 5(b) to the intensity profile Fig. 3(b). The up-down bipolar overshootings appearing in Fig. 3(b) disappear in the phase profile Fig. 5(b), where only sharp downward peaks present for depicting the large phase shifts at the bubble rims. Therefore, the wrap's phase map Fig. 5(a) clarifies the nature of the dark fringes in Fig. 3(a) such that these dark fringes do not indicate any structural break in the wrap sample.

IV. DISCUSSION AND CONCLUSIONS

This study demonstrates that the robustness against noises of a phase retrieval method is critical for the qualities of the retrieved phase map. Specifically, the striking differences between the retrieved phase maps in Figs. 4(a) and 4(b), and Fig. 5(a) underline the importance of removing the zero-frequency singularity that is intrinsic to the TIE-based method. While the TIE-based phase retrieval method is computational effective for the cases with strong phase contrast effects and low noise levels,[11,12] it completely failed in retrieving the phase map of the bubble wrap, as is shown in Figs. 4(a) and 4(b). This is because the noise problem is especially challenging for the case at hand, as the bubble wrap has very low attenuation contrast and only moderate x-ray exposures were applied in bubble image acquisitions. From mathematical viewpoint, the TIE-based phase retrieval formula Eq. (2) is ill-posed, since it involves the inverse Laplacian operator ∇^{-2} that owns a zero-frequency singularity. Beyond the mathematics formality, this zero-frequency singularity reflects the fact that the phase contrast projection is insensitive to the slow variations of x-ray phase shifts. Seeking to recover the phase shifts by comparing the two projection images contaminated with noise, the TIE-based method has amplified the noise in retrieving the slowly varying phase shifts and ruined the phase retrieval completely. The Tikhonov regularization mends the singularity problem by replacing the inverse Laplacian operator ∇^{-2} in Eq. (2) by a pseudodifferential operator $\nabla^2/[(\nabla^2)^2+\alpha^2]$ with a regularization parameter $\alpha^2 > 0$. As is shown in Fig. 4(b), this regularization made some but only little improvement compared to Fig. 4(a) as the bubbles start to appear in the phase map but are still hardly visible. From the mathematical formulation of the Tikhonov regularization technique, it is clear that Tikhonov regularization just limits the overall magnitude of the errors caused by the noise in the retrieved phase map, but the details of the original phase map could still get lost in the retrieval.[22] The AP-based method mends the singularity problem by utilizing the correlations between x-ray attenuation and x-ray phase shifts generated by tissues or materials, as is shown in Eq. (8). In a sense, the AP-based method utilizes the object's x-ray attenuation to get rid of the low-frequency singularity and the associated noise amplification. This physics-motivated regularization scheme for the AP-based method is expected to be more effective than Tikhonov regularization in phase retrievals. The greatly improved quality of the retrieved phase map shown in Fig. 5(a), as compared to Figs. 4(a) and 4(b), validates this expectation. Hence, the performance differences of these phase retrieval methods underscore the importance of developing an effective method to remove the singularity that is intrinsic to the TIE-based method. After all, the high noise levels in the acquired images still take tolls on the quality of the phase map Fig. 5(a) retrieved the AP-method, where the noise are quite visible. While increasing radiation doses used in the projections is a possible solution for improving phase retrievals, but the radiation dose constraints are stringent in many applications. In clinical applications, it is imperative to limit and reduce radiation doses involved in the imaging. Therefore, more research is needed for developing ever-improved phase retrieval methods for future clinical applications of phase contrast imaging.

Other factors, which are less critical to the robustness of phase retrieval but may affect the accuracies of retrieved phase maps, include the detector calibrations such as the flat-field and gain corrections, and the ways to incorporate the spectral averaging effects of polychromatic x-rays. In fact, the residual background nonuniformity in the acquired images [Figs. 2(a) and 3(a)] also caused variations in the background phase values in Fig. 5 and reduced their accuracies. A careful detector calibration in future experiments should avoid this kind of problem. In addition, note that x-ray wavelength enters as an important parameter in Eq. (2) for the TIE-based method, and in the flow chart in Fig. 1 for the AP-based method. The average x-ray wavelength used in the phase retrievals should represent the wavelength's linear and nonliner effects averaged over the exiting x-rays spectrum and the detector's spectral response. For the TIE-based method, several works discussed the ways of performing the spectral averages over polychromatic x-rays.[8,23] We did not use these techniques in this work, because the TIE-based method in any way failed the wrap's phase retrieval. In this work, we simply use the estimated average photon energy of the incident x-ray to incorporating the spectral averaging. In the future, we may develop more elaborated ways for incorporating the spectral averaging effects. Finally, we mention that one could as well employ a special phase retrieval method for the simple samples such as the bubble wrap. This special method works specifically for the single-material homogeneous samples, as long as the linear attenuation coefficient and refractive index of this material are provided. In this special method, the phase map of a single-material sample can be retrieved from just a single phase contrast image of the sample.[24] The air-bubble wrap can be approximately treated as a single-material sample as the air in bubbles contributes negligibly to x-ray attenuation and phase shifts. In this work, we do not compare this special method for single-material samples to the TIE-based and AP-based methods, since both the TIE-based and AP-based methods are the general phase retrieval methods applicable for any general objects of inhomogeneous materials.

In summary, in this work, we compared the robustness of two phase retrieval methods, the TIE-based method and the AP-based method, by analyzing the retrieved phase maps from the experimental projection images of an air-bubble wrap. We showed that the TIE-based method, regardless if the Tikhonov regularization is used, failed in retrieving the wrap's phase map. In contrast, in the wrap phase map retrieved by using the AP-based method bubbles are clearly recovered. The retrieved phase values with this method are reasonably close to the estimate based on the thickness-based measurement. The stark performance differences of the two methods are rooted in their different techniques employed to deal with the singularity problem. This comparison shows that the conventional TIE-based phase retrieval method, regardless of using Tikhonov regularization or not, is unstable against the noise in the wrap's projection images, while the AP-based phase retrieval method is shown in these experiments to be superior to the TIE-based method for the robustness in performing the phase retrieval.

ACKNOWLEDGMENTS

This research was supported in part by the Department of Defense Breast Cancer Research Program under Award No. W81XWH-08-1-0613 and the NIH Grant No. R01CA142587. H. Liu would like to acknowledge the support of Charles and Jean Smith Chair endowment fund as well.

---

[a] Author to whom correspondence should be addressed. Electronic mail: xwu@uabmc.edu

[1] A. Snigirev *et al.*, "On the possibilities of x-ray phase contrast microimaging by coherent high-energy synchrotron radiation," Rev. Sci. Instrum. **66**, 5486–5492 (1995).

[2] S. Wilkins, T. Gureyev, D. Gao, A. Pogany, and A. Stevenson, "Phase contrast imaging using polychromatic hard x-ray," Nature **384**, 335–338 (1996).

[3] A. Pogany, D. Gao, and S. Wilkins, "Contrast and resolution in imaging with a microfocus x-ray source," Rev. Sci. Instrum. **68**, 2774–2782 (1997).

[4] P. Cloetens, R. Barrett, J. Baruchel, J.-P. Guigay, and M. Schlenker, "Phase objects in synchrotron radiation hard X-ray imaging," J. Phys. D: Appl. Phys. **29**, 133–146 (1996).

[5] C. J. Kotre and I. P. Birch, "Phase contrast enhancement of x-ray mammography: A design study," Phys. Med. Biol. **44**, 2853–2866 (1999).

[6] F. Arfelli *et al.*, "Mammography with synchrotron radiation: Phase-detected Techniques," Radiology **215**, 286–293 (2000).

[7] E. Donnelly and R. Price, "Effect of kVp on edge-enhancement index in phase-contrast radiography," Med. Phy. **29**, 999–1002 (2002).

[8] X. Wu and H. Liu, "Clinical implementation of phase contrast x-ray imaging: Theoretical foundation and design considerations," Med. Phys. **30**, 2169–2179 (2003).

[9] X. Wu and H. Liu, "A new theory of phase-contrast x-ray imaging based on Wigner distributions," Med. Phys. **31**, 2378–2384, (2004).

[10] M. Teague, "Deterministic phase retrieval: a Green's function solution," J. Opt. Soc. Am. **73**, 1434–1441 (1983).

[11] K. Nugent, T. Gureyev, D. Cookson, D. Paganin, and Z. Barnea, "Quantitative phase imaging using hard x rays," Phys. Rev. Lett. **77**, 2961–2965 (1996).

[12] L. Allen and M. Oxley, "Phase retrieval from series of images obtained by defocus variation," Opt. Commun. **199**, 65–85 (2001).

[13] A. Yan, X. Wu, and H. Liu, "An attenuation-partition based iterative phase retrieval algorithm for in-line phase-contrast imaging," Opt. Express **16**, 13330–13341 (2008).

[14] P. Cloetens, R. Mache, M. Schlenker, and S. Lerbs-Mache, "Quantitative phase tomography of Arabidopsis seeds reveals intercellular void network," Proc. Natl. Acad. Sci. **103**, 14626–14630 (2006).

[15] T. Gureyev, D. Paganin, G. Myers, Ya. Nesterets, and S. Wilkins, "Phase-and-amplitude computer tomography," Appl. Phys. Lett. **89**(1–3), 034102 (2006).

[16] X. Wu, H. Liu, and A. Yan, "Phase-contrast x-ray tomography: Contrast mechanism and roles of phase retrieval," Eur. J. Radiol. **68**, S8–S12 (2008).

[17] X. Wu and H. Liu, "Phase-space evolution of x-ray coherence in phase-sensitive imaging," Appl. Opt. **47**, E44–E52 (2008).

[18] A. Yan, X. Wu, and H. Liu, "Performance analysis of the attenuation-partition based iterative phase retrieval algorithm for in-line phase-contrast imaging," Opt. Express **18**, 16074–16089 (2010).

[19] N. A. Dyson, *X-rays in Atomic and Nuclear Physics* (Essex, UK, 1973).

[20] X. Wu, H. Liu, and A. Yan, "X-ray phase-attenuation duality and phase retrieval," Opt. Lett. **30**, 379–381 (2005).

[21] M. Born and E. Wolf, *Principle of Optics*, 6th ed. (Pergamon, Oxford, 1980).

[22] A. Tikhonov and V. Aresenin, *Solution of Ill-posed Problems* (Winston & Sons, Washington, 1977).

[23] B. D. Arhatari, K. Hannah, E. Balaur, and A. G. Peele, "Phase imaging using a polychromatic x-ray laboratory source," Opt. Express **16**, 19950–19956 (2008).

[24] D. Paganin, S. C. Mayo, T. E. Gureyev, P. Miller, and S. W. Wilkins, "Simultaneous phase and amplitude extraction from a single defocused image of a homogeneous object," J. Microscopy **206**, 33–40 (2002).

Journal of X-Ray Science and Technology 19 (2011) 509–519
DOI 10.3233/XST-2011-0310
IOS Press

The effects of x-ray beam hardening on detective quantum efficiency and radiation dose

Molly Donovan Wong[a], Xizeng Wu[b] and Hong Liu[a,*]
[a]*Center for Bioengineering and School of Electrical and Computer Engineering, University of Oklahoma, Norman, OK, USA*
[b]*Department of Radiology, University of Alabama at Birmingham, Birmingham, AL, USA*

Received 26 April 2011
Revised 19 July 2011
Accepted 29 July 2011

Abstract. The goal of this preliminary study was to investigate the effects of x-ray beam hardening on the detective quantum efficiency (DQE) and the radiation dose of an inline x-ray imaging system. The ability to decrease the risk of harmful radiation to the patient without compromising the detection capability would more effectively balance the tradeoff between image quality and radiation dose, and therefore benefit the fields of diagnostic x-ray imaging, especially mammography. The DQE and the average glandular dose were both calculated under the same experimental conditions for a range of beam hardening levels, corresponding to no added beam hardening and two thicknesses each of Rhodium (Rh) and Molybdenum (Mo) filters. The dose calculation results demonstrate a reduction of 15% to 24% for the range of beam hardening levels. The comparison of all quantities comprising the DQE exhibit very close correlation between the results obtained without added beam hardening to the results corresponding to the range of beam hardening levels. For the specific experimental conditions utilized in this preliminary study, the results are an indication that the use of beam hardening holds the potential to reduce the radiation dose without decreasing the performance of the system. Future studies will seek to apply this method in a clinical environment and perform a comprehensive image quality evaluation, in an effort to further evaluate the potential of beam hardening to balance the tradeoff between dose and image quality.

Keywords: Diagnostic x-ray imaging, beam hardening, radiation dose, detective quantum efficiency (DQE), noise equivalent quanta (NEQ), modulation transfer function (MTF), noise power spectrum (NPS)

1. Introduction

Throughout the history of mammography, the technology and methods have evolved with a consistent goal of improving the tradeoff between the risk of harmful radiation dose to the patient and the benefit of disease detection provided by improved image quality [1–4]. However, the physical formulation of the images, which relies solely on attenuation contrast, has remained the same. The similar composition

---

[*] Corresponding author: Hong Liu, Center for Bioengineering and School of Electrical and Computer Engineering, University of Oklahoma, 110 West Boyd Street, Devon Energy Hall 150, Norman, OK 73019, USA. Tel.: +1 405 325 4286; Fax: +1 405 325 7066; E-mail: liu@ou.edu.

0895-3996/11/$27.50 © 2011 – IOS Press and the authors. All rights reserved

of benign and malignant breast tissue produces very low attenuation contrast [5–7], which presents a considerable challenge for cancer detection in mammography. Unfortunately, current techniques utilized in mammography to improve the image quality also deliver an increased radiation dose. As a result, the challenge remains to more effectively optimize the tradeoff between image quality and radiation dose.

2. Background

Breast cancer typically arises in the glandular tissue [5,8]; therefore, the average glandular dose has been established as the standard measurement of radiation dose in mammography, and guidelines have been created by numerous national and international councils for its calculation and supervision in clinical environments [8–12]. The formula for calculation of the average glandular dose D_g is as follows [5,13, 14]:

$$D_g = D_{gN} \cdot X_{ESE}, \tag{1}$$

where D_{gN} is the normalized average glandular dose coefficient and X_{ESE} is the object entrance exposure. D_{gN} is determined by experimental and computer simulation methods based on the following factors: radiation quality (x-ray energy or half value layer), x-ray tube target material, filter material, breast thickness and breast tissue composition [5]. Due to the complicated nature of the calculations, as well as the small range of values in mammography for each of the D_{gN} calculation parameters, numerous studies have published tables of D_{gN} values that are widely used in clinical and research environments [13–16]. However, the values must typically be calculated directly in investigational studies, due to the use of parameters outside the standard values. This study will therefore apply a Monte Carlo process described previously [14,17,18].

A comprehensive quantitative determination of the performance of an x-ray imaging system is the detective quantum efficiency (DQE) [5,19,20], as it represents the transfer function of the SNR of the system, which is demonstrated by the following equation [5,19,21–24]:

$$DQE(f) = \frac{SNR_{OUT}^2}{SNR_{IN}^2} = \frac{S(0)^2 \cdot MTF(f)^2}{NPS(f) \cdot q} = \frac{NEQ(f)}{q}, \tag{2}$$

where the modulation transfer function (MTF) is a measurement of the frequency response of the system [5,19,23,25,26], the noise power spectrum (NPS) is a determination of the noise processed by the system [5,19,23,27–29], and $S(0)$ is the mean intensity of a large area signal, assuming a uniform x-ray beam absorbed by the detector. The noise equivalent quanta (NEQ) is a combination of the three quantities and describes the number of quanta recorded at each spatial frequency, which provides information regarding the maximum attainable value of the output SNR [22,30–33]. The photon fluence (q) is the number of incident photons per square millimeter, which is equal to the square of the input SNR for x-ray photons following a Poisson distribution [5]. In this preliminary study, comparisons were made of the DQE as well as the individual quantities, in an effort to provide a comprehensive investigation of the effects of beam hardening on the imaging performance.

Beam hardening is the removal of low energy photons from the x-ray beam before reaching the object, through the use of filtration or other objects placed in the path of the x-ray beam [5]. Low energy photons are absorbed more readily due to lower penetration ability [5]; therefore, removing them prior to x-ray exposure has the potential to reduce the patient dose without considerably decreasing the image quality, which would benefit the field of mammography by delivering a more effective balance between image quality and radiation dose. The goal of this study was therefore to provide an initial investigation of the effects of a range of beam hardening levels on the DQE and the average glandular dose.

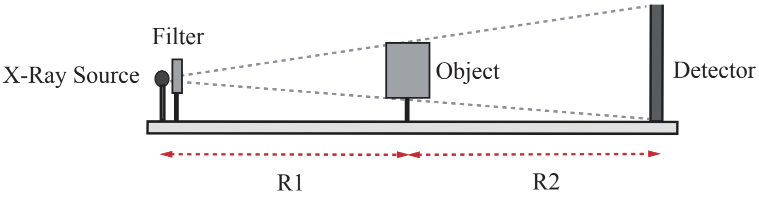

Fig. 1. Illustration of the x-ray configuration utilized in this study.

3. Materials and methods

3.1. Beam hardening

Beam hardening was provided through the use of the commonly used mammography filters Rhodium (Rh) and Molybdenum (Mo) [3–5]. The typical filter thicknesses utilized are 25 μm of Rh and 30 μm of Mo [5]. This study thus evaluated four filter thicknesses to provide a thorough comparison: 25 μm and 50 μm of Rh, and 30 μm and 60 μm of Mo. In addition, the investigation included a fifth mode without added filtration to provide a baseline for the comparison.

3.2. Inline x-ray imaging system and measurement components

The inline x-ray imaging system prototype utilized in this study consists of the imaging and measurement components mounted along an optical rail, which allows the use of a precise laser alignment process detailed in a previous study [34]. This also provides the ability to adjust the x-ray source-to-object (R1) and object-to-detector (R2) distances to facilitate the x-ray configuration utilized in this study, which is given in Fig. 1. In this study, R1 and R2 were both 91.44 cm, which produced a source-to-detector distance (R1+R2) of 182.88 cm. A longer distance than typical clinical mammography values was utilized to target future applications, as this configuration has been used for preliminary studies in inline phase contrast x-ray imaging indicating the potential to reduce the dose in mammography without negatively affecting the detection capability [7,35–39]. In addition, the air gap in this configuration provides a comparable amount of scatter rejection and resultant image quality improvement as the grid used in clinical systems [6,40,41]. The object was simulated by a BR12 phantom (Model 014A, CIRS, Norfolk, Virginia, USA) with a thickness of 5 cm. BR12 phantoms were developed to simulate a 50% glandular, 50% adipose tissue composition [42], and thus are used extensively for dose estimation purposes in clinical and research applications [2]. For comparison purposes, a second set of measurements were performed without the object, in an effort to evaluate the effect of the object on the measurements. The prototype system employs an x-ray tube with a Mo anode and a Be output window (UltraBright Microfocus Source, Oxford Instruments, Scotts Valley, California, USA). The tube operates between x-ray energies of 20 and 60 kV with an output power range of 10 to 60 W. The focal spot diameter varies with power output, thus a constant power output of 20 W was maintained in this study to ensure a constant focal spot diameter of 20 μm, which corresponds to a tube current of 0.33 milliamperes (mA). The image detection system employed in this study is a computed radiography system with mammography plates (Regius 190, Konica Minolta Medical Imaging, Wayne, New Jersey, USA), which provides a pixel pitch of 43.75 μm. Data linearization was performed through a process presented previously [26,31,43] to allow quantitative DQE analysis of the image data. The entrance exposure level was measured with a calibrated ionization chamber (10X9-180 ionization chamber, Model 9095 measurement system, Radcal Corporation, Monrovia, California, USA). Results from a previous study [24] indicated that utilizing the mean of numerous measurements reduces the error; therefore five measurements at each mode were acquired. The x-ray spectrum was measured through the use of an x-ray spectrometer with a $3 \times 3 \times 1$ mm^3 CdTe detector (Amptek Incorporated, Bedford, Massachusetts, USA), using a pair of tungsten collimators provided by the manufacturer.

3.3. Imaging parameters

An x-ray energy of 60 kV was utilized for the measurements acquired in this preliminary study. A higher x-ray energy than current clinical values was utilized in an effort to target future clinical applications in phase contrast imaging. Initial investigations in phase contrast imaging have indicated the potential of increasing the x-ray energy to reduce the dose without impacting the image quality [6, 39,44–46]. The ability to apply the technique of beam hardening to high energy phase contrast imaging could provide an additional dose reduction, which would further increase the benefits to the field of mammography. However, beam hardening alone could potentially be utilized in a current clinical environment for an immediate dose reduction; therefore, subsequent studies will further evaluate the feasibility of beam hardening through comparisons with a range of diagnostic energies, including current clinical mammography values.

The exposure time for each filter/object combination was selected to provide a constant detector entrance exposure of 10 mR, in an effort to provide a comparison based on similar radiation exposure for image acquisition. Once the exposure time was determined for each filter/object combination, the corresponding object entrance exposure was measured for calculation of the average glandular dose. Due to the constant detector entrance exposure for all combinations, the differences among the DQE and dose values was a result of only the factors controlled by this study.

3.4. Average glandular dose measurements

As demonstrated in Eq. (1), the average glandular dose D_g is based on the object entrance exposure (X_{ESE}) and the average glandular dose coefficient (D_{gN}). The object entrance exposure measurements were detailed previously, and the D_{gN} values for each mode were estimated with Monte Carlo simulations through a process detailed in previous studies [14,17,18]. The simulations assume the presence of an object with 50% adipose and 50% glandular tissue composition in the path of the x-ray beam. Therefore, the D_{gN} values were calculated only for the spectra acquired when the object is utilized.

3.5. Detective quantum efficiency measurements

The DQE calculation given in Eq. (2) consists of measurements of the MTF, NPS, $S(0)$ and q. First, the MTF was calculated through acquiring one image of a 10 μm wide slit camera (Nuclear Associates, Carle Place, NY, USA) for each filter/object combination. The MTF of each image was determined according to previous methods [25,47–50] by normalizing the absolute value of the line spread function (LSF), which is the response of the imaging system to a line stimulus [5]. Next, the noise power spectrum was measured through acquisition of 20 images for each mode in the absence of any additional objects in the path of the x-ray beam, which is referred to as a noise-only image. Due to the stochastic nature of noise in x-ray images, the experimental calculation of the two-dimensional (2D) NPS typically involves separating the noise-only image into numerous smaller regions and averaging the NPS values calculated from each region [22,27,29,31,43,51]. The one-dimensional (1D) NPS is then determined through the use of a slice consisting of four data lines parallel to and immediately adjacent to the axes [22,43].

Table 1
Average glandular dose calculations for an x-ray energy of 60 kV and 20 W with a 5 cm BR12 phantom, assuming 50% adipose, 50% glandular tissue composition. The exposure time was selected for each filter to provide a constant detector entrance exposure of 10 mR. The results indicate a dose reduction for all filters

Filtration	Object exposure (R)	D_{gN} (mrad/R)	D_g (mrad)	Dose reduction (%)
None	0.81	333.4	268.69	
25 μm Rh	0.61	343.8	210.02	22
50 μm Rh	0.56	366.6	203.82	24
30 μm Mo	0.68	337.0	229.17	15
60 μm Mo	0.63	356.0	222.86	17

The large area signal $S(0)$ was determined by calculating the mean pixel intensity of the 20 noise-only images within the region of interest utilized for calculation of the noise power spectrum. The value of q is determined experimentally through multiplying the detector entrance exposure by the photon fluence per unit exposure, which can be calculated from a measured x-ray spectrum [24,43,52].

4. Results and discussion

4.1. Average glandular dose

Comparisons of the average glandular dose calculated for each filter with the 5 cm BR12 object are given in Table 1, which provides the measured object entrance exposure and the corresponding range of D_{gN} values calculated from the Monte Carlo estimations. The last column presents the percentage of dose reduction provided by each filter as compared to the dose value obtained without filtration. The results demonstrate a notable dose reduction of 15% to 24% for the range of beam hardening levels. The filter corresponding to the maximum dose reduction was the 50 μm Rh filter. It is also interesting to note that the filter providing the second largest dose reduction was the 25 μm Rh filter, which provided a lower dose than both Mo filters.

4.2. Detective quantum efficiency

Comparisons of the x-ray spectra acquired for each beam hardening level are given in Fig. 2 (a) and (b), which correspond to the images acquired without an object and with the 5 cm BR12, respectively. The display range in both figures has been adjusted to display a subset of the full x-ray spectra range, in an effort to more effectively demonstrate the differences between the beam hardening levels in the region of interest around the peaks. The behavior in the low and high energy values not depicted exhibits a decreasing trend to 0 in both directions. The comparison without the object demonstrates the effects of beam hardening in removing low energy photons from the x-ray beam, while the comparison with the object illustrates the further hardening effects of the object on the x-ray beam.

Comparisons of the MTF, NPS, and NEQ values calculated for each beam hardening level are given in Figs 3 through 5, respectively, in which (a) and (b) correspond to the images acquired without an object and with the 5 cm BR12, respectively. In each of the comparisons without the object, the curve calculated without added beam hardening is noticeably different from the curves corresponding to the filters. However, when the 5 cm BR12 is utilized to simulate the human breast, the separation among the curves is much smaller, which is an encouraging indication that the use of filtration in a clinical

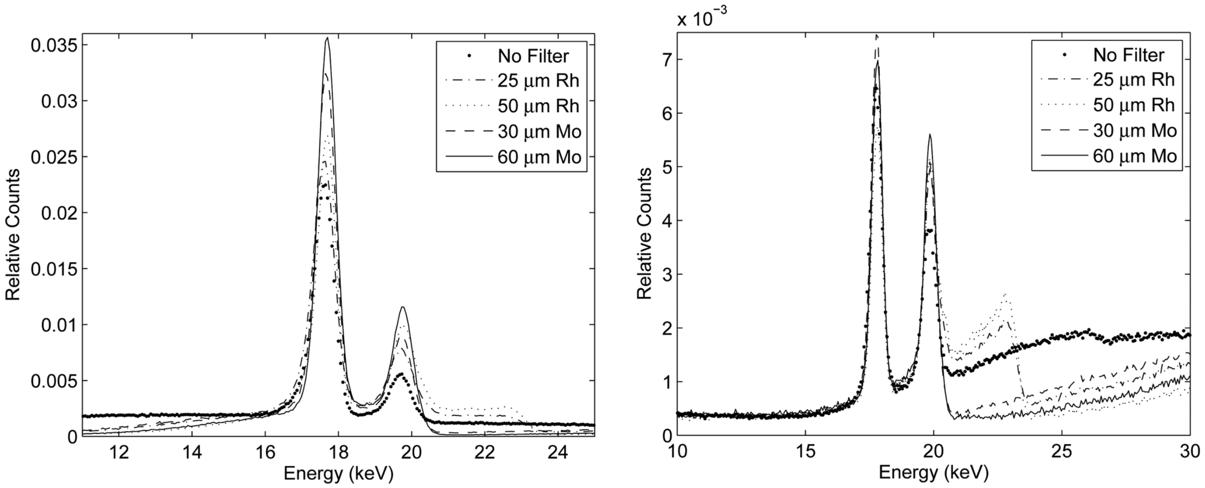

(a) (b)

Fig. 2. Comparison of the x-ray spectra corresponding to each beam hardening level. The spectra were acquired at 60 kV, 20 W (a) without an object in the path of the x-ray beam, and (b) with the 5 cm BR12 object in the path.

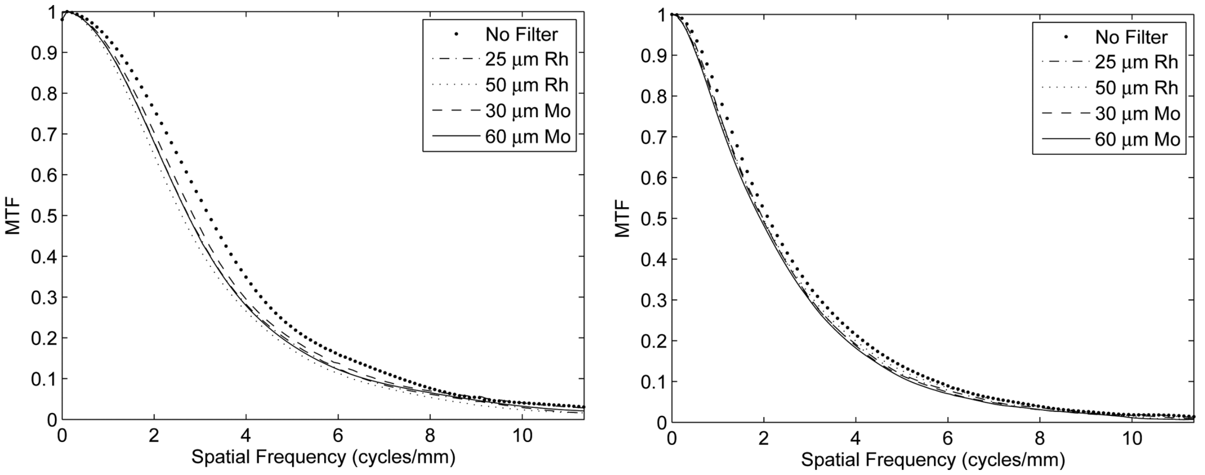

(a) (b)

Fig. 3. Comparison of the MTF curves corresponding to the beam hardening levels. The curves were calculated from slit camera images acquired at 60 kV, 20 W (a) without an object in the path of the x-ray beam, and (b) with the 5 cm BR12 object in the path.

environment may not negatively affect the imaging response of the system. For example, in Fig. 3(a), the shape of the MTF is affected by each level of added filtration, which can probably be attributed to the sensitivity of the x-rays to the filtration without an object in the path of the x-ray beam. When the object is utilized, the MTF for each beam hardening level is degraded in comparison to the corresponding MTF without the object, which indicates the negative effect of the object. This is intuitive, due to the amount of attenuation experienced within the object. In this comparison, the minimal difference between the MTF without filtration and the filtered MTFs indicates that beam hardening provides a limited amount of additional degradation to the imaging response of the system.

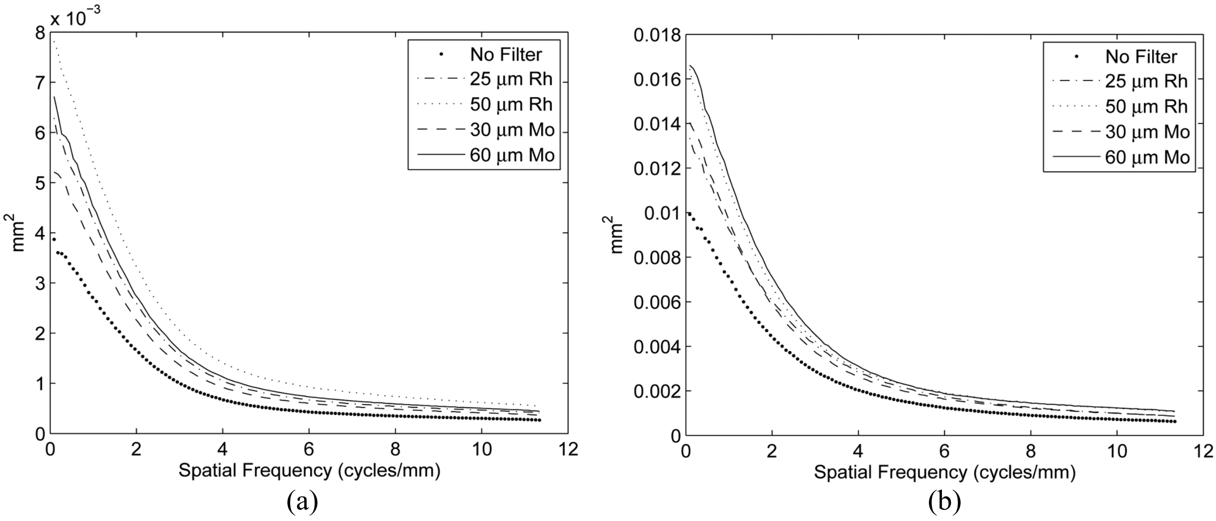

Fig. 4. Comparison of the NPS curves corresponding to the beam hardening levels. The curves were calculated from noise-only images acquired at 60 kV, 20 W (a) without an object in the path of the x-ray beam, and (b) with the 5 cm BR12 object in the path.

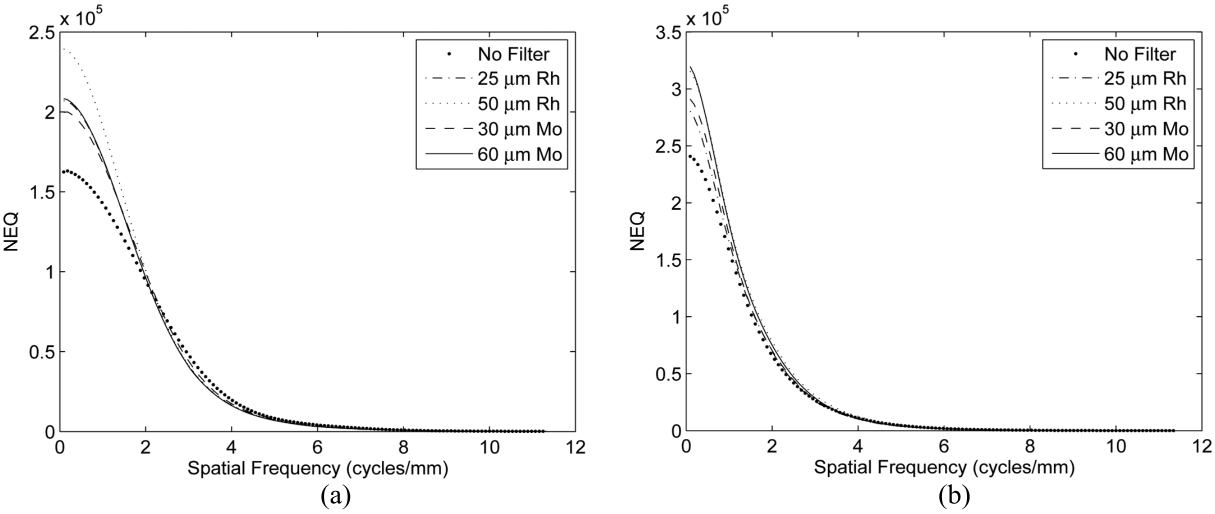

Fig. 5. Comparison of the NEQ curves corresponding to the beam hardening levels. The curves were calculated from the MTF, NPS and $S(0)$, (a) without an object in the path of the x-ray beam, and (b) with the 5 cm BR12 object in the path.

Next, comparisons of the q values corresponding to the beam hardening levels are given in Tables 2 and 3, which correspond to the measurements acquired without an object and with the 5 cm BR12, respectively, in the path of the x-ray beam. The results correlate with the D_{gN} coefficients, through exhibiting an increasing trend from the minimum value without added beam hardening to the maximum value with the 50 μm Rh filter, which also produced the largest D_{gN} value. This follows intuition, as the largest q value indicates the highest concentration of photons in the same surface area, which would also correspond to the largest dose coefficient.

Finally, comparisons of the DQE values for the beam hardening levels without an object and with

Table 2
Comparison of the photon fluence (q) values for the beam hardening levels, corresponding to the measurements acquired without an object in the path of the x-ray beam

Filtration	Photon fluence (q) (1/mm^2)
None	3.134×10^5
25 μm Rh	4.314×10^5
50 μm Rh	5.089×10^5
30 μm Mo	4.024×10^5
60 μm Mo	4.498×10^5

Table 3
Comparison of the photon fluence (q) values for the beam hardening levels, corresponding to the measurements acquired with the 5 cm BR12 object in the path of the x-ray beam

Filtration	Photon fluence (q) (1/mm^2)
None	7.087×10^5
25 μm Rh	7.636×10^5
50 μm Rh	8.288×10^5
30 μm Mo	7.618×10^5
60 μm Mo	8.243×10^5

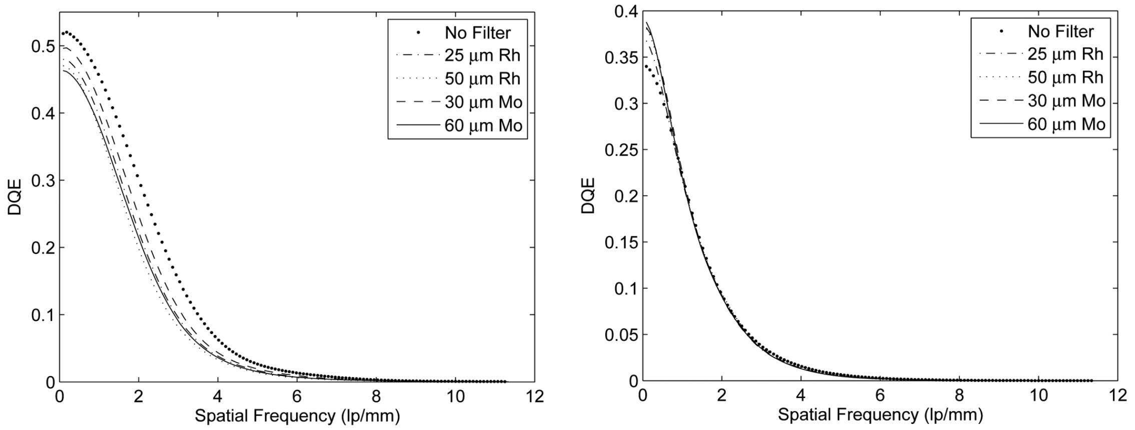

(a) (b)

Fig. 6. Comparison of the DQE curves corresponding to the range of beam hardening levels, (a) without an object in the path of the x-ray beam, and (b) with the 5 cm BR12 object in the path.

the 5 cm BR12 are provided in Fig. 6 (a) and (b), respectively. The results also exhibit much closer correlation between the curves acquired with the 5 cm BR12 than the curves generated without the object. Furthermore, within the DQE curves corresponding to the object, once again only a small divergence is distinguishable between the curve acquired without beam hardening and the curves corresponding to the range of beam hardening levels.

5. Conclusion

For the specific experimental conditions utilized in this preliminary study, the results of the dose and DQE comparisons are an initial indication that the use of beam hardening holds the potential to reduce the dose without decreasing the performance of the system. Subsequent studies will further evaluate the feasibility of beam hardening through a thorough investigation of any differences in subject contrast resulting from beam hardening, which could affect the image quality provided by the system. The ability of beam hardening to more effectively balance the tradeoff between dose and image quality would benefit the fields of diagnostic x-ray imaging, especially mammography. Future studies will also perform comparisons encompassing a range of diagnostic energies, including current clinical mammography values.

Acknowledgements

This study was supported in part by NIH-NCI grant R01CA142587, DoD BCRP grant W81XWH-08-1-613, and the Charles and Jean Smith Chair endowment fund.

References

[1] L. Bassett and R. Gold, The evolution of mammography, *American Journal of Roentgenology* **150** (1988), 493–498.
[2] W. Huda, E. Nickoloff and J. Boone, Overview of patient dosimetry in diagnostic radiology for the past 50 years, *Medical Physics* **35** (2008), 5713–5728.
[3] A. Karellas and S. Vedantham, Breast cancer imaging: A perspective for the next decade, *Medical Physics* **35** (2008), 4878–4897.
[4] J. Law, The development of mammography, *Physics in Medicine and Biology* **51** (2006), 155–167.
[5] J. Bushberg, J. Seibert, E. Leidholdt, Jr. and J. Boone, *The Essential Physics of Medical Imaging*, Second ed. Philadephia, Pennsylvania: Lippincott Williams & Wilkins, 2002.
[6] V. Ingal, Phase mammography-a new technique for breast investigation, *Physics in Medicine and Biology* **43** (1998), 2555–2567.
[7] C. Kotre and I. Birch, Phase contrast enhancement of x-ray mammography: a design study, *Physics in Medicine and Biology* **44** (1999), 2853–2866.
[8] American College of Radiology, *Mammography Quality Control Manual*, ACR, 1994.
[9] American Association of Physicists in Medicine, Equipment requirements and quality control for mammography, *AAPM Report 29*, 1990.
[10] Institute of Physical Sciences in Medicine, The Commissioning and Routine Testing of Mammographic X-Ray Systems, *IPSM Group Report 59*, 1989.
[11] International Commission on Radiological Protection, Managing patient dose in digital radiology, *ICRP Report 93*, 2003.
[12] National Council on Radiation Protection and Measurements, Mammography – a user's guide, *NCRP Report Number* **85** (1986), 40–48.
[13] J. Boone, Glandular Breast Dose for Monoenergetic and High-Energy X-ray Beams: Monte Carlo Assessment, *Radiology* **vol 213** (1999), 23–37.
[14] X. Wu, E. Gingold, G. Barnes and D. Tucker, Normalized Average Glandular Dose in Molybdenum Target-Rhodium Filter and Rhodium Target-Rhodium Filter Mammography, *Radiology* **193** (1994), 83–89.
[15] D.R. Dance, Monte Carlo calculation of conversion factors for the estimation of mean glandular breast dose, *Physics in Medicine and Biology* **35** (1990), 1211–1219.
[16] R.E. Hendrick, Standardization of image quality and radiation dose in mammography, *Radiology* **174** (1990), 648–654.

[17] X. Wu, G. Barnes and D. Tucker, Spectral dependence of glandular tissue dose in screen-film mammography, *Radiology* **179** (1991), 143–148.

[18] X. Wu, Breast Dosimetry in Screen Film Mammography, *Screen Film Mammography: Imaging Considerations and Medical Physics Responsibilities* (1991), 159–175.

[19] B. Hasegawa, *The Physics of Medical X-Ray Imaging*, Madison, Wisconsin: Medical Physics Publishing Corporation, 1990.

[20] IEC, Medical electrical equipment – Characteristics of digital imaging devices – Part 1: Determination of the detective quantum efficiency, *International Electrotechnical Commission International Standard 62220-1*, 2003.

[21] J. Dainty and R. Shaw, *Image Science*, New York: Academic Press, 1974.

[22] J. Dobbins III, D. Ergun, L. Rutz, D. Hinshaw, H. Blume and D. Clark, DQE(f) of four generations of computed radiography acquisition devices, *Medical Physics* **22** (October 1995), 1581–1593.

[23] ICRU, Medical Imaging – The Assessment of Image Quality, *International Commission on Radiation Units and Measurements* **54**, 1996.

[24] M. Wong, D. Zhang, J. Rong, X. Wu and H. Liu, Optimizing photon fluence measurements for the accurate determination of detective quantum efficiency, *Journal of Electronic Imaging* **18** (2009), 043010.

[25] M. Giger and K. Doi, Investigation of basic imaging properties in digital radiography. 1. Modulation transfer function, *Medical Physics* **11** (1984), 287–295.

[26] E. Samei and M. Flynn, An experimental comparison of detector performance for computed radiography systems, *Medical Physics* **29** (2002), 447–459.

[27] H. Jiang, W. Chen and H. Liu, Techniques to improve the accuracy and to reduce the variance in noise power spectrum measurement, *IEEE Transactions on Biomedical Engineering* **49** (2002), 1270–1278.

[28] C. Metz, R. Wagner, K. Doi, D. Brown, R. Nishikawa and K. Myers, Toward consensus on quantitative assessment of medical imaging systems, *Medical Physics* **22** (1995), 1057–1061.

[29] M. Williams, P. Mangiafico and P. Simoni, Noise power spectra of images from digital mammography detectors, *Medical Physics* **26**, (1999), 1279–1293.

[30] J. Dobbins III, Effects of undersampling on the proper interpretation of modulation transfer function, noise power spectra, and noise equivalent quanta of digital imaging systems, *Medical Physics* **22** (1995), 171–181.

[31] M. Flynn and E. Samei, Experimental comparison of noise and resolution for 2k and 4k storage phosphor radiography systems, *Medical Physics* **26** (1999), 1612–1623.

[32] J. Sandrik and R. Wagner, Absolute measures of physical image quality: Measurement and application to radiographic magnfication, *Med Phys* **9** (1982), 540–549.

[33] K. Fetterly, N. Hangiandreou, B. Schueler and E. Ritenour, Measurement of the presampled two-dimensional modulcation transfer function of digital imaging systems, *Med Phys* **29** (2002), 913–921.

[34] D. Zhang, M. Wong, X. Wu and H. Liu, A convenient alignment approach for x-ray imaging experiments based on laser positioning devices, *Medical Physics* **35** (2008), 4907–4910.

[35] E. Donnelly, R. Price and D. Pickens, Quantification of the effect of system and object parameters on edge enhancement in phase-contrast radiography, *Medical Physics* **30** (2003), 2888–2896.

[36] A. Pogany, D. Gao and S. Wilkins, Contrast and resolution in imaging with a microfocus x-ray source, *Review of Scientific Instruments* **68** (1997), 2774–2782.

[37] S. Wilkins, T. Gureyev, D. Gao, A. Pogany and A. Stevenson, Phase-contrast imaging using polychromatic hard x-rays, *Nature* **384** (1996), 335–338.

[38] D. Zhang, M. Donovan, L. Fajardo, A. Archer, X. Wu and H. Liu, Preliminary feasibility study of an in-line phase contrast x-ray imaging prototype, *IEEE Transactions on Biomedical Engineering* **55** (2008), 2249–2257.

[39] Y. Zhou, H. Pew, J. Rong, W. Chen, L. Fajardo, X. Wu and H. Liu, Phantom imaging with a prototype phase contrast radiography system, *SPIE* **6163** (2006), 61630E.

[40] M. Freedman, S. Lo, C. Honda, E. Makariou, G. Sisney, E. Pien, H. Ohara, A. Ishisaka and F. Shimada, Phase contrast digital mammography using molybdenum x-ray: clinical implications in detectability improvement, *SPIE* **5030** (2003), 533–540.

[41] S. Matsuo, T. Katafuchi, K. Tohyama, J. Morishita, K. Yamada and H. Fujita, Evaluation of edge effect due to phase contrast imaging for mammography, *Medical Physics* **32** (2005), 2690–2697.

[42] D. White, R. Martin and R. Darlison, Epoxy resin based tissue substitutes, *British Journal of Radiology* **50** (1977), 814–821.

[43] D. Zhang, J. Rong, R. Chu, X. Wu and H. Liu, Imaging characteristics of a high resolution computed radiography system, *Journal of X-Ray Science and Technology* **14** (2006), 273–282.

[44] F. Arfelli et al., Low-dose phase contrast x-ray medical imaging, *Physics in Medicine and Biology* **43** (Oct 1998), 2845–2852.

[45] E. Donnelly and R. Price, Quantification of the effect of kVp on edge-enhancement index in phase-contrast radiography, *Medical Physics* **29** (2002), 999–1002.

[46] P. Monnin, J. Hoszowska, J. Valley, R. Meuli and F. Verdun, Quantitative characterization of edge enhancement in phase contrast x-ray imaging, *Medical Physics* **31** (2004), 1372–1383.

[47] C. Bradford, W. Peppler and J. Waidelich, Use of a slit camera for MTF measurements, *Medical Physics* **26** (1999), 2286–2294.

[48] H. Fujita, D. Tsai, T. Itoh, K. Doi, J. Morishita, K. Ueda and A. Ohtsuka, A Simple Method for Determining the Modulation Transfer Function in Digital Radiography, *IEEE Transactions on Medical Imaging* **11** (March 1992), 34–39.

[49] P. Judy, The line spread function and modulation transfer function of a computed tomography scanner, *Medical Physics* **3** (1976), 233–236.

[50] F. Yin, M. Giger and K. Doi, Measurement of the presampling modulation transfer function of film digitizers using a curve fitting technique, *Medical Physics* **17** (1990), 962–966.

[51] J. Dobbins III, E. Samei, N. Ranger and Y. Chen, Intercomparison of methods for image quality characterization. II. Noise power spectrum, *Medical Physics* **33** (2006), 1466–1475.

[52] K. Fetterly and N. Hangiandreou, Image quality evaluation of a desktop computed radiography system, *Medical Physics* **27** (2000), 2669–2679.

Medical Physics Letter

X-ray phase-shifts-based method of volumetric breast density measurement

Xizeng Wu[a) and Aimin Yan
Department of Radiology, University of Alabama at Birmingham, Birmingham, Alabama 35233

Hong Liu
Center for Bioengineering and School of Electrical and Computer Engineering, University of Oklahoma, Norman, Oklahoma 73019

(Received 13 April 2012; revised 8 May 2012; accepted for publication 2 June 2012; published 21 June 2012)

Purpose: The high breast density is one of the biggest risk factors for breast cancer. Identifying patient having persistent high breast density is important for breast cancer screening and prevention. In this work the authors propose for the first time an x-ray phase-shifts-based method of breast density measurement.

Methods: When x ray traverses the breast, x ray gets not only its intensity attenuated but also its phase shifted. Studying the x-ray phase-shifts generated by the breast tissues, we derived a general formula for determining the volumetric breast density from the breast phase map. The volumetric breast density is reconstructed by retrieving the breast phase map from just a single phase-sensitive projection of the breast, through the use of an innovative phase retrieval method based on the phase-attenuation duality. In order to numerically validate this phase-shifts-based method for measuring the volumetric breast density, the authors performed computer simulations with a digitally simulated anthropomorphic breast phantom.

Results: Using the proposed phase-shifts-based method, we reconstructed the breast phantom's volumetric breast density, which differs from the phantom's intrinsic breast density by only 0.06%. In the presence of noises in the projection image, the reconstructed volumetric breast density differs from the phantom's intrinsic breast density by only 1.79% for a projection signal-to-noise-ratio (SNR) of 34. The error in reconstructed breast density is further reduced to 1.61% and 1.55% for SNR = 68 and SNR = 134, respectively, achieving good accuracies in the breast density determination.

Conclusions: The authors proposed an x-ray phase-shifts-based method of measuring the volumetric breast density. The simulation results numerically validated the proposed method as a novel method of breast density measurement with good accuracies. © *2012 American Association of Physicists in Medicine*. [http://dx.doi.org/10.1118/1.4729838]

Key words: X-ray phase contrast, phase retrieval, breast density

I. INTRODUCTION

As is well known, breast cancer is the most common cancer among American women and is the leading cause of cancer related death among women between 35 and 50 yr of age in the United States. In recent years scientific studies have found that the breast cancer risk is directly linked to the breast density, the relative amount of the dense fibroglandular tissue versus fatty adipose tissue, namely, the fraction of the volume of fibroglandular tissue in the breast. As the fibroglandular tissues appear "hyperdense" in mammograms because of its relatively high attenuation coefficients, studies found that high breast density inferred from mammograms is associated with twofold to fourfold increase in risk for breast cancer.[1–3] Although the magnitude of that risk is still under some debate, the scientific literature holds that high breast density is one of the biggest risk factors for breast cancer.[2] Identifying patient having persistent breast density may benefit these patients from a more frequent breast cancer screening for early detection of breast cancer or from some other preventive measure such as the chemoprevention. The public awareness of breast density as a high risk factor for breast cancer has recently been pushing new legislature and regulatory efforts for providing patients the breast density information from their breast imaging exams. Therefore, in recent years there is strong interest in developing methods to measure volumetric breast density (VBD). The most straightforward method of measuring volumetric breast density would be from the three-dimensional x-ray breast image techniques such as breast computed tomography (CT), which is still in its early period of development. Currently, it is most practical to determine volumetric breast density from the two-dimensional imaging techniques such as mammography.[4–10] The mammography-associated methods are all based on the small differences in tissue attenuation of the dense breast fibroglandular tissue and fatty adipose tissue. In some methods, breast density is measured by the categorical scores based on the tissue radiographic opacity on a mammogram acquired with a screen/film based or digital system.[4,9,10] However, such methods are limited by lack of consensual reference standards and are often flawed by the subjectivity. The improved methods reported in the literature all need to conduct elaborated phantom-based system calibrations for breast density measurement. Some of these methods require simultaneous exposure of a calibration phantom alongside the breast for the system calibrations.[7,8,10] These laborious calibrations are indeed required, because mammography exams are conducted with different tube targets/filters and voltages, and the linear attenuation coefficients of breast tissues vary in complicated ways as the x-ray energy changes. Therefore, in search for a more effective method of breast density measurement, it would be desirable to develop a method to measure breast density directly rather than measuring tissue attenuation as a surrogate of the breast density.

In this work we propose to determine the breast density by direct probing the projected electron densities of breast fibroglandular tissue and adipose tissue through the use of the retrieved phase map of a breast. Note that the electron density of a tissue is the intrinsic property of the tissue and it is independent of x-ray photon energies employed. In Secs. II–IV, we lay down a framework of a phase-shifts-based method of determining the volumetric breast density. We show how to retrieve the breast phase map from a single phase-sensitive projection of the breast. In order to validate this novel breast density measurement method, we discuss the volumetric breast density values reconstructed from computer simulations with a digitally simulated anthropomorphic breast phantom.

II. METHODS

Our method of breast density measurement is based on an x-ray phase-sensitive imaging technique. As x rays traverse the breast, x rays undergo phase-shifts in addition to the intensity attenuation. The amount of x-ray phase-shift φ generated by tissues is equal to $\varphi = -\langle\lambda\rangle r_e \int_{\text{ray}} \rho_e(s)ds = -\langle\lambda\rangle r_e \rho_{e,p}$, where $r_e = 2.818 \times 10^{-15}$ m is the classical electron radius and λ denotes the x-ray wavelength.[11–15] In this paper the angle bracket $\langle\cdot\rangle$ denotes the spectral average over the detected polychromatic x-ray spectrum, so $\langle\lambda\rangle$ denotes the average x-ray wavelength. Here, ρ_e denotes the tissue electron density and $\rho_{e,p} = \int_{\text{ray}} \rho_e(s)ds$ is the projected electron density summed over the x-ray path. Therefore, once we have retrieved the phase map $\varphi(\vec{r})$ of a breast through its projection image, where $\vec{r}$ denotes the position on the phase map, we are able to find the projected electron density map $\rho_{e,p}(\vec{r})$ of the breast as $\rho_{e,p}(\vec{r}) = (-1/\langle\lambda\rangle r_e)\varphi(\vec{r})$. Using the $\rho_{e,p}(\vec{r})$-map of a breast, we can determine the volumetric breast density of the breast as follows. For the purpose of breast density determination, we may assume that there are only two types of tissues in breast: the fibroglandular tissue with an electron density $\rho_{e,\text{fg}}$ and the adipose tissue with an electron density $\rho_{e,\text{ad}}$. Note that the values of $\rho_{e,\text{fg}}$ and $\rho_{e,\text{ad}}$ are available from the measured data in the literature, $\rho_{e,\text{fg}} = 3.448 \times 10^{23}/\text{cm}^3$ and $\rho_{e,\text{ad}} = 3.108 \times 10^{23}/\text{cm}^3$.[16] Let $m(\vec{r})$ be the fibroglandular-tissue fraction along a projection-ray detected at position $\vec{r}$, then we have

$$\rho_{e,p}(\vec{r}) = [m(\vec{r}) \cdot \rho_{e,\text{fg}} + (1 - m(\vec{r})) \cdot \rho_{e,\text{ad}}] \cdot T(\vec{r}), \tag{1}$$

where $T(\vec{r})$ denotes the ray path-length in the breast. In mammography, the breast is always kept forcefully and uniformly compressed for spreading breast tissues and reducing the scatters. The compressed breast thickness is always automatically measured and indicated by the imaging system. As long as the source-breast distance is significantly larger than the breast lateral size, the values of $T(\vec{r})$ are approximately equal to the compressed thickness T_c of the breast, except for the breast anterior edge, which is not in contact with the compression paddle and constitutes only a very small portion of the breast volume. With this approximation we found that the fibroglandular-tissue fraction along the ray-$\vec{r}$ as given by

$$m(\vec{r}) = \frac{-\varphi(\vec{r})/\langle\lambda\rangle r_e - \rho_{e,\text{ad}} T_c}{(\rho_{e,\text{fg}} - \rho_{e,\text{ad}})T_c}. \tag{2}$$

While $m(\vec{r})$ specifies the fibroglandular-tissue fraction along the ray-$\vec{r}$, the breast density, as a risk factor defined in the literature, should be quantified the fibroglandular-tissue fractions averaged over the whole breast. Hence, a map of these $m(\vec{r})$-values, which we call the $m(\vec{r})$-image of a breast, is the map of the breast's fibroglandular-tissue fractions. The VBD can then be computed from the $m(\vec{r})$-image as VBD $= \sum_{\text{breast}} m(\vec{r})/N_p$, where the sum is taken over the projected breast image and N_p is the total pixel number in the projected breast. Hence, the volumetric breast density can be found from the breast phase map as

$$\text{VBD} = \frac{\sum_{\text{breast}} (-\varphi(\vec{r})/\langle\lambda\rangle r_e - \rho_{e,\text{ad}} T_c)}{N_p T_c (\rho_{e,\text{fg}} - \rho_{e,\text{ad}})}. \tag{3}$$

In order to implement a phase-shifts-based method of measuring the breast density, it calls for a low radiation dose yet phase-sensitive technique to recover the phase-shifts generated by the breast, as the average glandular doses involved should be closely controlled and monitored as is in current mammography. Although the differences in x-ray phase-shifts between different tissues are about 1000 times greater than their differences in the attenuation, current technology is unable to directly measure the phase-shifts because of the extremely high frequencies of x rays.[11–13] Breast phase-shifts have to be retrieved from the phase-sensitive images of the breast. The proposed Eq. (3)-based method of breast density measurement can be applied to any of phase-sensitive imaging techniques such as the inline or the grating-based techniques. Among these phase-sensitive techniques, the inline phase-sensitive imaging is the simplest to be implemented, since the inline technique does not need any x-ray optics such as the crystal analyzers or high line-density transmission gratings. In this work, we study the inline phase-sensitive imaging only. The setting for the inline technique is similar to that of conventional mammography, provided one uses a small focal spot and a sufficiently large object-detector distance.[12,14,15] In the inline phase-sensitive imaging, as x rays traverse the breast, x rays undergo phase-shifts and intensity-attenuation, and then diffract freely over a distance upon detection. The resulted image exhibits not only the tissue attenuation contrast, but also the tissue phase contrast, which manifests as the dark-bright fringes at tissues' boundaries and interfaces in the image.[11–15] In order to measure the breast density by using the phase map of a breast, one needs to retrieve the breast phase map from its phase-sensitive projection images.

The phase retrieval is based on x-ray propagation equation, which reveals how the phase-shifts are encoded in the image intensity variations. A convenient form of the propagation equation is the so-called transport of intensity equation (TIE):[17,18]

$$I(\vec{r}_D) = \frac{I_{\mathrm{in}}}{M^2}\left\{A_o^2(\vec{r}_D/M) - \frac{R_2\langle\lambda\rangle}{2\pi M}\nabla\cdot\left(A_o^2(\vec{r}_D/M)\nabla\varphi(\vec{r}_D/M)\right)\right\}, \tag{4}$$

where $I\,(\vec{r}_D)$ is the detected x-ray intensity, I_{in} is the entrance x-ray intensity, $A_o^2(\vec{r})$ is the attenuation image of the imaged object, say a breast, and $\varphi(\vec{r})$ is the x-ray phase-shift map of the breast. In Eq. (4) R_2 is the object-detector distance, M is the magnification factor employed in the projection, and $\vec{r}_D$ denotes the position in the detector plane. The operator ∇ denotes the two-dimensional transverse gradient differential operator. From Eq. (4) it is clear that the detected x-ray intensity $I\,(\vec{r}_D)$ is determined not only by the conventional attenuation-based contrast $A_o^2\,(\vec{r})$ but also by the transverse Laplacian and gradient differentials of the phase-shift $\varphi\,(\vec{r})$. These differentials represent the edge-enhancements exhibit in the phase-sensitive projection images. Since the phase contrast and attenuation contrast are mixed together in a phase-sensitive projection, there are two unknown variables for a given projection intensity in Eq. (4). Hence, the TIE-based phase retrieval method requires multiple projections (at least two projections) acquired with varying object-detector distances for retrieving the phase-shift map $\varphi(\vec{r})$ of a breast.[17–19] This requirement of multiple image-acquisitions for the TIE-based phase retrievals is obviously cumbersome in implementation, and the multiple exposures make the radiation doses to breast multiplied. As if these were not enough challenges, the TIE-based phase retrieval method is indeed unstable against the noise in projection images. While one might want to increase the radiation doses employed in the projections for retrieving a quality phase map of a breast, the glandular dose to a breast should be kept as low as reasonably achievable because the breast is a radiation sensitive organ. Considering these disadvantages with the TIE-based phase retrieval method, we have to employ a more effective phase retrieval method of measuring breast density through the use of Eqs. (2) and (3).

We noted that the breast fibroglandular tissues and adipose tissues are consisting of dominantly elements with $Z < 10$. If we employ high energy x rays of 60 keV or higher for imaging, the x-ray-breast tissue interactions are dominated by the x-ray Compton scattering from freelike atomic electrons, while the x-ray photoelectric absorption and coherent scattering are all diminished and negligible.[20] In this situation, both the tissue attenuation and phase-shift are all determined by tissues' electron density distributions such that

$$\begin{aligned} A^2(\vec{r}) &= exp[-\sigma_{\mathrm{KN}}(E)\,\rho_{e,p}(\vec{r})], \\ \varphi(\vec{r}) &= -\lambda r_e \rho_{e,p}(\vec{r}), \end{aligned} \tag{5}$$

where $\sigma_{\mathrm{KN}}(E)$ denotes the Klein–Nishina total cross section for Compton scattering and E is the photon energy The Klein-Nishina total cross section changes slowly with photon energy as[20]

$$\sigma_{\mathrm{KN}}(E) = 2\pi r_e^2\left\{\frac{1+\eta}{\eta^2}\left[\frac{2(1+\eta)}{1+2\eta} - \frac{1}{\eta}\log(1+2\eta)\right] + \frac{1}{2\eta}\log(1+2\eta) - \frac{1+3\eta}{(1+2\eta)^2}\right\}, \tag{6}$$

where $\eta \equiv E/511$ keV. In a recent work we explored the relationship between the phase-shift and attenuation defined by Eq. (5) and called this as the phase-attenuation duality (PAD).[21] We found that when the phase-attenuation duality holds, the x-ray propagation equation gets simplified and the phase map can be retrieved from just a single phase-sensitive projection $I\,(\vec{r}_D)$ of the imaged object:[21,22]

$$\varphi(\vec{r}) = \frac{\langle\lambda\rangle r_e}{\langle\sigma_{\mathrm{KN}}\rangle}\ln\{[1-(\langle\lambda^2/\sigma_{\mathrm{KN}}\rangle R_2 r_e\nabla^2/2\pi M)]^{-1} \cdot (M^2 I(\vec{r}_D)/I_{\mathrm{in}})\} \tag{7}$$

Here, the operator ∇^2 denotes the two-dimensional transverse Laplacian differential operator $\nabla^2 \equiv (\partial^2/\partial x^2 + \partial^2/\partial y^2)$ and the operator $\mathcal{D}(\nabla^2) \equiv [1-(\langle\lambda^2/\sigma_{KN}\rangle R_2 r_e\nabla^2/2\pi M)]^{-1}$ is a pseudodifferential operator. The action on a function $g(\vec{r})$ of a pseudodifferential operator such as $\mathcal{D}\,(\nabla^2)$ is defined as

$$\mathcal{D}(\nabla^2)g(\vec{r}) \equiv \iint \exp(i2\pi(\vec{s}-\vec{r})\cdot\vec{f})\cdot\mathcal{D}(-4\pi^2\vec{f}^2) \cdot g(\vec{s})d^2\vec{s}\cdot d^2\vec{f}, \tag{8}$$

where $\vec{s}$ and $\vec{f}$ denote the integral variables in the transverse coordinate space and frequency space, respectively. We call Eq. (7) the PAD-based phase retrieval formula.[21] Recently, we have theoretically and experimentally demonstrated that the PAD-based phase retrievals are robust against the noise, in a stark contrast to the TIE-based method that is unstable in the presence of noise in images.[22] Of course, in order for breast tissues to fulfill the phase-attenuation duality condition, the tube voltages should be set to as high as 120–150 kVp, grossly different from the tube voltages employed in current mammography, where tube voltages used are lower than 40 kVp. Although the attenuation-based tissue contrast gets much reduced at 120–150 kVp, the phase-contrast extracted from the phase retrieval will compensate for the attenuation-contrast loss associated with the use of high tube voltages.[22] Putting above discussion together, we propose that it is feasible to measure the projected electron densities of a breast by using the high-energy x-ray phase-sensitive imaging technique. One can retrieve the phase map of a breast by using only a single phase-sensitive projection of the breast and performing the PAD-based phase retrieval as is shown in Eq. (7). From the retrieved phase map of the breast one can determine its volumetric breast density by using Eq. (3).

In order to numerically validate the proposed new method of breast density measurement, we constructed a digitally simulated anthropomorphic breast phantom. The phantom includes the simulated breast ductal system, the lobule system, and three masses simulating the invasive ductal carcinoma, and four groups of small calcification spheres (in sizes of 0.54, 0.4, 0.32, and 0.2 mm) simulating the breast microcalcifications. In the breast phantom each voxel was randomly assigned with its electron density ρ_e according to a random Gaussian process with a zero mean and unit standard deviation. To simulate the breast tissue texture, the spatial power spectrum of the random electron density distribution was further modified such that it varies as $|\vec{f}|^{1.35}$ for a frequency $\vec{f}$. The resulted phantom's intrinsic by construction volumetric breast density, which we denote by $\mathrm{VBD}_{\mathrm{True}}$, can be computed from the assigned voxel electron densities $\{\rho_e(v), v = 1, \ldots, N\}$ as

$$\mathrm{VBD}_{\mathrm{True}} = \frac{\frac{1}{N}\sum_{v=1}^{N} \rho_e(v) - \rho_{e,\mathrm{ad}}}{\rho_{e,\mathrm{fg}} - \rho_{e,\mathrm{ad}}}, \tag{9}$$

where N is the total number of the phantom voxels.

In order to numerically validate the phase-based method of breast density measurement, we first computed the breast projections with different photon energies. In the simulations we assumed a detector of 50 μm pixels, and set $R_1 = R_2 = 1$ m. The source's focal spot was assumed as a point source. This is an adequate approximation as long as the blur caused by the focal spot is less than the detector pixel size.[15] In our simulation the magnification factor $M = 2$ and pixel size is a 50 μm, so a focal spot of 50 μm or smaller in size can be approximately treated as a pointlike source in the simulation. In this simulation we assumed that the source was with a tungsten target and operated at 140 kVp. We assumed that the detection energy spectrum ranges from 54 keV to 140 keV, including the tungsten characteristic radiations. Selecting this photon-energy range in the simulation was to satisfy the phase-attenuation duality condition with good approximation. This implied that the source should operate at high voltages and with heavy filtrations in the implementation of the proposed method. For a given photon energy, a ray-tracing algorithm was used to compute the ray integrals such as $\int_{\mathrm{ray}} \rho_e(\vec{r}, s)ds$ in the projection. The x-ray phase-shifts and attenuations through the phantom were determined as $\varphi_{\mathrm{ph}}(\vec{r}) = -\lambda r_e \int_{\mathrm{ray}} \rho_e(\vec{r}, s)ds$ and $A^2_{\mathrm{ph}}(\vec{r}) = \exp[-\sigma_{\mathrm{KN}}(E)\int_{\mathrm{ray}} \rho_e(\vec{r}, s)ds]$, as we assumed that the phase-attenuation duality condition is satisfied for fibroglandular and adipose tissues in this simulation to numerically validate the proposed method. Using the computed $\varphi_{\mathrm{ph}}(\vec{r})$ and $A^2_{\mathrm{ph}}(\vec{r})$, we simulated the x-ray Fresnel diffraction of the exit x rays propagating from the breast phantom to the detector,[23] and thereby we computed the detected Fresnel diffraction intensity $I_{\mathrm{mono}}(\vec{r}_D, E)$ for each individual energy E. To compute the phase-sensitive projection intensity $I_{\mathrm{poly}}(\vec{r}_D)$ with the polychromatic x rays, we summed the $I_{\mathrm{mono}}(\vec{r}_D, E)$ over photon energies in the detection spectrum. On the other hand, it is important to examine the effects of the noise on the accuracies in the breast density measurement. In fact, the robustness of the phase retrieval method is critical to the success of the proposed phase-based method of breast density measurement, as some methods in the literature may be unstable at some substantial noise levels.[22] To simulate the noise effects, we added the Poisson noise with different noise-levels into the simulated phase-sensitive projections of the phantom, following the standard noise simulation method used in the literature.[24] Employing the PAD-based phase-retrieval formula (7), we retrieved the phase map $\varphi(\vec{r})$ of the breast phantom. Using the retrieved $\varphi(\vec{r})$ and Eq. (3) we reconstructed the phantom's volumetric breast density VBD.

III. RESULTS

According to the aforementioned method, we constructed a digitally simulated anthropomorphic breast phantom, which simulates a compressed breast of 4.5 cm thick, 20 cm in lateral, and 10 cm in chest wall-nipple dimension. Applying Eq. (9) to the randomly assigned electron densities of this phantom, we found the phantom's intrinsic by construction volumetric breast density $\mathrm{VBD}_{\mathrm{True}} = 0.5025$. We take this $\mathrm{VBD}_{\mathrm{True}}$ value as the reference to evaluate the accuracy of the reconstructed phantom volumetric breast density.

From the simulated phase-sensitive projection image of the phantom and using Eqs. (2) and (7) with $T_c = 4.5$ cm, we computed the $m(\vec{r})$-image of the breast phantom, the map of the phantom's fibroglandular-tissue fractions, as is shown in Fig. 1. In this image, the shade of gray of a pixel represents the computed fraction of fibroglandular tissues along a ray passing the pixel. A lighter shade of gray represents a larger fraction of fibroglandular tissues. In this way, the $m(\vec{r})$-image exhibited good breast tissue contrast as well (Fig. 1.) Moreover, this $m(\vec{r})$-image provided the basis for reconstructing the phantom's volumetric breast density. Using the VBD-formula (3), we found the phantom's volumetric breast density VBD = 0.5028, which differs from its intrinsic volumetric breast density by only 0.06%, achieving an excellent accuracy. Furthermore, testing the breast density determination from the projection images with different signal-to-noise-ratio (SNR) levels associated with different mean glandular doses. The SNR, which is similarly defined as in conventional mammography, is defined

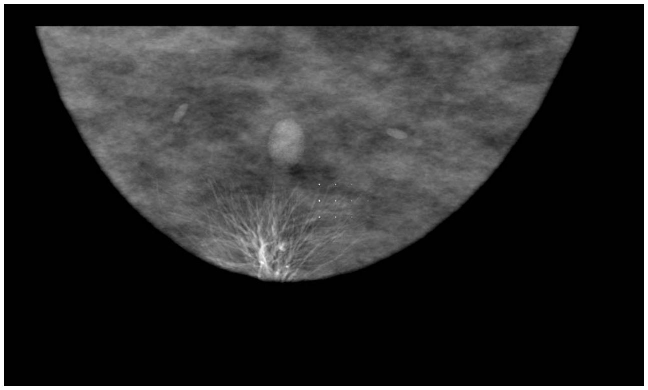

FIG. 1. The computed $m(\vec{r})$-image of the breast phantom, namely, the map of the phantom's fibroglandular-tissue fractions.

as the mean intensity over a ROI drawn in the center of the phantom projection image over the standard deviation of the intensity values. We tested the cases with the projection SNR = 34, 64, and 136, which are corresponding to estimated mean glandular doses of 0.14, 0.57, and 2.21 mGy, respectively. We found that the reconstructed VBD values keep achieving good accuracies, in spite of the presence of noise in the simulated projections. With the projection SNR = 34 we found the reconstructed VBD = 0.5115, which differs from the intrinsic volumetric breast density $\mathrm{VBD}_{\mathrm{True}}$ by only 1.79%. The error in reconstructed VBD decreases with increasing projection SNR value. For example, we found the reconstructed VBD = 0.5106 for SNR = 68, which differs from $\mathrm{VBD}_{\mathrm{True}}$ by only 1.61%. The error in VBD is further reduced to 1.55% for SNR = 134. All these results numerically validated the proposed phase-shifts-based method as a novel breast density measurement method with good accuracies.

IV. DISCUSSION AND CONCLUSIONS

Current x-ray-based methods of breast density measurement are all based on small attenuation differences between breast tissues. However, as the linear attenuation coefficients of breast tissues vary in a complicated way as the employed x-ray spectrum changes, all these methods have to require elaborated phantom-based system calibrations, some of them include simultaneous exposures of the phantom alongside the breast for system calibrations.[7,8,10] The proposed phase-shifts-based method measures the tissue projected electron densities rather than their projected attenuation coefficients. Our strategy of direct probing tissue electron densities simplifies the system calibration for breast density measurement. In fact, as Eqs. (3) and (7) involve the spectral averages of x-ray wavelengths and the Klein-Nishina cross sections, the system parameters that our method requires are the source x-ray spectra and detector responses. Another key idea in our method is to use the PAD-based phase retrieval technique for obtaining the breast phase map. As breast imaging is stringently regulated for radiation doses involved, there are always substantial noises in breast projection images. Some common phase retrieval methods in the literature are actually unstable in presence of noise,[22] and the large errors in the retrieved phase map caused by the retrieval instability would spoil the breast density measurement. The high robustness against noise of the PAD-based phase retrieval technique is crucial to our method for achieving good accuracies in breast density determination. Of course, many future works are required for implementing this phase-based method of breast density measurement. In our compressed breast model, 13.5% of breast volume is in the curved periphery zone of the breast, and breast thickness in the periphery is not uniform and falls off quickly. This portion of tissues was not included in the VBD computation for avoiding the errors in thickness estimation. Therefore, if the periphery has a quite different breast density than the rest of breast, this approach may cause errors in the computed VBD. Hence, how to accurately estimate the breast thickness is an area for improvement, and it is also an active research area in implementing other x-ray imaging-based methods of breast density measurement.[25] In addition, it will be useful to develop a correction method for the VBD errors in cases where an imaging setup does not accurately satisfy the phase-attenuation condition.

In summary, in this work we propose for the first time an x-ray phase-shifts-based method of measuring the volumetric breast density. The proposed Eq. (3)-based method of breast density measurement can be applied to any of phase-sensitive imaging techniques such as the inline or the grating-based techniques. This phase-shifts-based method measures the tissue projected electron densities rather than their projected attenuation coefficients. The direct probing of tissue electron densities in our method simplifies the system calibration requirement. The robust PAD-based phase retrieval method employed in the inline technique ensures the accuracy of the reconstructed volumetric breast densities. Constructing an anthropomorphic digitally simulated breast phantom, we performed simulations for validating this novel method of breast density measurement. Testing with different projection SNR-levels in the simulations, we found that the reconstructed volumetric breast densities achieved good accuracies compared to the phantom's intrinsic volumetric breast density. All these results numerically validated the proposed phase-shifts-based method as a novel method of breast density measurement with good accuracies.

ACKNOWLEDGMENTS

This research was supported in part by the Department of Defense Breast Cancer Research Program under Award No. W81XWH-08-1-0613 and the NIH under Grant No. R01CA142587. H. Liu would like to acknowledge the support of Charles and Jean Smith Chair endowment fund as well.

[a] Author to whom correspondence should be addressed. Electronic mail: xwu@uabmc.edu

[1] W. J. Nk, "Risk for breast cancer development determined by mammographic parenchymal pattern," Cancer **37**, 2486–2492 (1976).

[2] N. F. Boyd, L. J. Martin, M. J. Yaffe, and S. Minkin, "Mammographic density and breast cancer risk: Current understanding and future prospects," Breast Cancer Res. Treat. **13**, 1–12 (2011).

[3] V. A. McCormack and I. dos Santos Silva, "Breast density and parenchymal patterns as markers of breast cancer risk: A meta-analysis," Cancer Epidemiol. Biomarkers Prev. **15**, 1159–1169 (2006).

[4] R. P. Highnam and J. M. Brady, *Mammographic Image Processing* (Kluwer Academic, Boston, 1999).

[5] R. Highnam, M. Brady, and B. Shepstone, "A representation for mammographic image processing," Med. Image Anal. **1**, 1–8 (1996).

[6] J. A. Shephard, K. M. Kerlikowske, R. Smith-Bindman, H. K. Genant, and S. R. Cummings, "Measurement of breast density with dual X-ray absorptiometry: Feasibility," Radiology **223**, 554–557 (2002).

[7] O. Pawluczyk, B. J. Augustine, M. J. Yaffe, D. Rico, J. Yang, G. E. Mawdsley, and N. F. Boyd, "A volumetric method for estimation of breast density on digitized screen-film mammograms," Med. Phys. **30**, 352–364 (2003).

[8] S. Van Engeland, P. R. Snoeren, H. Huisman, C. Boetes, and N. Karssemeijer, "Volumetric breast density estimation from full-field digital mammograms," IEEE Trans. Med. Imaging **25**, 273–282 (2006).

[9] K. E. Martin, M. A. Helvie, C. Zhou, M. A. Roubidoux, J. E. Bailey, C. Paramagul, C. E. Blane, K. A. Klein, S. S. Sonnad, and H.-P. Chan, "Mammographic density measured with quantitative computer-aided method: Comparison with radiologists' estimates and BIRADS categories," Radiology **240**, 656–665 (2006).

[10] M. J. Yaffe, "Measurement of mammographic density," Breast Cancer Res. Treat. **10**, 1–10 (2008).

[11] A. Snigirev *et al.*, "On the possibilities of x-ray phase contrast microimaging by coherent high-energy synchrotron radiation," Rev. Sci. Instrum. **66**, 5486–5492 (1995).

[12] S. Wilkins, T. Gureyev, D. Gao, A. Pogany, and A. Stevenson, "Phase contrast imaging using polychromatic hard x-ray," Nature (London) **384**, 335–338 (1996).

[13] F. Arfelli *et al.*, "Mammography with synchrotron radiation: Phase-detection techniques," Radiology **215**, 286–293 (2000).

[14] E. Donnelly and R. Price, ''Effect of kVp on edge-enhancement index in phase-contrast radiography,'' Med. Phys. **29**, 999–1002 (2002).

[15] X. Wu and H. Liu, "Clinical implementation of phase contrast x-ray imaging: Theoretical foundation and design considerations," Med. Phys. **30**, 2169–2179 (2003).

[16] G. Hammerstein, D. Miller, D. White, M. Masterson, H. Woodard, and J. Laughlin, "Absorbed radiation dose in mammography," Radiology **130**, 485–491 (1979).

[17] K. Nugent, T. Gureyev, D. Cookson, D. Paganin, and Z. Barnea, "Quantitative phase imaging using hard x rays," Phys. Rev. Lett. **77**, 2961–2965 (1996).

[18] L. Allen and M. Oxley, "Phase retrieval from series of images obtained by defocus variation," Opt. Commun. **199**, 65–85 (2001).

[19] P. Cloetens, R. Mache, M. Schlenker, and S. Lerbs-Mache, "Quantitative phase tomography of Arabidopsis seeds reveals intercellular void network," Proc. Natl. Acad. Sci. U.S.A. **103**, 14626–14630 (2006).

[20] N. A. Dyson, *X-rays in Atomic and Nuclear Physics* (Longman, London, 1973).

[21] X. Wu, H. Liu, and A. Yan, "X-ray phase-attenuation duality and phase retrieval," Opt. Lett. **30**, 379–381 (2005).

[22] A. Yan, X. Wu, and H. Liu, "Robustness of phase retrieval methods in x-ray phase contrast imaging: A comparison," Med. Phys. **38**, 5073–5080 (2011).

[23] M. Born and E. Wolf, *Principle of Optics*, 6th ed. (Pergamon, Oxford, 1980).

[24] R. S. Saunders Jr., and E. Samei, "A method for modifying the image quality parameters of digital radiographic images," Med. Phys. **30**, 3006–3017 (2003).

[25] G. Mawdsley, A. Tyson, C. Peressotti, R. Jong, and M. Yaffe, "Accurate estimation of compressed breast thickness in mammography," Med. Phys. **36**, 577–586 (2009).

COL 10(12), 121101(2012) CHINESE OPTICS LETTERS December 10, 2012

Phase retrieval for hard X-ray computed tomography of samples with hybrid compositions

Huiqiang Liu (刘慧强)[1], Yuqi Ren (任玉琦)[1], Han Guo (郭 瀚)[1], Yanling Xue (薛艳玲)[1],
Honglan Xie (谢红兰)[1], Tiqiao Xiao (肖体乔)[1*], and Xizeng Wu (吴希增)[2]**

[1]*Shanghai Institute of Applied Physics, Chinese Academy of Sciences, Shanghai 201204, China*
[2]*Department of Radiology, University of Alabama at Birmingham, Birmingham, Alabama 35233, USA*
[*]*Corresponding author: tqxiao@sinap.ac.cn;* [**]*corresponding author: xwu@uabmc.edu*

Received May 31, 2012; accepted June 20, 2012; posted online September 14, 2012

X-ray tomography of samples containing both weakly and strongly absorbing materials are necessary in material and biomedical imaging. Extending the validity of the phase-attenuation duality (PAD) method, the propagation-based phase-contrast computed tomography (PPCT) of a sample with hybrid compositions of both the light and dense components with 60 keV of synchrotron radiation is investigated. The experimental results show that the PAD-based PPCT is effective in imaging both the weakly and strongly absorbing components simultaneously. Compared with the direct PPCT technique, the PAD-based PPCT technique demonstrates its excellent capability in material discrimination and characterization. In addition, the PAD-based PPCT exhibits a striking performance on the image contrast enhancement and noise suppression. Therefore, this technique is useful for material and biomedical imaging applications, especially when the radiation dose involved imposes a serious constraint.

OCIS codes: 110.6960, 100.5070, 170.3010, 340.7440.
doi: 10.3788/COL201210.121101.

X-ray tomography of samples containing both weakly and strongly absorbing materials is necessary in material and biomedical imaging[1,2]. Propagation-based phase-contrast computed tomography (PPCT) is a good choice for this purpose because it utilizes highly sensitive phase contrast and requires a relatively simple setup[3−5]. Two different types of approaches are available for PPCT. One type is direct PPCT, in which the tomographic reconstruction, such as that based on the filtered back-projection (FBP) algorithm, is directly applied to the acquired angular projections with mixed attenuation and phase contrast. The other type is phase retrieval-based PPCT, in which the acquired projections are preprocessed with the phase retrieval before tomographic reconstruction. The phase retrieval on the acquired angular projections can enhance image contrast, reduce artifacts, and enable quantitative characterization of the sample[6−8]. However, multiple sets of projections must be obtained at different sample-detector distances (SDDs) to proceed with the phase retrieval, indicating that a laborious acquisition process is needed, and considerably more radiation dose is introduced[9−11]. Therefore, a phase retrieval-based PPCT method that uses only a single set of projections is highly desirable.

The phase shift results from X-ray coherent scattering, whereas the attenuation arises from the three kinds of interactions between X-ray and matter, such as photoelectric absorption, incoherent scattering, and coherent scattering. The phase attenuation duality (PAD) relation holds for X-rays of 60–500 keV transmitted from the samples of light elements with atomic numbers $Z < 10$[7]. In these cases, the attenuations and phase shifts of the samples are all related to the projected electron densities along the X-ray paths. Under PAD conditions, the X-ray intensity propagation equation is simplified, such that robust phase retrieval can be achieved from only a single projection at each view angle. This letter reports the experimental results for a sample with hybrid composition to demonstrate the capability of the PAD-based PPCT technique in material discrimination and characterization.

A sample for phase-contrast imaging is modeled as a 2D transmission function in the object plane X$= (x,\ y)$, with the amplitude denoted by $A(\mathrm{X})$ and the phase by $\varphi(\mathrm{X})$. Maps $A^2(\mathrm{X})$ and $\varphi(\mathrm{X})$ are the attenuation image of the sample and the phase image, respectively. $A^2(\mathrm{X})$ is related to the projected electron density $\rho_{\mathrm{e,\ p}}(\mathrm{X})$ when the PAD condition is satisfied, given that $A^2(\mathrm{X})=\exp[-\sigma_{\mathrm{KN}}\rho_{\mathrm{e,\ p}}(\mathrm{X})]$, where σ_{KN} is the total cross section of the X-ray Compton scattering from a single free electron. However, the phase shift $\varphi(\mathrm{X})$ along a ray path is given by $\lambda r_{\mathrm{e}}\rho_{\mathrm{e,\ p}}(\mathrm{X})$, and r_{e} is the classic electron radius. Based on the paraxial Fresnel-Kirchhoff diffraction, the projected electron density $\rho_{\mathrm{e,\ p}}(\mathrm{X})$ is given as[7]

$$\rho_{\mathrm{e,p}}(\mathrm{X})=-\frac{1}{\sigma_{\mathrm{KN}}}\ln\left\{f^{-1}\left\{\frac{f\left\{M^2 I\left(M\mathrm{X};R_1+R_2\right)\right\}}{I_{\mathrm{in}}\left(1+2\pi\left(\frac{\lambda^2 r_{\mathrm{e}}R_2}{M\sigma_{\mathrm{KN}}}\right)u^2\right)}\right\}\right\}, \tag{1}$$

where $M = (R_1 + R_2)/R_1$, R_1 is the source-to-sample distance, R_2 denotes the SDD, $I(\mathrm{X}; R_1 + R_2)$ is the projection intensity at detector plane, and I_{in} is the entrance intensity. In Eq. (1), $f\{\ \}$ denotes the 2D Fourier transform, $f^{-1}\{\ \}$ is its inverse, and u denotes the spatial frequency vector in the object plane. The initial angular projections in PAD-based PPCT are preprocessed with PAD-based phase retrievals, and then the standard FBP algorithm is employed to reconstruct the distribution of the electron densities in the sample from the preprocessed projections.

The experiments were performed at the X-ray Imaging and Biomedical Application Beamline (BL13W1) of the

© 2012 Chinese Optics Letters

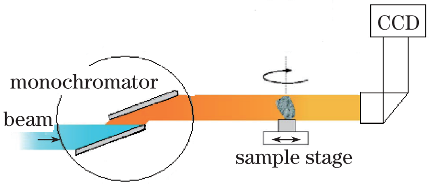

Fig. 1. Schematic of the propagation-based imaging system.

Shanghai Synchrotron Radiation Facility (SSRF), which can provide high flux X-rays in the energy range of 8–72.5 keV. The sample was located at approximately 34-m downstream of the wiggler source to provide both high spatial coherence and almost parallel beam. The schematic of the experimental setup is demonstrated in Fig. 1. The experiments were conducted at 60 keV, with a SDD of 80 cm. The phantom for the experiments was composed of four types of standard materials (GoodFellow Cambridge Limited), namely, an alumina rod (Al_2O_3, $\Phi = 1$ mm, 3.9 g/cm^{-3}), an aluminum tube (Al, $\Phi_{\rm in}$= 1.166 mm, $\Phi_{\rm out}$= 1.42 mm, 2.7 g/cm^{-3}), a PTFE tube (C_2F_4, $\Phi_{\rm in} = 1$ mm, $\Phi_{\rm out}$= 1.82 mm, 2.2 g/cm^{-3}), and a PMMA rod ($C_5H_8O_2$, $\Phi = 1$ mm, 1.19 g/cm^{-3}). The metallic oxide and metal components were chosen to simulate dense materials, such as the bones, whereas the polymer components were used to simulate light materials, such as soft tissues.

A total of 900 phase-contrast radiographs were collected over a 180° rotation for a tomographic data set; each radiograph was acquired with an exposure time of 208 ms. The detector was a CCD (Photonic Science) with a 9-μm effective pixel size. Considering that a highly coherent X-ray beam and large SSD were employed, all these radiographs exhibited not only the usual attenuation-based image contrast, but also enhanced material interfaces as a result of the refraction and diffraction of the phase-shifted X-rays. For comparison, tomograms were reconstructed using the angular projection data set through two different techniques, namely, the direct and the PAD-based PPCTs. The tomogram by direct PPCT, in which the standard FBP algorithm was directly applied to the initial projections, is shown in Fig. 2(a). The structures for the dense and light material components can all be distinguished from each other because of the edge enhancements at the interfaces. Notably, some micropores inside the Al_2O_3 rod became apparent as the results of the edge-enhancement. This feature indicates that the direct PPCT method is suitable for distinguishing the small cracks or voids embedded inside a sample. However, the bulk contrast between the different materials appeared rather weak. Moreover, Fig. 2(a) presents anomalously large or even negative apparent linear attenuation coefficients at material interfaces, impeding proper material characterization. According to a general analysis of the direct PPCT technique, the pixel value indicated in Fig. 2(a), namely the reconstructed apparent attenuation coefficient, was not equal to the material linear attenuation coefficient. Rather, the reconstructed apparent attenuation coefficient is a sum of three parts, i.e., the linear attenuation coefficient of the material, the Laplacian of the refractive index of the material, and the nonlocal contribution, which is dependent on the global variations in the phantom attenuation coefficients and refractive indices[5]. The presence of an excessive noise added uncertainty to the apparent attenuation coefficients.

The tomogram shown in Fig. 2(b) was reconstructed using the PAD-based PPCT method, in which the acquired projections were preprocessed with the PAD-based phase retrievals to retrieve the $\rho_{\rm e,\ p}$-maps for each individual angular view. FBP-based algorithm was then applied to these retrieved $\rho_{\rm e,\ p}$-maps for tomography reconstruction. For comparison, the intensity profiles along two white dash-dot circles in Figs. 2(a) and (b) are shown in Fig. 3. The red dashed line associated with the direct PPCT method shows severe high-frequency noise and weak bulk contrast, which cannot provide useful means for material characterization. However, the blue solid line with the PAD-based PPCT method demonstrates good bulk-contrast and high signal-to-noise ratios, enabling qualitative and quantitative material characterization. The bulk contrast-to-noise ratios (CNRs) achieved in Figs. 2(a) and (b) were compared to quantify the noise-suppression advantage of the PAD-based PPCT. The signal was defined as the mean image intensity in a region of interest, excluding the boundaries. The contrast was defined as the difference in the signals in two regions of interest, and the noise was the average of the standard deviations of the intensities in the two regions. The bulk CNRs achieved with the two techniques are shown in Fig. 4, indicating that the bulk CNRs with the PAD-based PPCT method were approximately 10 to 15 times higher than that with the direct PPCT method. This significant enhancement in the bulk CNR implies that the PAD-based method has the potential to reduce tremendously the radiation dose. This feature is particularly useful for biomedical applications, where a good bulk contrast is critical for tissue/lesion characterization. Some ring artifacts are present in both Figs. 2(a) and (b), which are due to the beam quality degradation at high photon energies.

In addition, the histograms derived from Figs. 2(a) and (b) are demonstrated in Figs. 5(a) and (b), respectively. Figure 5(a), which is derived from direct PPCT, shows that the overlapped histogram peaks hamper the discrimination between the four different materials in the sample. However, Fig. 5(b) from the PAD-based PPCT shows that the well-separated peaks clearly discriminate among the four different materials in the sample. The histogram peaks in Fig. 5(b) were identified as those of PMMA, PTFE, Al, and Al_2O_3 from left to right.

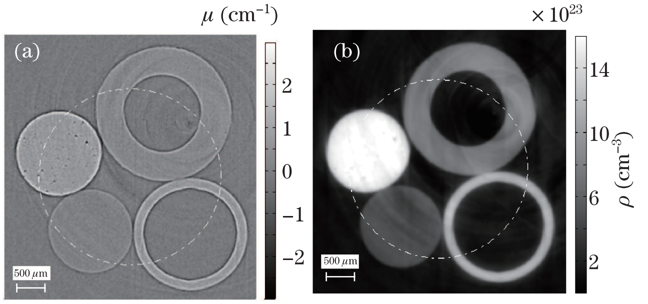

Fig. 2. Reconstructions for the sample at 60 keV. Tomograms of (a) direct and (b) PAD-based PPCTs.

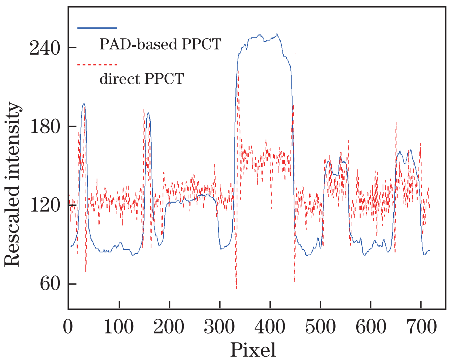

Fig. 3. (Color online) Profiles of rescaled intensity on the trace of white dash-dot circle in Figs. 2(a) and (b), respectively.

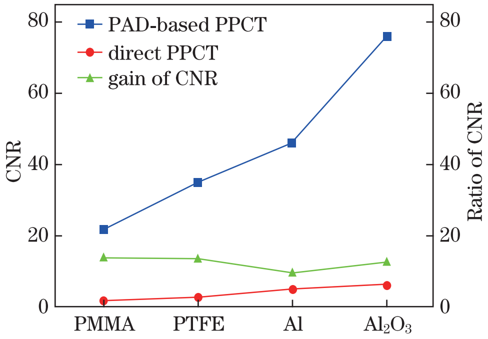

Fig. 4. Plots of CNR for both direct and PAD-based PPCTs as well as the gain of the CNRs of the PAD-based and direct PPCTs.

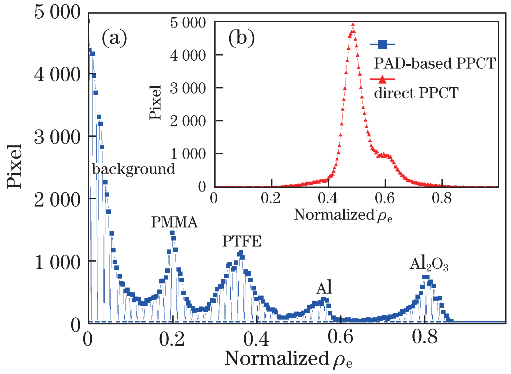

Fig. 5. Histograms of the electron density distribution of the samples with (a) direct and (b) PAD-based PPCTs.

This layout of the peaks is consistent with the true electron density values of these materials.

Moreover, some quantitative information can also be obtained from the histogram shown in Fig. 5(b). The PAD condition at 60 keV holds for the materials made of light elements with $Z<10$. Hence, good accuracies can be achieved in recovering the electron densities of the PTFE tube and PMMA rod in the sample because these two materials consist of the light elements with $Z<10$. The electron density of a material is theoretically expressed as $\rho_e = N_a\rho\sum[w_i(Z_i/A_i)]$, where N_a is the Avogadro constant and ρ is the mass density of the material; w_i, Z_i, and A_i are the elemental weight fraction, atomic number, and atomic weight of the material, respectively. Therefore, the obtained theoretical electron density values were $\rho_e(\text{PMMA}) = 3.865\times10^{23}$ cm^{-3} and $\rho_e(\text{PTFE}) = 6.358\times10^{23}$ cm^{-3}, and their ratio was $\rho_e(\text{PTFE})/\rho_e(\text{PMMA})$=1.645. However, the histogram in Fig. 5(b) shows that the ratio $[\rho_e(\text{PTFE})/\rho_e(\text{PMMA})]_{\text{peak}} = 1.714$ differs from its theoretical value by only 4.2%. Moreover, Fig. 2(b) shows that the reconstructed electron density values of these two materials are less than 12% different from their theoretical values. These results demonstrate that the PAD-based PPCT method achieved good accuracies in evaluating the electron densities of the materials composed of light elements. Similar ratios involving aluminum atoms, such as $[\rho_e(\text{Al})/\rho_e(\text{PMMA})]_{\text{peak}}$ and $[\rho_e(\text{Al}_2\text{O}_3)/\rho_e(\text{PMMA})]_{\text{peak}}$, differ from their theoretical ratios by as much as 36%. These larger errors are expected considering that the PAD does not hold for heavier elements, such as aluminum (Z=13). These errors associated with heavier elements can be reduced as the X-ray photon energy increases.

Although several other methods that use only a single set of projections for the phase retrieval-based PPCT are available, these methods are not applicable to samples of hybrid materials with both light and dense components. As analyzed in Ref. [13], some of these methods require samples with diminished attenuation, whereas others are applicable only to samples composed of single or binary materials with known linear attenuation coefficients and refractive indices. The proposed method is therefore advantageous because it does not require such assumptions and constraints. The PAD-assumption holds only if the X-ray Compton scattering dominates in the X-ray attenuation process, as we point out at the beginning. Hence, additional research is needed to investigate whether the PAD-based PPCT method is applicable for other combinations of light and dense materials encountered in material and biomedical applications.

In conclusion, extending the validity of the PAD-based method, the PPCT of a sample with hybrid compositions is investigated using a 60-keV synchrotron radiation. The experimental results show that the PAD-based PPCT is effective in imaging simultaneously both the weakly and strongly absorbing components. Compared with the direct PPCT technique, the PAD-based PPCT demonstrats its excellent capability in material discrimination and characterization. This PAD-based method also exhibits a striking performance on the bulk-contrast enhancement and noise suppression. This technique therefore has great potential for material and biomedical applications, especially when the radiation dose involved imposes a serious constraint.

This work was supported by the National Basic Research Program of China (No. 2010CB834301), the External Cooperation Program of Chinese Academy of Science (No. GJHZ09058), and the National Natural Science Foundation of China (No. 11105213). XW was supported in part by the U.S. NIH grant R01CA142587 and the DoD Breast Cancer Research Program award W81XWH-08-1-0613.

References

1. P. Cloetens, R. Mache, M. Schlenker, and S. Lerbs-Mache, PNAS **103,** 14626 (2006).
2. J. P. Guigay, M. Langer, R. Boistel, and P. Cloetens, Opt. Lett. **32,** 1617 (2007).
3. P. Cloetens, W. Ludwig, J. Baruchel, D. Van Dyck, J. Van Landuyt, J. P. Guigay, and M. Schlenker, Appl. Phys. Lett. **75,** 2912 (1999).
4. R. Chen, H. Xie, L. Rigon, R. Longo, E. Castelli, and T. Xiao, Opt. Lett. **36,** 1719 (2011).
5. X. Wu, H. Liu, and A. Yan, EJR **68S,** S8 (2008).
6. M. Langer, P. Cloetens, and F. Peyrin, IEEE Trans. Image Process. **19,** 2428 (2010).
7. X. Wu, H. Liu, and A. Yan, Opt. Lett. **30,** 379 (2005).
8. A. Groso, R. Abela, and M. Stampanoni, Opt. Express **14,** 8103 (2006).
9. M. Langer, P. Cloetens, J. P. Guigay, and F. Peyrin, Med. Phys. **35,** 4556 (2008).
10. A. Burvall, U. Lundstr**ö**m, P. A. C. Takman, D. H. Larsson, and H. M. Hertz, Opt. Express **19,** 10359 (2011).
11. Y. Ren, C. Chen, R. Chen, G. Zhou, Y. Wang, and T. Xiao, Opt. Express **19,** 4170 (2011).